# FOCUSED FLOW OF WATER INTO ETHANOL-CONTAMINATED SAND

# FOCUSED FLOW DURING WATER INFILTRATION INTO ETHANOL-CONTAMINATED UNSATURATED POROUS MEDIA

By
ALICJA N. JAZWIEC, B.Sc.

A Thesis Submitted to the School of Geography and Earth Sciences
in Partial Fulfillment of the Requirements for the Degree Master of Science

MASTER OF SCIENCE (2018)
McMaster University, Hamilton, Ontario
School of Geography and Earth Science
TITLE: Focused flow during water infiltration into ethanol-contaminated unsaturated porous media
AUTHOR: Alicja N. Jazwiec
SUPERVISOR: Professor James E. Smith
NUMBER OF PAGES: xv, 145

## Lay Abstract

Understanding the behaviour and interaction of water and contaminants in soils is important as environmental contamination and spills can have devastating environmental impacts. In recent decades, ethanol spills and accidental releases onto ground surface have increased as the commercial and industrial use of ethanol has increased. The goals of this work were to qualitatively visualize and quantify the unique nature of water infiltration into the ethanol-contaminated soil and understand the complex mechanisms behind water-ethanol interactions. This research showed that water infiltration creates an uncommon vertical, focused pattern when flowing into sand contaminated by ethanol. However, when ethanol is applied to standard water-wet sand, that behaviour is not observed. This work provided greater insight into the nature of ethanol-contaminated soils. These findings furthered the understanding needed to evaluate impacts that ethanol contamination can have on remedial efforts and the rate of migration of contaminants to groundwater.

## Abstract

The increasing commercial and industrial use of ethanol, i.e., in biofuel and gasoline, has generated increased incidents of vadose zone contamination by way of ethanol spills and releases. This has increased the interest in better understanding infiltration behaviours of ethanol in unsaturated porous media and the multiphase interactions in the vadose zone. Solute-dependent capillarity-induced focused flow (SCIFF) is a vertical, highly focused flow infiltration behaviour first reported by Smith et al. (2011) in butanol-contaminated sands. Through the use of highly controlled laboratory experiments, this thesis research investigates focused flow (SCIFF) and related behaviours through water infiltration into ethanol-contaminated unsaturated sand.

Focused flow behaviours (SCIFF) were demonstrated through the infiltration of water into an ethanol-contaminated unsaturated sand using both constant flux and constant head methodologies. The observation of focused flow behaviours in ethanol-contaminated sand supported the primary hypothesis of this work. The secondary hypothesis was also supported, as focused flow behaviours were not observed, rather stable semicircular infiltration patterns were observed during ethanol infiltration into water-wet sand. Comparisons between constant flux and constant head application methods under similar flow rates and fluid volumes produced similar results. The zone of lower saturation, or the "halo effect" reported in previous literature, was strongly expressed during water infiltration in ethanol-contaminated sand. This halo effect is affected by the maximum (at 40% to 50%) of aqueous concentration of ethanol. This maximum enhances the zone of

lower saturation and stabilizes the solute front. The SCIFF focused flow also overcame the effects of minor heterogeneities in the sand. However, additional laboratory and modelling work is required to further understand the extent of SCIFF behaviour.

Keywords

focused flow, solute-induced capillarity-dependent focused flow, SCIFF, infiltration, ethanol, vadose zone, unsaturated zone, flow cell, porous media, rainulator, constant flux, tension infiltrometer, constant head, soil physics, hydrology, hydrogeology

## Acknowledgements

Research is always a collaborative effort. I would like to take this opportunity to thank the many people who helped me bring this thesis to completion.

First, I would like to thank my committee members, Dr. Sean K. Carey, Dr. Gregory F. Slater, and Dr. James E. Smith (Supervisor) for their guidance and examination of this thesis. Over the years, their instruction in their respective areas of expertise has shaped my understanding of and passion for my field.

The appreciation and respect I have for Dr. James Smith is indescribable. During my years as an undergraduate student, Jim opened up the world of hydrogeology and scientific research for me, which has ultimately inspired my career. His mentorship, curiosity, and knowledge strongly supported my development as a scientist. Jim, thank you for everything.

I am grateful to the women in science, past and present, who continue to inspire and drive the passion in me every single day. My greatest inspiration has come from my sister, Patrycja Jazwiec; her tenacity and brilliance is truly one of a kind. Jennie Kirby, thank you for the years of technical and moral support. Dr. Maureen Padden, Dr. Sarah M. Beatty, Dr. Heather C. McLeod, and Kelly Van Burgsteden, the impact you made on my time as a graduate student is immeasurable; thank you.

Martin Czernicki, thank you for your unwavering love and encouragement.

This final year could not have been possible without the support of my family at Halton Region. This year of growth and laughter created memories that will last a lifetime. I sincerely thank Jon Clark, Adam Gilmore, David McCollum, John McIntosh, and Hayley Pankhurst.

Funding is required for scientific research to progress. I am grateful for the support provided by the Canadian Natural Sciences and Engineering Research Council Discovery Grant granted to James E. Smith and the Ontario Graduate Scholarship granted to Alicja N. Jazwiec.

My parents have fostered in me a curious mind and strong work ethic. This thesis would not have been possible without the lifetime of support and love of my parents. Thank you, Mom and Dad.

I will always be sincerely grateful to the incredible people who made this work possible; thank you.

Table of Contents

List of Figures

List of Tables

# List of Abbreviations and Symbols

| | |
|---|---|
| A | Area |
| C | Proportionality constant |
| *d* | Effective mean grain size diameter |
| DNAPL | Dense nonaqueous phase liquid |
| g | Acceleration due to gravity |
| h | Hydraulic head |
| K | Hydraulic conductivity |
| $K(\psi)$ | Unsaturated hydraulic conductivity |
| $K_r(\psi)$ | Relative unsaturated hydraulic conductivity |
| k | Intrinsic permeability |
| L | Distance |
| $M_S$ | Mass of solids |
| $M_T$ | Total mass |
| NAPL | Nonaqueous phase liquid |
| n | Porosity |
| $P_a$ | Capillary pressure of the nonwetting fluid |
| $P_b$ | Capillary pressure of the wetting fluid |
| $P_C$ | Capillary pressure |
| Q | Volumetric flow rate |
| q | Volumetric flux |
| R | Residual |
| r | Radius of curvature |
| S | Saturated |
| SCIFF | Solute-dependent capillarity-induced focused flow |
| $V_S$ | Volume of solids |
| $V_T$ | Total volume |
| $V_W$ | Volume of water |

| | |
|---|---|
| $V_V$ | Volume of voids |
| z | Elevation head |
| α | Fitting parameter |
| ψ | Pressure head |
| $\psi_a$ | Air entry pressure head |
| $\nabla(h)$ | Gradient of the total soil water potential |
| ρ | Fluid density |
| $\rho_p$ | Bulk density |
| $\rho_p$ | Particle density |
| μ | Kinematic viscosity |
| $\nu$ | Dynamic viscosity |
| $\bar{v}$ | Average linear pore water velocity |
| Θ | Effective saturation |
| θ | Volumetric moisture content |
| $\theta_r$ | Residual water content |
| $\theta_S$ | Saturated water content |
| σ | Surface (interfacial) tension |
| ϕ | Total soil moisture potential |
| 2-D | Two-dimensional |

## Declaration of Academic Achievement

The contributions of this thesis include the following: qualitative visualization and quantitative demonstration of focused flow behaviour (SCIFF) through water infiltration into ethanol-contaminated unsaturated sand using highly controlled laboratory experiments, increased understanding and insight into the halo effect that was strongly expressed in this work, and comparison between constant flux and constant head application methods, which under similar conditions, generated similar results.

This thesis was prepared in accordance with the McMaster University Guidelines for the preparation of standard theses. This thesis was completed under the close supervision of Dr. James E. Smith.

# 1 Introduction

The increasing commercial and industrial use of ethanol in biofuels has generated incidents of vadose zone contamination by way of ethanol spills and releases. This has increased the interest in better understanding behaviours of ethanol in unsaturated porous media and its multiphase interactions in the vadose zone.

## 1.1 Darcy's Law

Darcy's Law describes the ability of a fluid to flow through a porous media (Equation 1).

$$q = -K\frac{\Delta h}{\Delta L} \quad (1)$$

Where q is the volumetric flux, K is the hydraulic conductivity, h is the hydraulic head, and L is the distance. The negative sign seen in Equation 1 is used to denote groundwater flow from high hydraulic head to low hydraulic head. The hydraulic gradient $\left(\frac{\Delta h}{\Delta L}\right)$ is the driving force of groundwater flow. The discharge is proportional to the hydraulic conductivity. Darcy's law is valid for flow in any spatial direction (Freeze & Cherry, 1979).

## 1.2 Darcy Flux

Darcy flux (Equation 2), or specific discharge, is the volumetric flow rate per unit cross-sectional area.

$$q = \frac{Q}{A} \quad (2)$$

Where q is specific discharge, Q is volumetric flow rate, and A is cross-sectional area. As groundwater flows only through pores, the average linear pore water velocity can be calculated using Equation 3.

$$\bar{v} = \frac{Q}{A \times n} = \frac{q}{n} \quad (3)$$

Where $\bar{v}$ is the average linear pore water velocity, Q is the volumetric flow rate, A is the cross-sectional area, and n is the porosity.

### 1.3 Hydraulic Conductivity

Hydraulic conductivity is defined as the proportionality constant between the hydraulic gradient and the Darcy (volumetric) flux and represents the ease with which a fluid can pass through a porous media. The relationship between hydraulic conductivity and fluid and sediment properties is expressed by the following equation:

$$K = k\frac{\rho g}{\mu} = k\frac{g}{\nu} \quad (4)$$

Where K is the hydraulic conductivity, k is the intrinsic permeability, ρ is the fluid density, g is the acceleration due to gravity, and μ is the fluid absolute viscosity. Kinematic viscosity, ν, is defined by the ratio of density over dynamic viscosity, $\nu = \frac{\rho}{\mu}$.

Consequently, there is a linear relationship with slope *k* between kinematic viscosity and hydraulic conductivity.

As seen in Equation 4, the hydraulic conductivity of a fluid is directly proportional to its density and inversely proportional to its viscosity. Viscosity is a fluid's resistance to flow, and fluid density is mass per unit of volume (Freeze & Cherry, 1979; Hillel, 1998). Hydraulic conductivity is a function of fluid properties and the physical properties of the porous media (Sciortino & Leij, 2012). Changes in permeability or soil characteristics will cause changes in hydraulic conductivity. The addition of fluids to a system can alter the viscosity and density, which in turn impact the hydraulic conductivity.

### 1.4 Hydraulic Head

Total hydraulic head, $h$, is defined as an energy state of groundwater flow relative to a datum (Bashir et al., 2007). The hydraulic head is the sum of the pressure head, $\psi$, and elevation head, z (Equation 5).

$$h = \psi + z \quad (5)$$

Elevation head is defined as the point of measurement, whereas pressure head is the length of fluid exerting a force (Freeze & Cherry, 1979). Hydraulic, pressure, and elevation head are expressed in terms of length (L; Freeze & Cherry, 1979). Pressure head increases with depth profile.

## 1.5 Properties of Porous Media

### *1.5.1 Intrinsic Permeability*

Intrinsic permeability, or permeability, is defined as the ease with which a porous media allows fluid to flow through it.

$$k = C \times d^2 \qquad (6)$$

Where k is permeability and *d* is effective mean grain size diameter, C is a proportionality constant that includes physical porous media properties affecting the pore network, including grain size distribution, grain shapes, and grain surface roughness (Equation 6). Permeability impacts fluid velocity. Intrinsic permeability is solely a function of the properties of the porous media.

### *1.5.2 Pore Space and Porosity*

Pore space is the void space that can be filled with fluids (i.e., water, contaminant, air). Total porosity is the portion of porous media that is void space (Equation 7).

$$n = \frac{V_V}{V_T} \qquad (7)$$

Where n is porosity, $V_V$ is the volume of voids, and $V_T$ is the total volume of the porous media. The porosity of sediment depends on many factors, some of which include the following: grain size, grain shape, degree of compaction, and particle size distribution. Porosity, similar to permeability, is a function of the properties of the porous media.

### *1.5.3 Soil Texture and Soil Structure*

Soil texture is a term used to describe the size and size distribution of sediment particles. Sandy soils, loamy soils, and clayey soils are examples of textural classes (Brady & Weil, 1999). Textural classes describe the particle size distribution in terms of relative proportions of sand, silt, and clay size particles and are a fundamental physical property of the soil (Brady & Weil, 1999). Sand has particle diameters between 0.05 mm to 2.00 mm. The broad soil textural classifications are expressed in the soil textural triangle.

Soil structure describes the arrangement of soil particles. Soil structure can be broken down into four shapes: spheroidal, platy, prism, and block (Brady & Weil, 1999). Soil structure and pore patterns impact water movement, porosity, and various aspects of soil.

### *1.5.4 Particle and Bulk Density*

Particle density is the mass per unit volume of soil solids (Equation 8).

$$\rho_p = \frac{M_s}{V_s} \quad (8)$$

Where $\rho_p$ is particle density, $M_S$ is mass of solids, and $V_S$ is volume of solids. Bulk density is the mass of a unit volume of dry soil (Equation 9).

$$\rho_b = \frac{M_T}{V_T} \quad (9)$$

Where $\rho_b$ is bulk density, $V_T$ is total volume, and $M_T$ is total mass. The most distinct difference between particle density and bulk density is that particle density only considers solids, whereas bulk density considers both solids and pore spaces (Brady & Weil, 1999).

Soils with higher bulk densities will have a lower proportion of pore spaces than soils with lower bulk densities. The packing arrangement and sediment uniformity can also impact bulk densities. Higher bulk densities occur in well-graded sands, and lower bulk densities occur in well-sorted sands. The shape of the sediment (i.e., degree of sphericity, roundness) grains also impacts bulk density. Commonly, bulk density increases with depth due to compaction and less aggregation.

### 1.6 Darcy-Buckingham Flux and Richard's Equation

The Darcy-Buckingham flux (Equation 10) that incorporates matric potential, $\psi$, in unsaturated soils is a function of water content, θ. This relation also indicates that the flow of fluid cross-sectional area is proportional to the gradient of matric potential (Fetter, 1999).

$$q = -K(\psi)\frac{\Delta h}{\Delta L} = \frac{-k(\psi)\rho g}{\mu}\frac{\Delta h}{\Delta L} = -K_s K_r(\psi)\nabla(h) \qquad (10)$$

Where $K(\psi)$ is the unsaturated hydraulic conductivity as a function of matric potential and $\nabla(h)$ is the gradient of the total soil water potential.

Richard's equation (Equation 11) is a physically based one-dimensional unsaturated vertical flow equation for porous media.

$$\frac{\delta\theta}{\delta t} = \frac{\delta}{\delta z}\left(K(\psi)\frac{\delta\psi}{\delta z}\right) \quad (11)$$

Where θ is volumetric moisture content and K($\psi$) is hydraulic conductivity as a function of matric potential.

### 1.7 van Genuchten Functions

The van Genuchten (1980) hydraulic functions are widely used for moisture retention and unsaturated hydraulic conductivity relations encompassing water content and soil water pressure head (Equation 12).

$$\Theta = \frac{\theta - \theta_r}{\theta_S - \theta_r} \quad (12)$$

Where Θ is effective saturation, $\theta_r$ is residual water content, and $\theta_S$ is saturated water content. The unsaturated hydraulic conductivity function K($\psi$) and relative unsaturated hydraulic conductivity function $K_r(\psi)$ can be calculated using Mualem's function (Mualem, 1976) applied to the van Genuchten retention function with the conventions $m$ = 1-1/$n$ and $l$ = 0.5 invoked giving Equations 13 and 14.

$$K(\Theta) = K_s K_r(\Theta) = \Theta^{\frac{1}{2}}\left[1 - \left(1 - \Theta^{\frac{1}{m}}\right)^m\right]^2 \quad (13)$$

$$K(\psi) = K_s K_r(\psi) = \frac{\{1 - |\alpha\psi|^{n-1}\ [1 + |\alpha\psi|^n]^{-m}\}^2}{[1 + |\alpha\psi|^n]^{\frac{m}{2}}} \quad (14)$$

## 1.8 Infiltration and Cumulative Infiltration

Infiltration is the process of a fluid entering a porous media. Infiltration rates are affected by many factors including the properties of the fluid (i.e., hydraulic conductivity) and the properties of the porous media (i.e., permeability). Cumulative infiltration is the accumulated volume of fluid over a given period. Infiltration events can be separated into early-time and late-time infiltration events. In porous media, fast early-time infiltration is followed by slower (i.e., decreased slope) late-time infiltration (Beatty & Smith, 2014). On a cumulative infiltration versus time plot, a linear line indicates a non-repellent porous media, and an upward curved line indicates a repellent system (Beatty & Smith, 2014).

## 1.9 Multiphase Flow

### *1.9.1 Interfacial Tension*

A liquid that comes into contact with a substance holds interfacial energy (Fetter, 1999), which is expressed as energy per unit (i.e., Joules/$m^2$ or ergs/$cm^2$). Alternatively and equivalently, interfacial tensions can be expressed as force over a length (i.e., mN/m or dynes/cm) when the fluid mechanics and physics of multiple phase flow are considered. Interfacial tension is the amount of work required to expand the area of the interface by one unit area and/or the mechanical force exerted per unit length of the interface. For two

fluids, or a fluid and a solid surface, the interfacial tension is generated by the difference of the magnitude of inward attraction (cohesion) of molecules to each other compared with the degree of attraction (adhesion) to molecules of the other substance (Fetter, 1999).

### *1.9.2 Capillary Pressure*

The difference in the pressures of the two fluids in contact at the fluid-fluid interface is defined as capillary pressure, $P_C$. The Laplace Equation of Capillarity describes the capillary pressure between two immiscible fluids (*a* and *b*) as a function of the interfacial tension and the curvature of the interface (Equation 15).

$$P_C = P_a - P_b = \sigma\left(\frac{1}{r_1} + \frac{1}{r_2}\right) = \frac{2\sigma}{r} \qquad (15)$$

Where $P_C$ is capillary pressure, $P_a$ is capillary pressure of the nonwetting fluid, $P_b$ is capillary pressure of the wetting fluid, σ is interfacial tension, $r_1$ and $r_2$ are principle radii of curvature of the interface, and r is the equivalent hemispherical radius of curvature of the interface. By convention, capillary pressure of water is a positive value in the vadose zone since water is most commonly the wetting fluid. That is, the capillary pressure is equal to the magnitude of the water pressure in unsaturated soils, which is commonly expressed relative to gauge pressure (atmospheric pressure set as zero reference pressure), and consequently water pressures are negative values. Capillary pressure is directly proportional to the interfacial tension and inversely proportional to the radius of curvature (Equation 15). Therefore, as a fluid infiltrates into a porous media, the smaller pores preferentially fill due to the higher pressure difference, i.e., capillarity (Beatty & Smith,

2013). As expressed in the Laplace Equation of Capillary, any reductions in interfacial tension between two fluids results in decreases in the difference in pressure between the two fluids, i.e., the capillary pressure. As supported by Equation 15, capillary pressure is a function of the pore radius. Therefore, there are greater capillary effects in fine materials (Henry & Smith, 2003).

### *1.9.3 Surface Tension*

Surface tension, σ, is the interfacial tension between a liquid and its vapour. Surface tension is defined as the interface potential energy by interface area (Koorevaar et al., 1983). Interfacial and surface tension cause pressure differences across the curved interface as described by the Laplace Equation of Capillarity (Equation 15). The surface tension interactions between water and ethanol are critical to this work.

### *1.9.4 Contact Angles and Wettability*

The contact angle, θ, is the angle at which the interface between two fluids intersects a solid surface. Young's equation (Equation 16) was the first to quantify the wettability of a solid surface by two fluids based on interfacial tensions, σ (Spencer et al., 2013).

$$\cos\theta = \frac{\sigma_{SG} - \sigma_{Sl}}{\sigma_{Gl}} \qquad (16)$$

Where S denotes solid, l denotes liquid (generally represented as L except for the purpose of this thesis), and G denotes gas. As seen in the equation above, contact angles change proportionally to changing surface tensions (Beatty & Smith, 2014). If the contact angle is

less than 90°, the liquid will preferentially wet the solid, and if the contact angle is greater than 90°, the gas will preferentially wet the solid. The fluid with a contact angle of less than 90° is termed the wetting fluid; the other fluid is termed the nonwetting fluid. In natural porous media, water has the greatest affinity for the solid surface, followed by oil and then air. The contact angle determines wettability. Furthermore, surface chemistry determines the contact angle at the interface.

## 1.10 Flow in the Unsaturated Zone

### *1.10.1 Vadose Zone*

The vadose zone is the unsaturated zone above the capillary fringe and groundwater table. The unsaturated zone is not a source of available water for consumption. However, the unsaturated zone is often a controlling factor in water movement from surface to the groundwater table. In unsaturated porous media, water flow is a function of the characteristics of the porous media (Henry & Smith, 2003).

### *1.10.2 Matric Potential and Volumetric Water Content*

Pressure head or matric potential, $\psi$, is the negative pressure caused by capillarity and is a function of the volumetric water content of a porous media, $\theta$. In the unsaturated zone, the pressure head is less than zero, i.e., less than atmospheric (gauge) pressure (Bashir et al., 2007). This is because the fluid in the unsaturated zone is held within soil pores by surface tension forces (Bashir et al., 2007).

Volumetric moisture content is defined as the volume of water divided by the total volume as described in Equation 17.

$$\theta = \frac{V_w}{V_T} \quad (17)$$

Where θ is volumetric moisture content, $V_W$ is volume of water, and $V_T$ is total volume. In unsaturated systems, volumetric moisture content is less than porosity.

Hydraulic head, pressure head, and gravitational potential head volumetric moisture content are defined using the relationship:

$$h = \psi(\theta) + z \quad (18)$$

Where $h$ is the soil moisture hydraulic head, $\psi$ is pressure head, which in unsaturated porous media is a function of volumetric moisture content, θ is volumetric moisture content, and z is gravitational potential head. The lower the volumetric water content, the lower the pressure head (Equation 18).

### *1.10.3 Characteristic Curves*

Moisture content or soil water characteristic curves define the relationship between pressure head and volumetric water content for a particular soil (Figure 1.1). On the characteristic curve, the sediment is saturated at atmospheric pressure. At this point, the water content is equal to porosity. The moisture content decreases as the pressure head or

matric suction decreases. The characteristic curve continues to decline until minimum residual water content is reached.

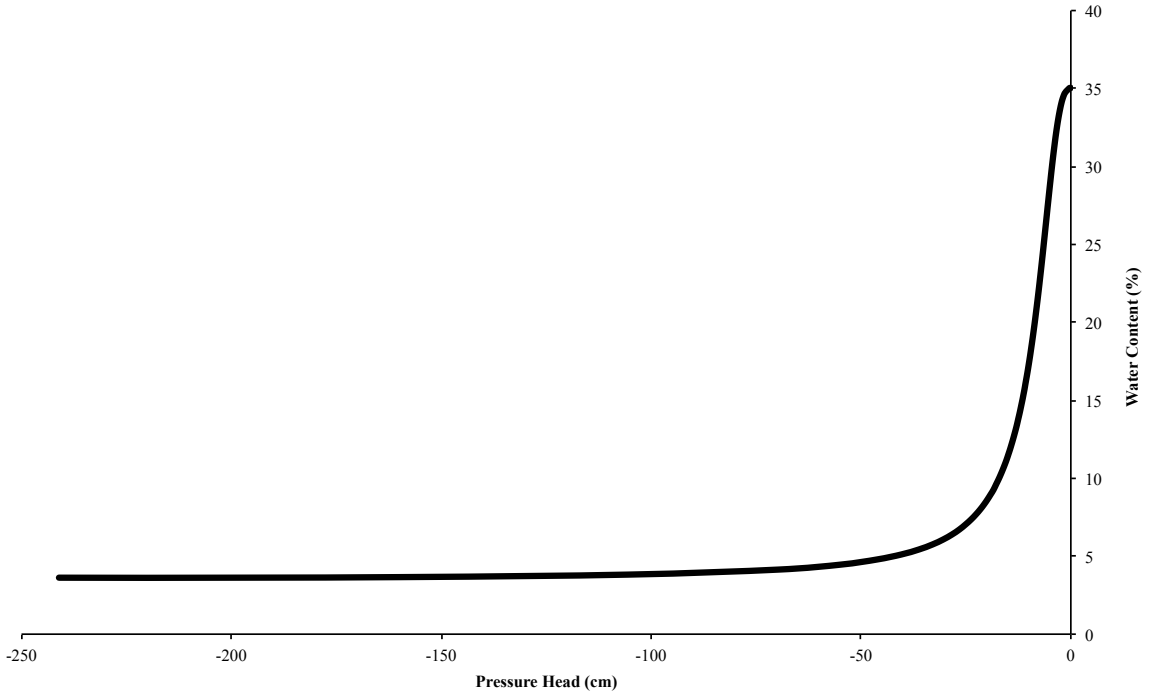


*Figure 1.1.* Schematic of a moisture content characteristic curve for typical sand.

Characteristic curves can provide hydraulic properties (i.e., unsaturated hydraulic conductivities, porosity) and soil properties (i.e., sediment texture, pore size distribution). Characteristic curves with a narrower (pressure head) range indicate well-sorted sediment as the pore sizes have a narrower range. Characteristic curves with a smaller air entry pressure indicate a smaller grain size. Air entry value is defined as the critical matric suction value that must be exceeded before air enters the previously fluid-filled pore space (Hillel, 1998). The air entry value is inversely proportional to the pore radius of the largest pores (Hillel, 1998). Air entry values can be determined through characteristic curves.

## 1.11 Ethanol

Ethanol, or ethyl alcohol, is alcohol (organic compound) with the chemical formula $C_2H_5OH$ (Table 1.1). Ethanol is a colourless liquid with both volatile and flammable properties. Ethanol is produced through the fermentation of various sugars and yeasts, some of which include sugar cane, corn, and wood (Alvarenga & Dewulf, 2013; Lee, 2008). Ethanol has a low impact to human health (Freitas & Barker, 2013a) and has a low affinity to mineral surfaces (Freitas & Barker, 2013b; Powers et al., 2001).

Table 1.1. Comparison of properties of ethanol and water-chemical formula, molar mass, and boiling point (Kadlec, Henke, & Bubnik, 2010; Lide, 1993).

| | **Chemical Formula** | **Molar Mass** | **Boiling Points** | **Freezing Points** |
|---|---|---|---|---|
| | | **g/mol** | **°C** | **°C** |
| **Water** | $H_2O$ | 18.02 | 100 | 0 |
| **Ethanol** | $C_2H_6O$ | 46.07 | 78.29 | -114.1 |

In recent decades, the demand for ethanol and the uses for ethanol have been increasing. Ethanol use has been rising for many reasons, one of which includes meeting increasing fuel needs and renewable fuel requirements (Cápiro et al., 2007; Sciortino & Leij, 2012). Most commonly, ethanol is widely used as a fuel source—both in biofuels and gasoline—pharmaceuticals, bio-based plastics, and industrial solvents (Alvarenga & Dewulf, 2013; Cápiro et al., 2007; Lee, 2008; Powers et al., 2001; Stafford et al., 2009). Not only is ethanol increasingly being used, its use as an additive to other compounds (Freitas & Barker, 2013a; Lee, 2008) is becoming more widespread. Denatured ethanol is typically used in solvents and as additives to gasoline and is not suitable for human consumption (Freitas & Barker, 2013a).

Ethanol is a cosolvent: a solvent that when combined with another solvent is able to dissolve a solute. As ethanol concentration increases, so does the strength of the cosolvent; to be specific, ethanol increases the solvency of hydrocarbons (Freitas & Barker, 2013a; Freitas & Barker, 2013b). Ethanol is miscible in gasoline, and the presence of ethanol makes water and gasoline completely miscible (Lee, 2008; Powers et al., 2001). Ethanol for use as a gasoline additive has been increasing. Due to the hydroscopic properties of ethanol gasoline, ethanol is transported separately to distribution terminals and combined before distribution (Powers et al., 2001; Stafford et al., 2009). This increase in the use of ethanol warrants increased storage of ethanol, which could result in underground storage tanks leaking (Stafford et al., 2009). Ethanol is added to gasoline as an oxygenate; the addition of ethanol increases the octane rating and decreases the air pollution (Freitas & Barker, 2013b; Powers et al., 2001; Sciortino & Leij, 2012). Ethanol as a solvent is also used in remedial solvent flushing (Freitas & Barker, 2013a). Ethanol can affect the fate, distribution, and transport of other contaminants in the same area due to its physical properties (Freitas & Barker, 2013a; Lee, 2008; Powers et al., 2001). Other gasoline additives are also used, such as methyl tert-butyl ether; however, as the impacts of ethanol are less harmful, the use of ethanol as a gasoline additive is increasing (Powers et al., 2001).

Ethanol can biodegrade under both aerobic and anaerobic conditions. Low concentrations of ethanol biodegrade, whereas high concentrations of ethanol kill the microorganisms in the subsurface (Powers et al., 2001). Ethanol ($C_2H_6O$) degradation produces methanol

($CH_4O$) and methane ($CH_4$). The byproducts produced in ethanol biodegradation are not toxic (Powers et al., 2001). The presence of ethanol causes lower biodegradation of hydrocarbons (Powers et al., 2001).

## 1.12 Ethanol and Water

### *1.12.1 Physical Properties*

The relationship between ethanol and water is unique. Ethanol is miscible (soluble) in water as well as other organic solvents. Ethanol is more viscous and less dense than water (Table 1.2; Figure 1.2, 1.3); therefore, ethanol has a lower hydraulic conductivity. As ethanol concentration increases linearly, fluid mobility shows a nonlinear pattern (Table 1.3; Figure 1.4; Beatty & Smith, 2014). The lower the fluid mobility factor, the slower the infiltration rate (Beatty & Smith, 2014).

Under the same fluid content, aqueous solutions of ethanol are less mobile than water (Table 1.3; Figure 1.4; Beatty & Smith, 2014). Ethanol affects both the surface tension and viscosity of water as a function of concentration (Figure 1.2). As ethanol concentration increases, the surface tension decreases (Figure 1.2; Sciortino & Leij, 2012; Spencer et al., 2013). Decreases in surface tension due to ethanol concentration produces a less negative pressure head; therefore, relative to water, fewer pores are filled at a given pressure head (Sciortino & Leij, 2012). Ethanol and ethanol solutions have lower air/liquid interfacial (surface) tensions and apparent contact angles compared to water (Table 1.2; Equation 15; Beatty & Smith, 2014). This means the presence of ethanol

lowers the surface tension of water. A study by Spencer et al. (2013) observed that as ethanol concentration increases in ethanol-water mixtures, the contact angle decreases. Most importantly, both water and ethanol solutions are temperature sensitive.

Table 1.2. Physical properties of 0% to 100% ethanol-density, dynamic viscosity, kinematic viscosity, and surface tension at 20°C (Beatty & Smith, 2014; Kadlec, Henke, & Bubnik, 2010; Lide, 1993).

| | **Density at 20°C** | **Dynamic Viscosity at 20°C** | **Kinematic Viscosity at 20°C** | **Surface Tension at 20°C** |
|---|---|---|---|---|
| **%** | **kg/m$^3$** | **Pa•s** | **m/s$^2$** | **mN/m** |
| **0** | 998.20 | 0.00089 | 8.92E-07 | 72.01 |
| **10** | 981.84 | 0.00150 | 1.53E-06 | 47.53 |
| **20** | 968.61 | 0.00214 | 2.21E-06 | 37.97 |
| **30** | 953.79 | 0.00267 | 2.80E-06 | 32.98 |
| **40** | 935.15 | 0.00285 | 3.04E-06 | 30.16 |
| **50** | 913.81 | 0.00281 | 3.08E-06 | 27.96 |
| **60** | 891.10 | 0.00255 | 2.86E-06 | 26.23 |
| **70** | 867.63 | 0.00221 | 2.55E-06 | 25.1 |
| **80** | 843.41 | 0.00188 | 2.23E-06 | 23.82 |
| **90** | 817.95 | 0.00154 | 1.89E-06 | 22.72 |
| **96** | 808.21 | 0.00134 | 1.66E-06 | - |
| **100** | 789.24 | 0.00120 | 1.51E-06 | 22.8 |

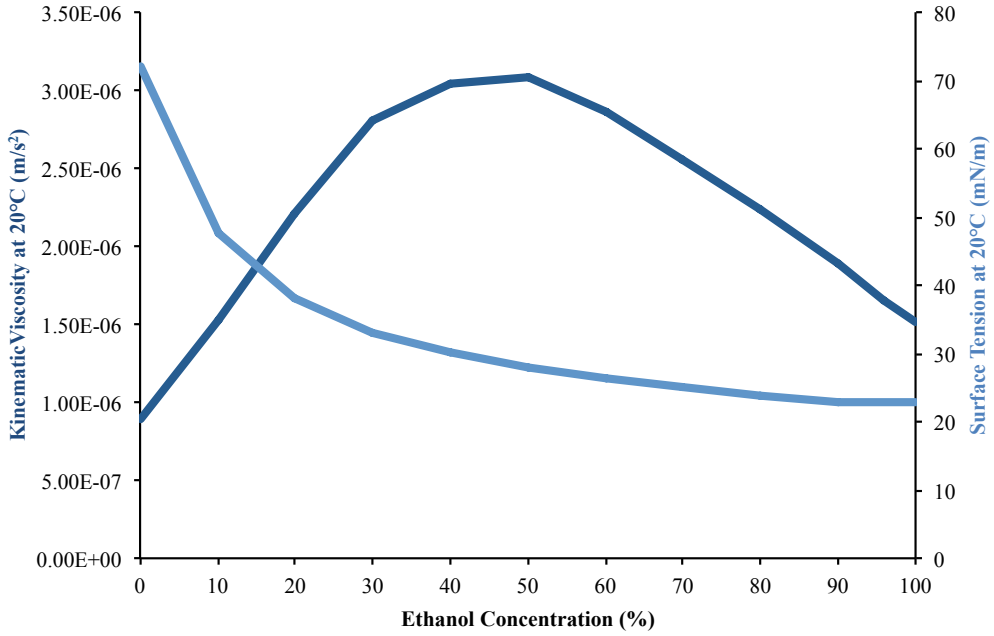


*Figure 1.2.* Kinematic viscosity (ν) and surface tension (σ) at 20°C for aqueous concentrations of ethanol (Kadlec, Henke, & Bubnik, 2010; Lide, 1993).

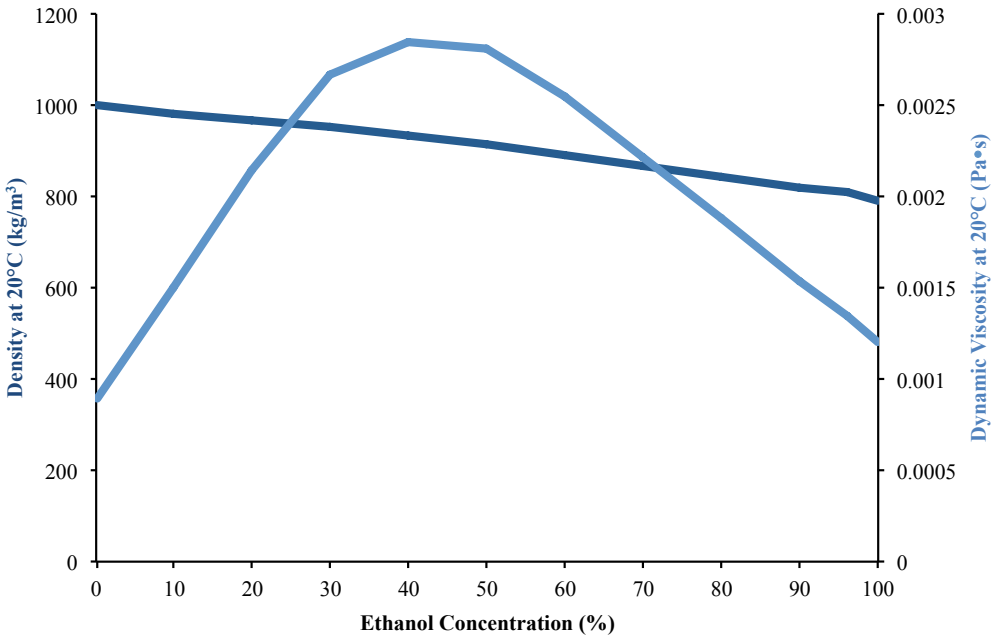


*Figure 1.3.* Density (ρ) and dynamic viscosity (μ) at 20°C for aqueous concentrations of ethanol (Kadlec, Henke, & Bubnik, 2010; Lide, 1993).

Table 1.3. Physical properties of 0% to 100% ethanol-fluid mobility and inverse fluid mobility at 25°C (Beatty & Smith, 2014).

| % | Fluid Mobility at 25°C | Inverse Fluid Mobility at 25°C |
|---|---|---|
| **0** | 1 | 1 |
| **10** | 0.6632 | 1.508 |
| **20** | 0.4771 | 2.096 |
| **40** | 0.3548 | 2.818 |
| **50** | 0.3550 | 2.817 |
| **60** | 0.3547 | 2.819 |
| **80** | 0.4297 | 2.327 |
| **100** | 0.6577 | 1.520 |

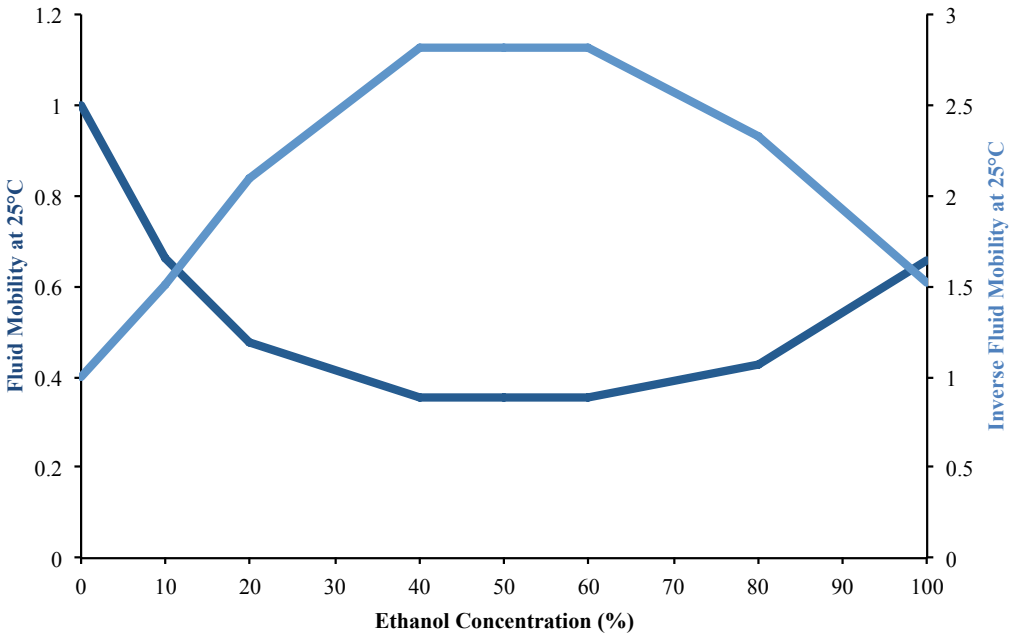


*Figure 1.4.* Fluid mobility and inverse fluid mobility at 25°C for aqueous concentrations of ethanol (Beatty & Smith, 2014).

### *1.12.2 Fundamental Relationships*

Aqueous solutions of ethanol have concentration-dependent capillary pressures (Equation 19) or pressure heads (Equation 20) and hydraulic conductivities (Equation 21). The following relationships and scaling relations are fundamental in the unsaturated zone:

$$P_{Ce} = \frac{\sigma_e}{\sigma_w} P_{Cw} \qquad (19)$$

In Equation 19, $P_C$ denotes capillary pressure and σ denotes interfacial tension. Subscripts "e" and "w" denote ethanol and water, respectively. Capillary pressure and interfacial tension for a given fluid are directly proportional. The ratio of interfacial tension $\left(\frac{\sigma_e}{\sigma_w}\right)$ is the scaling term used to scale the capillary pressure of water to the capillary pressure of ethanol (Henry et al., 2002; Smith & Gilham, 1999).

$$\psi_e = \frac{\sigma_e/\rho_e}{\sigma_w/\rho_w} \psi_w \qquad (20)$$

Pressure head is directly proportional to the interfacial tension of a fluid and inversely proportional to the density of a fluid. The scaling relation for Equation 20, $\left(\frac{\sigma_e/\rho_e}{\sigma_w/\rho_w}\right)$, used interfacial tension and density to scale the pressure head of water to the pressure head of ethanol. Equations 19 and Equation 20 have capillary pressure components that have solute-concentration dependence.

$$K_e = \frac{\nu_w}{\nu_e} K_w \qquad (21)$$

In Equation 21, K denotes concentration-dependent hydraulic conductivity and ν denotes kinematic viscosity. For a given fluid, the hydraulic conductivity is inversely proportional to the kinematic viscosity. As kinematic viscosity for a given fluid increases, the hydraulic conductivity decreases. The kinematic viscosity ratio, $\left(\frac{\nu_w}{\nu_e}\right)$, scales the water-wet hydraulic conductivity to determine the ethanol-wet hydraulic conductivity (Henry et al., 2002). Kinematic viscosity and hydraulic conductivity both depend on ethanol concentration (Equation 21). The relationship between pressure head, surface tension, density, and contact angle come together in Equation 22.

$$\psi_e = \frac{\left({}^{\sigma_e}/_{\rho_e}\right)cos\beta_e}{\left({}^{\sigma_w}/_{\rho_w}\right)cos\beta_w}\psi_w \qquad (22)$$

### *1.12.3 Scaled Curves for Water and Ethanol*

The concept of scaling terms and scaling relationships has been successfully used in many scientific works (Bashir et al., 2008; Bashir et al., 2011; Henry et al., 2002; Henry & Smith, 2003; Miller & Miller, 1956; Sciortino & Leij, 2012; Smith & Gilham, 1999). Scaling relationships are defined as the adjustment of the relationship along the pressure head axis (Henry & Smith, 2003). The scaling of moisture content characteristic curves along the pressure head axis is done by multiplying the pressure head by the ratio of surface tension (Henry & Smith, 2003). Bashir et al. (2008), Henry et al. (2002), and Smith and Gilham (1999) used such scaling relationships for 7% butanol solutions.

### *1.12.4 Primary Concentration-Dependent Effects*

The SCIFF event investigated in this thesis is primarily due to the decreases or induced changes in interfacial tension at the air-liquid interfaces in the unsaturated sand as a function of ethanol contamination. The presence of antecedent ethanol decreases the surface tension of water (Table 1.2), thereby decreasing the interfacial tension at the water-ethanol interface. The changes in surface tension affect capillary pressure gradients (Equation 19; Smith et al., 2011). The idea follows from Equations 19 and 20 that the capillary pressure component of the hydraulic gradients will have solute-concentration dependence (i.e., will be coupled to the ethanol-concentration gradient). The pressure gradients increase during times of drainage within the system (Henry & Smith, 2002). The moisture content characteristic curve (Figure 1.5) is concentration-dependent through surface tension. This relationship creates conditions where higher ethanol content but lower moisture content porous media has higher capillary pressures (higher magnitude pressure heads) than adjacent higher moisture content porous media that have lower ethanol contents (Figure 1.5).

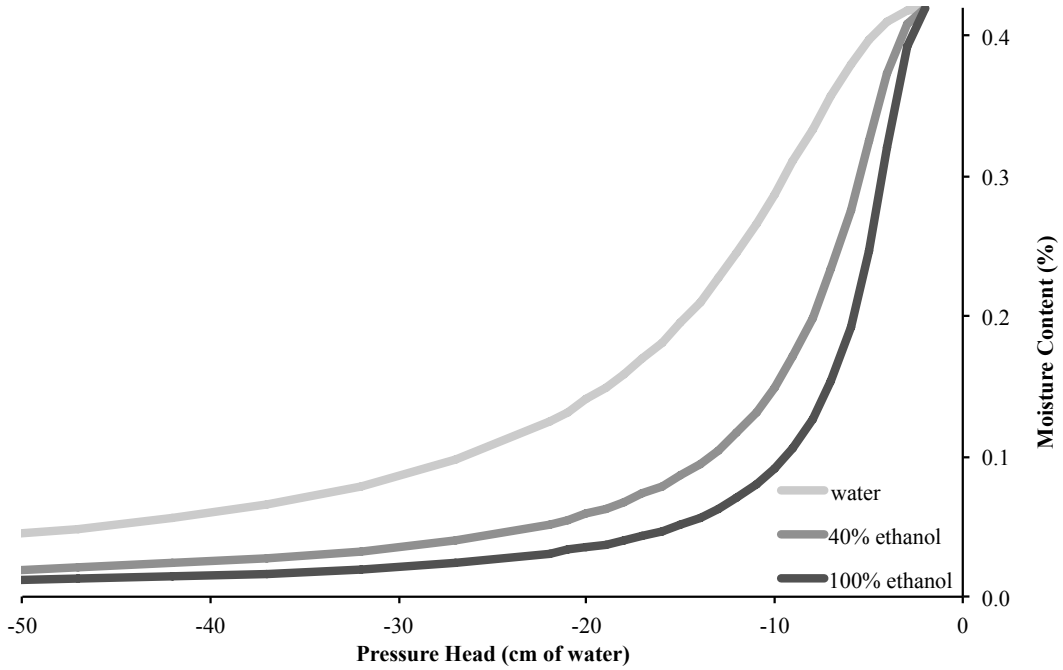


*Figure 1.5.* Moisture content vs. pressure head for water, 40% ethanol and 100% ethanol scaled by surface tension.

### *1.12.5 Secondary Concentration-Dependent Effects*

There are two secondary concentration-dependent effects. The first effect is through the kinematic viscosity scaling of unsaturated hydraulic conductivities. The second effect is the reduction in the gravitational potential (or elevation head) through the dependence of aqueous density (or specific weight) on ethanol concentration and the related buoyant forces during fluid displacements.

Concentration-dependent unsaturated hydraulic conductivity was scaled by kinematic viscosity (Equation 21) for moisture content (Figure 1.6). For given moisture contents, 40% ethanol has the lowest unsaturated hydraulic conductivity and pure water has the highest unsaturated hydraulic conductivity (Figure 1.6). This relationship stems from the

nonlinear relationship of kinematic viscosity for linearly increasing ethanol concentration (Figure 1.2).

A numerical investigation presented by Sciortino and Leij (2012) assessed the impact of surface tension, kinematic viscosity, and density on ethanol flow in the unsaturated zone for constant flux and constant head applications. During constant head application, kinematic viscosity had the most significant impacts on water movement in an ethanol-contaminated system; this was followed by surface tension and density, respectively (Sciortino & Leij, 2012). Surface tension and kinematic viscosity had the most significant impacts on liquid movement during constant flux scenarios (Sciortino & Leij, 2012). Density had the least significant impacts in numerical simulations of both constant flux and constant head ponding scenarios (Sciortino & Leij, 2012). Additionally, the numerical modelling showed that during ponding scenarios, 50% ethanol concentration is the slowest, primarily due to viscosity. This is supported by the nonlinear relationship between kinematic viscosity and ethanol concentration (maximum of 40% to 50%) on Figure 1.2.

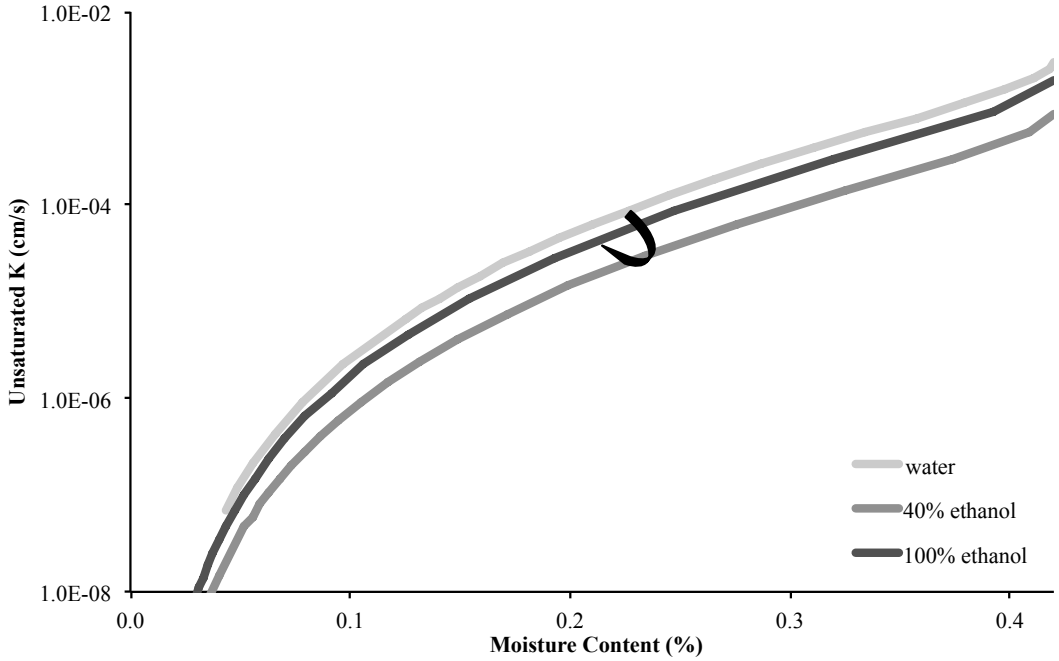


*Figure 1.6.* Unsaturated hydraulic conductivity curves for water, 40% ethanol and 100% ethanol scaled by kinematic viscosity.

### *1.12.6 The Sludge Effect*

The "sludge effect" is a solute transport term coined by Beatty and Smith (2014) that describes a zone of lower mobility than either the antecedent ethanol or the infiltrating water. As concentration of ethanol increases linearly, the associated viscosity is nonlinear (Figure 1.2; Table 1.2); therefore, 50% ethanol solutions have higher viscosities than either ethanol or water. The sludge effect can have impacts on fluid mobility within the mixing zones.

## 1.13 Ethanol, Water, and the Subsurface

The unique physical properties of ethanol and water impact the interactions that ethanol and ethanol solutions have on the capillary fringe and water table.

### *1.13.1 Ethanol, Water, and the Water Table*

The presence of ethanol decreases the surface tension of water (Figure 1.2); therefore, fluctuations in the water table occur when ethanol or ethanol solutions reach the water table (Stafford & Rixey, 2011). These fluctuations further mobilize the ethanol and increase the spreading of ethanol in the saturated zone as ethanol has a high affinity for pore water (Cápiro et al., 2007; Freitas & Barker, 2013a).

The work presented by Cápiro et al. (2007) described the large-scale release and transport of gasoline (E95) at the water table. Phase separation occurred between the gasoline and ethanol; the ethanol component of the gasoline migrated upwards from the water table to the capillary fringe and slowly spread laterally along the capillary fringe (Cápiro et al., 2007; Freitas & Barker, 2013a; Stafford et al., 2009). The nonaqueous phase liquid (NAPL) component remained close to the injection point but below the water table (Freitas & Barker, 2013a; Stafford et al., 2009). Ethanol had minor impacts to groundwater in this study (Cápiro et al., 2007; Stafford et al., 2009).

### *1.13.2 Ethanol, Water, and the Capillary Fringe*

The capillary fringe is the saturated zone above the water table where pressure is less than atmospheric (Freeze & Cherry, 1979; Silliman et al., 2002). Due to the physical properties of ethanol (buoyant forces due to density; Table 1.2), ethanol can accumulate above the capillary fringe and water table (Cápiro et al., 2007; Freitas & Barker, 2011; Stafford et al., 2009). Concentrations of ethanol can dissolve in the capillary fringe and become

trapped. The presence of lower surface tension ethanol in the subsurface decreases the capillary pressure, which decreases the height of the capillary fringe (Cápiro et al., 2007; Freitas & Barker, 2013a; Henry & Smith, 2003; Stafford et al., 2009). Furthermore, fluids with lower air entry pressures will have lower capillary pressures (Henry & Smith, 2003).

The work presented by Silliman et al. (2002) observed that the capillary fringe plays a critical role in the transport of contaminants to the water table and that flow occurs between the capillary fringe and water table. Heterogeneities enhance the two-way exchange between the two zones and flow in the capillary fringe in the porous media (Silliman et al., 2002). However, the capillary fringe plays a minimal role in flow on a regional scale.

Freitas and Barker (2013a, 2013b) used two large-scale, controlled releases to understand the impacts of a denatured ethanol release on a residual gasoline release. The results showed that only ethanol remained and accumulated in the capillary fringe and vadose zone due to the physical properties of the ethanol, specifically the low density (Freitas & Barker, 2011; Freitas & Barker, 2013a; Freitas & Barker, 2013b; Stafford et al., 2009). The ethanol levels in the unsaturated zone fluctuated with water-table oscillations, further supporting the work of Cápiro et al. (2007; Freitas & Barker, 2013a). As a cosolvent, the ethanol release caused redistribution of the residual NAPL; however, the ethanol release did not cause significant transport of hydrocarbons (Freitas & Barker, 2013a; Freitas & Barker, 2013b; Powers et al., 2001; Stafford et al., 2009). The hydrocarbons remained at

deeper positions in the system, and the effects of all contaminants to groundwater were minimal (Freitas & Barker, 2011; Freitas & Barker, 2013b; Powers et al., 2001; Stafford et al., 2009). The work presented by Stafford et al. (2009) further suggested that ethanol is constrained within the capillary fringe due to mass transfer limitations between the capillary fringe and groundwater.

The pilot-scale gasoline and ethanol releases presented by Freitas and Barker (2011) compared three methods of groundwater quality sampling for contaminants in the capillary fringe. Their findings showed that suction samplers and soil cores were the best way to sample for volatile compounds. The findings also showed that ethanol concentration was two times higher in the capillary fringe than below the water table; these findings have since been further supported (Freitas & Barker, 2011; Freitas & Barker, 2013a; Freitas & Barker, 2013b).

### *1.13.3 Ethanol, Water, and the Unsaturated Zone*

The surface tension of ethanol can have significant effects on unsaturated flow in porous media (Smith & Gilham, 1999). The lower the surface tension of the fluid, the larger the shift in pressure-head values (Smith & Gilham, 1999). Surface tension does not always remain constant as pressure head changes in the system (Smith & Gilham, 1999). As surface tensions change, hydraulic gradients within the system are induced.

## 1.14 Focused Flow

Preferential or focused flow is the enhanced flux of water or solute passage through porous media as a result of physical fluid or sediment properties. Focused flow events are manifested as narrow, vertically oriented flow patterns or fingers. The vertical focused flow takes the preferential pathway through the system, the path of least resistance. As the infiltrating fluid (water) continues through the preferential pathway, less antecedent fluid is being caught or mixed down the flow pathway. Gravity is the primary driver, and surface tension and capillarity are the stabilizers of the focused flow vertical movement (Smith et al., 2011).

The experimental work by Chouke et al. (1959) was the first to show interfacial instability due to viscosity differences. Parlange and Hill (1976) concluded that finger size is dependent on soil properties: wider fingers will be observed in finer sediment textures and when initial moisture content is higher. Glass et al. (1989b) used a moisture content visualization technique to further understand finger persistence in unsaturated porous media. The major finding of their work was that fingers could persist during multiple wetting and drying cycles (Glass & Steenhuis 1984); during this time, the fingers remain similar with changes as a result of air entrapment due to initially wet porous media (Glass et al., 1989b). The tips of the fingers have the largest moisture content, with the lowest moisture content in the fringe area (Glass et al., 1989b). Focused flow fingers can merge, and in the long-term, there will be horizontal movement of fluid around the focused flow

fingers (Glass et al., 1989a). Glass et al. (1989a; 1989c) further supported this work by observing that the wider the finger, the faster the finger moves.

The work by Glass et al. (1989a) shows that in a multi-finger scenario, the most rapidly growing finger does not indicate that finger will dominate. The findings went on further to show that the coarser the porous media, the smaller the minimum finger width that can occur (Glass et al., 1989a). Changes in fluid properties affect finger width and velocity; specifically, decreases in surface tension can decrease finger width (Glass et al., 1989a). As the flow rate increases through the finger, finger width also increases (Glass et al., 1989a). At the finger scale, as finger flow increases, so does the width, velocity, and moisture content of the finger (Glass et al., 1989c). Zhang and Smith (2002) conducted a series of dense nonaqueous phase liquid (DNAPL) infiltration experiments in glass beads, which determined that the DNAPL finger elongates from the tip of the finger and moves down a more winding path when compared to butanol-contaminated systems (Smith & Zhang, 2001; Smith et al., 2011).

Smith et al. (2011) presented SCIFF with water infiltration into antecedent butanol-contaminated sand. The authors hypothesized that SCIFF should be active for all aqueous surfactants or solutes with capillarity effects, such as alcohols. SCIFF manifests as an unsaturated flow phenomenon of infiltrating water in highly focused, vertical flow finger with minimal lateral migration into antecedent butanol-contaminated sand (Smith et al.,

2011). The results concluded that alcohol concentration induced the reduction in surface tension and moisture content in the SCIFF (Smith et al., 2011).

### 1.15 Focused Flow and Heterogeneity

Heterogeneity is a term used to describe porous media that is not uniform in nature. Focused flow events can be common in heterogeneously layered systems (Glass and Steenhuis, 1984; Glass et al., 1989b). Heterogeneity of porous media has a strong influence on the direction that finger growth takes (Glass et al., 1989c). In multiple finger scenarios, heterogeneities can cause fingers to merge. These merged fingers form faster and wider fingers (Glass et al., 1989c). Focused flow develops at textural interfaces in heterogeneous systems (Glass et al., 1989c), more specifically, in systems where finer texture porous media overlays coarser texture porous media.

### 1.16 Hysteresis

Hysteresis is the nonlinear relationship between water saturation and capillary pressure (Figure 1.7; Miller & Miller, 1956). The hysteretic relationship is a time scale invariant of capillary pressure. Hysteresis is the change in behaviour based on history within the system. The hysteretic relationship is defined by drainage and wetting curves (Figure 1.7). The drainage or drying curve is obtained by desorbing water via increased suction from an initially saturated porous media. The wetting curve is obtained by re-saturating the sediment via decreased suction. At 100% saturation, the slope of the drainage curve (also termed the soil water retention curve) is low; at this point, the capillary pressure is low

and the largest pores are draining first. As capillary pressure becomes more negative, the saturation of the wetting fluid decreases, and there is an increase in the saturation of the nonwetting fluid. At lower water saturation, the relative change in capillary pressure is higher. Smaller pores drain when the relative change in capillary pressure is high. Pores fill and drain preferentially according to pore size (Beatty & Smith, 2013). Residual wetting fluid remains in the porous media (the porous media never fully drains). Along the wetting curve, the pores with the lowest pressure saturate first (Beatty & Smith, 2013). Residual nonwetting fluid remains entrapped in the porous media (the porous media never fully saturates) as disconnected ganglia (Fetter, 1999). Porous media can follow any intermediate drainage or wetting curve; these curves are referred to as scanning curves (Figure 1.7). Many factors influence the effect of hysteresis, some of which include the irregular and composite shapes of soil pores (Koorevaar et al., 1983).

Ethanol has a lower surface tension than water (Equation 19); therefore, a lower capillary pressure is required to sustain the ethanol-air hysteretic relationship than the water-air hysteretic relationship. Fingers or preferential flows persist due to hysteretic relationships (Glass et al., 1989b).

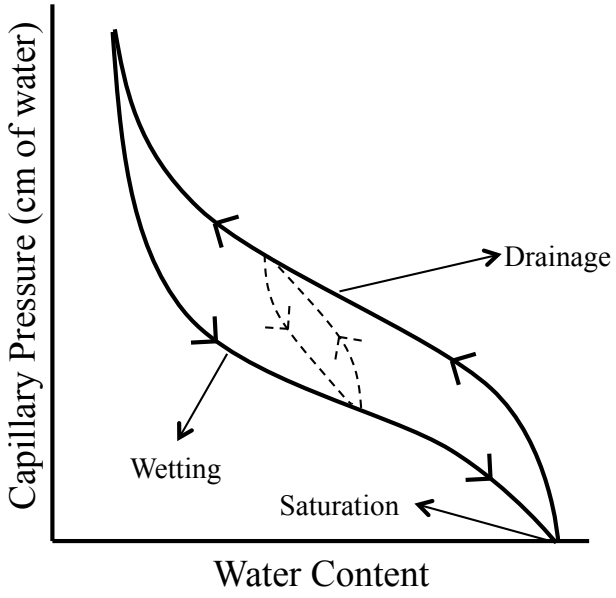


*Figure 1.7.* Schematic of a hysteretic curve depicting the drainage and wetting curves.

# 2 Thesis Overview

## 2.1 Research Goals

The purpose of this research is to improve the understanding of focused flow infiltration behaviours of water into ethanol-contaminated unsaturated porous media. This thesis aims to achieve the following:

(i) use highly controlled laboratory experiments in a two-dimensional (2-D) flow cell to demonstrate and better understand the focused flow infiltration behaviours using constant flux and constant head application methods

(ii) compare and contrast the differences and similarities between the application methods

(iii) further understand the mechanisms present in ethanol-water contaminated unsaturated sand systems.

### 2.2 Thesis Organization

This thesis is organized into three sections. Section 3 focuses on the focused flow infiltration experiments using constant flux application. Focused flow infiltration experiments using constant head application are the focus of Section 4. Section 5 focuses on the unique findings of this research.

## 3 Constant Flux

### 3.1 Introduction

Groundwater flux is defined as the rate of flow, or discharge, [$L^3/T$] per unit area [$L^2$], given the dimensions of [L/T]. Constant flux is a constant volume of droplets applied to the surface per unit time to mimic constant rainfall rate in real-life scenarios (Sciortino & Leij, 2012).

Many assumptions were made during experimental design and analysis. These assumptions include, but are not limited to, the following:

- Ambient temperature fluctuations are negligible,
- Steady-state conditions were achieved,
- The porous media is inert,
- Biodegradation, evaporation, and volatilization of ethanol is negligible, and
- Evaporation of water is negligible.

## 3.2 Study Objectives and Hypothesis

### *3.2.1 Study Objectives*

The primary objective of this research was to conduct a series of highly-controlled 2-D unsaturated flow cell experiments with constant flux application to the surface to demonstrate, characterize, and quantify focused flow behaviour of water infiltrating into ethanol-contaminated porous media.

### *3.2.2 Hypothesis*

The primary hypothesis of this research was that the infiltration of water using constant flux onto the surface of ethanol-contaminated unsaturated porous media would produce a narrowly focused vertical flow infiltration pattern. It was further hypothesized that this behaviour would be primarily due to the decreases in interfacial tensions at the air-liquid interfaces within the unsaturated sands as a function of ethanol concentration.

A secondary hypothesis was that the application of ethanol by constant flux onto water-wetted unsaturated porous media would produce a stable semicircular infiltration pattern below the application area.

## 3.3 Experimental Design and Methods

### *3.3.1 Apparatus*

#### *3.3.1.1 Flow Cell*

The 2-D infiltration experiments were carried out in a 2-D brass and glass flow cell (0.6 m by 0.5 m by 0.01 m). The glass plates had a thickness of 0.01 m and were sealed to the brass frame by Viton chord compression. The flow cell (Figure 3.1) was made of two panes (front and back) of glass held together by a brass metal frame with two outlet ports, one on each side 0.01 m above the base. The glass plates allowed visual inspection and recording of images of infiltration events. The flow cell was positioned with flat black background to create even backlighting and to minimize reflections in photographs.

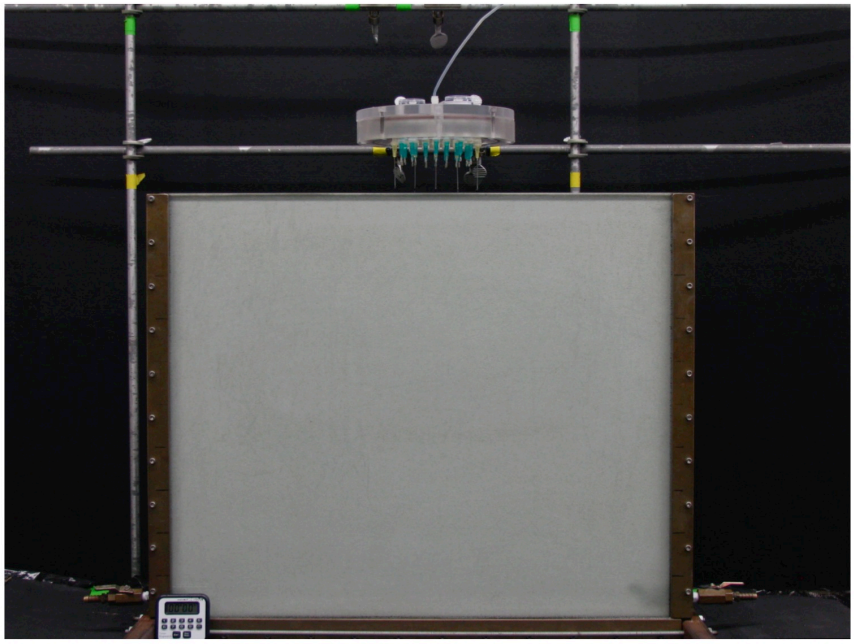

*Figure 3.1.* The glass plate flow cell (0.6 m by 0.5 m by 0.01 m) with a constant flux rainulator positioned above.

#### *3.3.1.2 Rainulator*

A rainulator with a row of five hypodermic needles was attached to a peristaltic pump for the constant flux application experiments (Figure 3.2) to simulate constant-rate rainfall. The needles were 2 cm apart, giving an application length of 8 cm. The rainulator applied ethanol and water to 13.3% of the total width of the flow cell. The needles were 23 gauge × 1 in. (2.54 cm; Becton Dickinson) and 20 gauge × 1½ in. (3.81 cm; Becton Dickinson), depending upon the desired application rate. The rainulator was secured to a laboratory metal support frame structure using two 3-prong clamps. The level of the rainulator was checked after securing the instrument and was continuously monitored during fluid application. The rainulator was thoroughly rinsed with distilled water after each phase of the experiment.

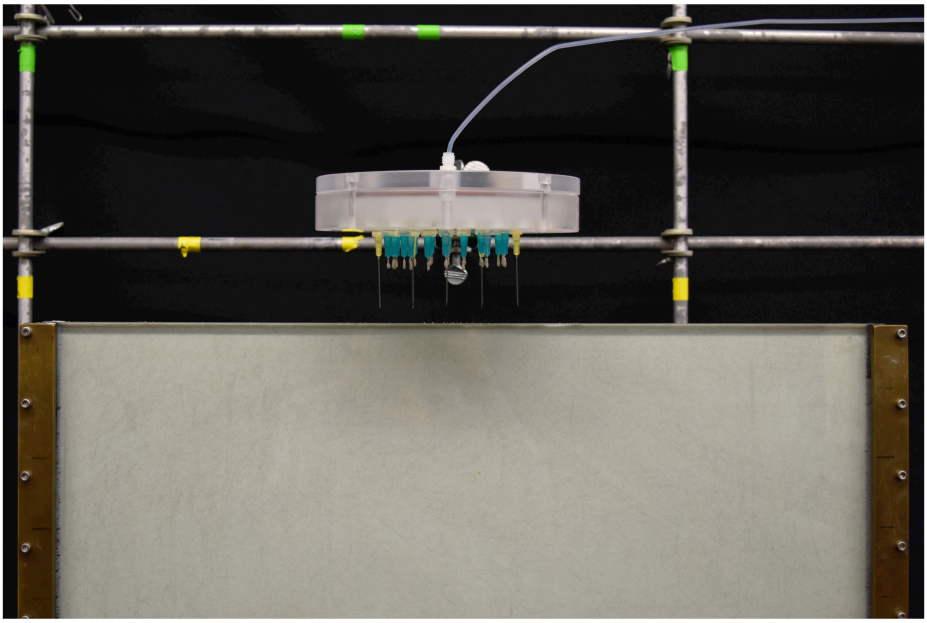

*Figure 3.2.* The constant flux rainulator with a row of hypodermic needles positioned above the flow cell.

#### *3.3.1.3 Camera*

A Canon PowerShot SX100 IS camera secured to a Velbon CX-540 camera tripod was connected to a desktop PC. This camera setup was covered using flat black fabric to prevent reflection in the photographs.

#### *3.3.1.4 Materials*

The two sand types used in the experiments were OOO Ricci Bros Sand Co., Inc. CAS #14808-60-7 (Ricci sand) and Opta Minerals BARCO M49 Quartz Silica 49-7-15 (Opta sand). The Ricci sand is a medium-brown coloured sand, and the Opta sand is a coarser, light-tan coloured sand (Table 3.1). The typical sand gradation for the Opta sand and Ricci sand are included in Table 3.2 and Table 3.3, respectively. The properties of these sands are listed in Table 3.1. The two fluids used during the experiments were room temperature deionized water and 95% by volume ethyl alcohol. The deionized water was de-aired for 24 hrs before the experiment.

Table 3.1. Sand properties for the two experimental sands used: OOO Ricci Bros Sand Co., Inc. (Ricci Bros. Sand Co., 2018) and Opta Minerals Quartz Silica 49-7-15 (McLeod, 2015; Opta Minerals, 2018).

| **Sand Properties** | **Units** | **OOO Ricci Bros Sand Co., Inc.** | **Opta Minerals Quartz Silica 49-7-15** |
|---|---|---|---|
| **Colour** | - | Gray/Brown | White |
| **Mineral** | - | Sand/Gravel | Quartz |
| **Solubility** | - | - | Insoluble |
| **Specific Gravity** | g/cc | 2.6 | 2.65 |
| **Grain Size** | - | - | Rounded |
| **Bulk Density** | $lbs/ft^3$ | 100 | 99 |
| **Hardness** | Mohs | 7 | 7 |

Table 3.2. Opta Minerals Silica Quartz 49-7-15 typical gradation. Adapted from Opta Minerals (2018).

| U.S. Mesh | Microns | Percent | |
|---|---|---|---|
| | | Retained | Passing |
| 20 | 850 | 0.0 | 100.0 |
| 30 | 600 | 0.2 | 99.8 |
| 40 | 425 | 13.9 | 85.9 |
| 50 | 300 | 30.6 | 55.3 |
| 70 | 212 | 33.2 | 22.1 |
| 100 | 150 | 15.7 | 6.4 |
| 140 | 106 | 5.5 | 0.9 |
| 200 | 75 | 0.9 | 0.0 |
| 270 | 53 | 0.0 | 0.0 |
| Pan | 0 | 0.0 | 0.0 |

Table 3.3. OOO Ricci Bros Co., Inc. typical gradation. Adapted from Ricci Bros. Sand Co., Inc. (2018).

| ASTM E11 Sieve # | Microns | Percent Passing |
|---|---|---|
| 25 | 710 | 100 |
| 30 | 600 | 99 |
| 35 | 500 | 99 |
| 40 | 420 | 90 |
| 45 | 360 | 70 |
| 50 | 300 | 56 |
| 60 | 250 | 35 |
| 70 | 210 | 24 |
| 80 | 180 | 10 |
| 100 | 150 | 4 |

### *3.3.2 Methods*

#### *3.3.2.1 Experimental Design*

The experiment was run on two sand textures, a finer sand texture (Ricci sand) and coarser sand texture (Opta sand), at two flux rates, i.e., a lower flux rate of ~ 0.77 ml/min for ethanol and ~ 1.31 ml/min for water, and a higher flux rate of ~ 8.6 ml/min for ethanol

and ~ 14.5 ml/min for water. Tables 3.4, 3.5, and 3.6 list the conditions of the experiments.

#### *3.3.2.2 Homogenous Sand Pack*

The 2-D glass flow cell was packed using a continuous dry pour method. Sand of a known mass was poured evenly and continuously from a plastic container (0.59 m by 0.37 m by 0.15 m) into a custom-made funnel (0.59 m by 0.01 m) secured to the flow cell opening. Both outlet ports remained open to aid in air migration during the continuous sand pour and subsequent experimentation. As the sand was poured, the metal sides of the flow cell were continually agitated manually using a rubber mallet. The vibrations from the agitation generated higher bulk densities and a more uniform sand pack. The volume of sand poured into the flow cell was more than required to fill the flow cell to allow even sand pack right to the top of the flow cell. After the funnel was removed, the sand was made even and flush with the top of the flow cell using a plastic block. The remaining sand was collected and weighed to determine the mass of sand in the flow cell. The bulk density was calculated using the known mass of sand in the flow cell divided by the volume of the flow cell (Table 3.4, 3.5, 3.6). Visual inspection and bulk density were used as indicators of the relative homogeneity and reproducibility of sand pack. If visible heterogeneity was noted, the flow cell was emptied, and the sand was re-poured into the flow using the same method.

#### *3.3.2.3 Experimental Method*

After continuously pouring the sand and before beginning the experiment, the flow cell, rainulator, and camera were checked using beam and circular levels. Once ambient laboratory conditions were established, a known volume of 95% ethyl alcohol was applied to the surface of the flow cell at a constant rate using the constant flux apparatus setup (Phase 1; Section 3.3.1.2). Immediately after the ethanol was applied, the surface of the experiment was covered with plastic film to minimize any evaporative loss of moisture during the waiting period. The 24-hr waiting period began when the constant flux apparatus began applying ethanol (Phase 1). The waiting period allowed for migration and redistribution of fluids (specifically ethanol) within the flow cell. At the 24-hr mark, a known volume of deionized water was applied to the surface of the flow cell at a constant rate using the same constant flux apparatus setup (Phase 2). The surface of the experiment was again immediately covered with plastic film to minimize evaporation during the waiting period of Phase 2. In some experiments during Phase 2, during water infiltration, a stainless steel laboratory scoop was inserted as an impermeable barrier to prevent the infiltrating water from escaping the antecedent ethanol-contaminated area. There was a 24- to 72-hr waiting period that began after the initial application of deionized water (Phase 2 and Phase 3). This 24- to 72-hr waiting period provided sufficient time for drainage and redistribution to occur in the porous media. The application rates and volumes were verified before and after each application of ethanol and deionized water. The constant flux rate was maintained during the entire length of the application period. Fluid ponding was not observed during any of the

experiments. The ambient laboratory temperature was continually recorded in consideration of the fluid viscosity and density temperature dependence. The average laboratory temperature was 19.8°C ± 2°C. The results of the duplicate experiments confirmed the experimental findings.

#### *3.3.2.4 Image Acquisition*

Photographs using the camera setup (Section 3.3.1.3) were taken in 5-s increments during the first hour of each phase, followed by photographs at 15-min increments during the subsequent drainage and redistribution waiting periods. These photographs were used for visual flow observation and analyses and also were transformed into time-lapse videos for further analysis. Contact the author for access to the time-lapse videos.

## 3.4 Results and Discussion

### *3.4.1 Results*

To better understand the infiltration of water into ethanol-contaminated porous media, three categories of experiments were conducted by constant flux: Ethanol Following Water Infiltration Porous Media Experiments (Section 3.4.1.1), Water Following Ethanol Infiltration for Higher Volume and Lower Flux Continuous Experiments (Section 3.4.1.2), and Water Following Ethanol Infiltration for Lower Volume and Higher Flux Pulse Experiments (Section 3.4.1.3).

#### *3.4.1.1 Ethanol Following Water Infiltration into Porous Media Experiments*

Two base-case experiments of ethanol following water infiltration experiments into air-dried Opta sand were conducted as outlined in Table 3.4. The experimental details are provided in Table 3.4.

Table 3.4. Experimental details for the constant flux ethanol following water infiltration porous media experiments. The Opta Minerals Quartz Silica 49-7-15 is a coarser and lighter coloured sand, and the OOO Ricci Bros Co., Inc. Sand is a finer and darker coloured sand.

| Experiment Name | Sand Type | Bulk Density | Volume of 95% Ethanol Applied | Volume of Water Applied | Rate of 95% Ethanol Application | Rate of Water Application |
|---|---|---|---|---|---|---|
| | | $g/cm^3$ | ml | ml | ml/min | ml/min |
| CF-Q | Opta sand | 1.73 | 44.50 | 31.0 | 7.42 | 15.50 |
| CF-R | Opta sand | 1.7 | 44.94 | 95.12 | 7.00 | - |

The de-aired, deionized water infiltrated into the air-dried unsaturated sand in an irregular, elongated hemispherical shape. The downwards deionized water migration was significant, occurring approximately ¼ flow cell depth over the 30-min waiting period (Figure 3.3b) before ethanol infiltration. The subsequent 95% ethanol application created a smooth semicircular infiltration pattern and a distinguishable interface between the two fluids (ethanol and water; Figure 3.3c). The interface between the two fluids (ethanol and water) was smooth and readily distinguishable as indicative of a stable displacement of water by ethanol (Figure 3.3d, 3.3e). A zone of lower fluid content at the ethanol-water

boundary is present; this zone of lower saturation (halo effect) will be discussed further in Section 5.1. As hypothesized, there was no evidence of unstable perturbations of the front or focused flow instability behaviours during this set of experiments. This stable infiltration behaviour is consistent with ethanol having a lower density and higher viscosity than water as listed in Table 1.2. A duplicate experiment was conducted.

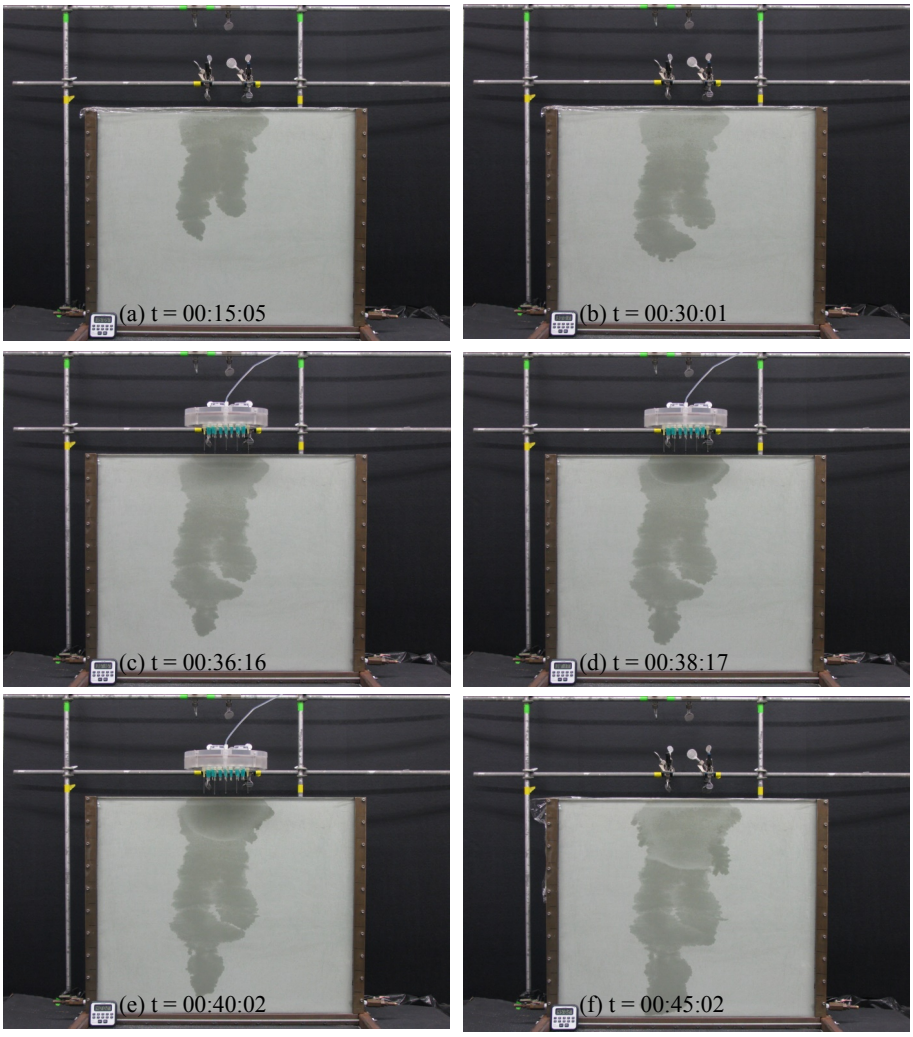


*Figure 3.3.* Ethanol following water infiltration constant flux experiment CF-R. Sequenced photographs of experiment CF-R with time zero being the beginning of water application at (a) t = 00:15:05, (b) t = 00:30:01, (c) t = 00:36:16 (start of ethanol infiltration), (d) t = 00:38:17, (e) t = 00:40:02, and (f) t = 00:45:02. Sequenced photographs of experiment CF-Q can be found in the Appendix.

#### *3.4.1.2 Continuous Application Experiments: Higher Volume and Lower Flux*

The long-term, lower flux, and higher volume continuous constant flux experiments performed are outlined in Table 3.5. There were five long-term and higher volume continuous experiments performed: three on the Ricci sand and two on the Opta sand. A

single focused flow event occurred in each of the higher volume and lower flux continuous constant head experiments performed (Figure 3.4). The experimental details are provided in Table 3.5.

Table 3.5. Experimental details for the higher volume and lower rate constant flux continuous water following ethanol infiltration porous media experiments. The Opta Minerals Quartz Silica 49-7-15 is a coarser and lighter coloured sand, and the OOO Ricci Bros Sand Co., Inc. is a finer and darker coloured sand.

| Experiment Name | Sand Type | Bulk Density | Volume of 95% Ethanol Applied | Volume of Water Applied | Rate of 95% Ethanol Application | Rate of Water Application |
|---|---|---|---|---|---|---|
| | | $g/cm^3$ | ml | ml | ml/min | ml/min |
| CF-B | Ricci sand | 1.63 | 45.07 | 124.77 | 0.75 | 1.39 |
| CF-D | Ricci sand | 1.63 | 47.44 | 136.00 | 0.79 | 1.13 |
| CF-E | Ricci sand | 1.64 | 45.30 | 148.20 | 0.76 | 1.24 |
| CF-H | Opta sand | 1.69 | 49.73 | 115.80 | 0.83 | 1.29 |
| CF-J | Opta Sand | 1.72 | 47.30 | 130.50 | 0.79 | 1.45 |

**Phase 1: Antecedent Ethanol Contamination**

During the application of water at the surface, the 95% ethanol infiltrated into the unsaturated porous media as a stable, smooth, elongated boundary, bulb-like shape (Figure 3.4a, 3.4b) during the infiltration of ~ 45 to 50 ml of ethanol over the application area (Table 3.5). In one instance (CF-J), the infiltrating ethanol reached the bottom of the flow cell after the 24-hr waiting period. Both sand types showed substantial downward migration and redistribution of the infiltrating ethanol over the course of the 24-hr waiting period (Phase 1; Figure 3.4c). During the other four experiments (CF-B, CF-D, CF-E, CF-

H), the infiltrating ethanol front reached about two-thirds of the depth of the flow cell after the 24-hr waiting period.

**Phase 2: Infiltrating Water-Bulb Formation**

During the subsequent application of water at the surface of the sand, three distinct growth stages occurred: the stable water-bulb, the focused flow, and the breakthrough (Figure 3.4). Each stage exhibited distinct visual characteristics. The water-bulb stage was the first to occur and began as the de-aired, deionized water was applied to the ethanol-contaminated porous media (Phase 2). The water-bulb of deionized water was an irregular, semi-hemispherical shape that continued to grow outwards as deionized water was applied to the surface. The application time of water was longer (Table 3.5) than the length of time the water-bulb remained at this stage.

In all instances, the focused flow began forming before the end of water application. The time between the start of water application and visualization of focused flow behaviours was approximately 5 to 10 mins in the Opta sand and 7 to 20 mins in the Ricci sand after application had stopped.

**Phase 2: Focused Flow Formation**

The water-bulb stage was followed by the focused flow stage, during which the preferential focused flow developed as an unstable perturbation at the base of the deionized water-bulb (the deepest zone of the water-bulb). Subsequently, the water draining from the water-bulb converged upon perturbation and advanced below the water-

bulb into a vertically oriented, narrowly focused preferential flow pathway (Figure 3.4d, 3.4e, 3.4f, 3.4g). The deionized water from within the water-bulb and the continued application from the peristaltic pump continued to feed the focused flow event. Drainage occurred within the water-bulb as the focused flow migrated through the system. The focused flow grew vertically at the tip and exhibited little horizontal growth. A zone of lower saturation at the ethanol-water boundary developed, which will be discussed in Section 5.1. This zone of lower saturation was more prominent in the Opta sand.

In all instances, a few minor perturbations formed at the base of the focused flow; however, eventually only one perturbation broke through and became the predominant preferential flow. The remaining perturbations did not continue to grow.

Experiments CF-D, CF-E, and CF-J showed evidence of bifurcation or multiple, initial unstable focused flow events. This phenomenon will be discussed further in Section 3.4.2.8. Additionally, all experiments showed one final, dominant focused flow event.

**Phase 3: Breakthrough Formation**

The breakthrough stage followed the focused flow stage. The breakthrough stage occurred when the focused flow reached the base of the antecedent ethanol-contaminated porous media and broke through into the uncontaminated, air-dry unsaturated porous media (Figure 3.4h). This is noteworthy in that over a relatively short period of time, the water migrated deeper into the sand and at a much higher rate than the ethanol migration

in the previous 24 hrs. That is, the water essentially bypassed much of the ethanol-contaminated zone. During the breakthrough stage, there was a visible and evident drainage front apparent in the upper section of the flow cell. The drainage front was seen in both the Ricci sand and the Opta sand but is more pronounced in the Opta sand.

During the higher volume and lower flux continuous experiments, the focused flow and breakthrough stages continued through the constant flux application and persisted after the constant flux application had ended. This indicates that the focused flow and breakthrough event was not due to the apparatus setup itself. The long-term nature of these experiments allowed for the various stages to fully develop. The longer duration of application in combination with the larger volume of water applied created a clearer, observable focused flow event and a more apparent breakthrough behaviour. Duplicate experiments were completed for each experiment and sand type.


*Figure 3.4.* Higher volume and lower flux continuous water following ethanol infiltration constant flux experiment CF-J. Sequenced photographs of experiment CF-J with time zero being the beginning of ethanol application (a) t = 00:30:05, (b) t = 00:59:50, (c) t = 24:15:12 (start of water application), (d) t = 24:30:13, (e) t = 24:45:13, (f) t = 25:00:14, (g) t = 25:15:14, and (h) t = 26:59:47. Sequenced photographs of experiments CF-B and CF-D can be found in the Appendix.

#### *3.4.1.3 Pulse Application Experiments: Lower Volume and Higher Flux*

The conditions of pulse experiments with short-term, lower volume, and higher constant flux are outlined in Table 3.6. There were four short-term and lower volume pulse experiments performed: two on the Ricci sand and two on the Opta sand. A single focused flow event occurred in each of the lower volume and higher flux pulse constant head experiments performed (Figure 3.5). The experimental details are provided in Table 3.6.

Table 3.6. Experimental details for the lower volume and higher constant flux pulse water following ethanol infiltration porous media experiments. The Opta Minerals Quartz Silica 49-7-15 is a coarser and lighter coloured sand, and the OOO Ricci Bros Sand Co. Inc. is a finer and darker coloured sand.

| Experiment Name | Sand Type | Bulk Density | Volume of 95% Ethanol Applied | Volume of Water Applied | Rate of 95% Ethanol Application | Rate of Water Application |
|---|---|---|---|---|---|---|
| | | $g/cm^3$ | ml | ml | ml/min | ml/min |
| CF-K | Opta sand | 1.69 | 29.61 | 29.61 | 8.71 | 14.71 |
| CF-M | Opta sand | 1.70 | 30.45 | 29.32 | 8.46 | 13.27 |
| CF-N | Ricci sand | 1.63 | 30.01 | 45.18 | 9.23 | 14.21 |
| CF-P | Ricci sand | 1.63 | 29.06 | 43.76 | 8.40 | 15.30 |

**Phase 1: Antecedent Ethanol Contamination**

The short-term and lower volume constant flux pulse experiments generated similar results to those of the long-term and higher volume continuous constant flux experiments (Section 3.4.1.2). The 95% ethanol infiltrated into the unsaturated porous media in a

stable, smooth, elongated bulb-like shape, redistributing to approximately two-thirds of the flow cell depth for the Ricci sand and approximately one-half the depth of the flow cell for the Opta sand (Figure 3.5a, 3.5b, 3.5c). Approximately 30 ml of ethanol was applied over the application area (Table 3.6). Both sand types showed substantial downwards migration and redistribution of the infiltrating ethanol over the course of the 24-hr waiting period (Phase 1; Figure 3.5c). The water-bulb in higher flux experiments forms faster than the water-bulb in the flow flux experiments described in Section 3.4.1.2.

**Phase 2: Infiltrating Water-Bulb Formation**

Similar to the long-term and higher volume continuous constant flux experiments, the behaviours that occurred during and after the application of water on the system can be divided into three distinct growth stages: the stable water-bulb, the focused flow, and the breakthrough (Figure 3.5d).

The water-bulb stage was the first to occur and began immediately as the de-aired, deionized water was applied to the ethanol-contaminated porous media (Phase 2). The water-bulb of deionized water was a semi-hemispherical shape that grew outwards as deionized water was applied to the surface. The water-bulb continued to migrate outwards even after the application via rainulator and peristaltic pump had stopped. The time between the end of water application and first visualization of focused flow behaviours was approximately 20 to 60 mins in the Opta sand and 1 to 3 hrs in the Ricci sand. The focused flow did not form until after application had stopped.

### Phase 2: Focused Flow Formation

The focused flow stage occurred when a preferential focused flow developed as an unstable perturbation at base of the water-bulb (the deepest zone of the water-bulb), i.e., at the infiltration front between antecedent ethanol and infiltrating water. Subsequently, the water draining from within the water-bulb converged and drained through a narrowly focused, vertically oriented preferential-flow pathway (Figure 3.5e, 3.5f). Drainage of the applied deionized water from within the water-bulb solely fed the focused flow since the application of water via peristaltic pump had previously stopped (pulse application). That is, there was a finite and specific volume of water present within the water-bulb. The focused flow grew vertically at the tip but exhibited little horizontal growth. The narrow zone of visibly observable lower saturation was associated with the ethanol-water boundary and will be discussed in Section 5.1. Similar to long-term and higher volume continuous constant flux experiments, this zone of lower saturation was more prominent in the Opta sand than in the Ricci sand. In all experiments, only one dominant perturbation was formed, which occurred at the base of the water-bulb (also the deepest part of the bulb). These constant flux experiments did show evidence of multiple perturbations forming (specifically CF-M) during the beginning of the focused flow stage; however, eventually one perturbation broke through and became the dominant preferential flow.

### Phase 3: Breakthrough Formation

The final stage is the breakthrough stage, during which the focused flow reached the base of the antecedent ethanol-contaminated porous media and broke through into the uncontaminated, air-dry porous media, essentially bypassing the ethanol-contaminated zone (Figure 3.5g, 3.5h). After breakthrough, the water infiltrated into the uncontaminated air-dry sand with a stable infiltration front in a semicircular, diverging pattern indicative of a wetting fluid. Similar to the continuous application constant flux experiments, the breakthrough infiltration front was seen in both the Ricci sand and the Opta sand and was more evident in the Opta sand.

Since the water-bulb, focused flow, and breakthrough stages were expressed during the short pulse application of water experiments, the development of the focused flow (SCIFF) was dependent on continuous application or on the flux-application apparatus itself. The short-term nature of these experiments still allowed for the full development of all three stages while applying a lower volume pulse of water to the system. Duplicate experiments were completed for each experiment and sand type.

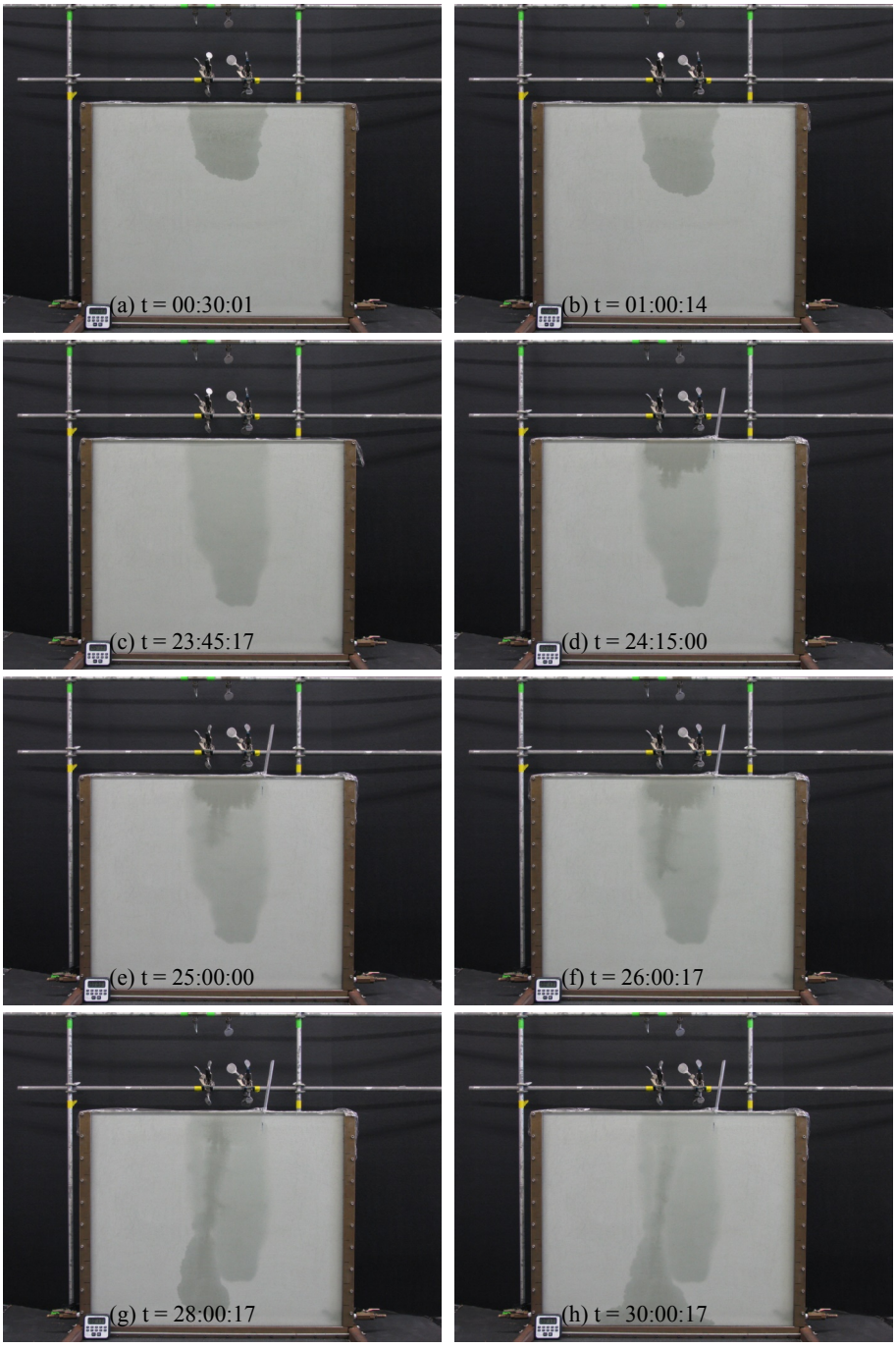


*Figure 3.5.* Lower volume and higher flux pulse water following ethanol infiltration constant flux experiment CF-M. Sequenced photographs of experiment CF-M with time zero being the beginning of ethanol application (a) t = 00:30:01, (b) t = 01:00:14, (c) t = 23:45:17, (d) t = 24:15:00 (start of water application), (e) t = 25:00:00, (f) t = 26:00:17, (g) t = 28:00:17, and (h) t = 30:00:17. Sequenced photographs of experiments CF-K and CF-N can be found in the Appendix.

### *3.4.2 Discussion*

#### *3.4.2.1 Comparison between Constant Flux Experiments*

Experiments where deionized, de-aired water infiltrated into antecedent ethanol-contaminated porous media exhibited vertical-flow events. Experiments where ethanol infiltrated into antecedent water did not exhibit focused flow events. These findings support the hypotheses of this thesis. Both the lower rate continuous constant flux and higher rate pulse constant flux experiments supported the hypothesis of this thesis. However, minor differences were identified.

**Continuous Application Experiments: Higher Volume and Lower Flux**

The lower flux continuous constant flux experiments are outlined and presented in Table 3.5 and Figure 3.4. The most notable difference was that the wetting front continued during the entire length of application. Therefore, hysteresis did not begin until the application had stopped. During these series of experiments, breakthrough at the base of the antecedent fluid occurred while application of water was continuing. Hysteresis began at the point where application stopped. The continuous application nature of the series of these experiments allowed for continuous finger growth. This application method produced higher rates of finger growth over time. This phenomenon will be discussed further in Section 3.4.2.5. Lastly, due to the nature of continuous application, the water-bulb of the infiltrating fluid is a smaller hemispherical shape than in the higher rate pulse flux experiments.

**Pulse Application Experiments: Lower Volume and Higher Flux**

The higher rate, pulse constant flux experiments are outlined and presented in Table 3.6 and on Figure 3.5. Again, the most notable difference was that the wetting front was present at the tip of the focused flow (had not penetrated the base of the antecedent contaminated porous media) and hysteresis had begun. During this series of experiments, the infiltrating fluid application stopped before the focused flow event began. Therefore, hysteresis was present as the focused flow event was forming. Specifically, the water near the sand surface underwent drainage while the lower water exhibited infiltration. This redistribution of a finite volume of water (pulse) was subject to the effects of hysteresis in the moisture characteristic (water content versus water pressure) curves. The pulse application nature of the series of experiments only allowed for targeted finger growth. This application method produced lower rates of finger growth over time. This phenomenon will be discussed further in Section 3.4.2.5. Lastly, due to the nature of the pulse application, the bulb of the infiltrating fluid is a larger hemispherical shape when compared to the infiltrating fluid bulb in the lower rate continuous flux experiments.

#### *3.4.2.2 Ethanol-Water Boundary Zone of Lower Saturation (Halo Effect)*

The zone of lower moisture content or saturation at the ethanol-water boundary surrounding the focused flow event (Figure 3.6) has been termed the halo effect. This narrow region of localized drainage is characteristic of the SCIFF effect (Smith et al., 2011). The phenomenon is present in all water following ethanol infiltration experiments

to some degree and is presented in CF-J (Figure 3.6). This zone of lower saturation is present in both sand types. However, it is more pronounced in the Opta sand due to the properties of the sand. This effect will be discussed in detail in Section 5.1.

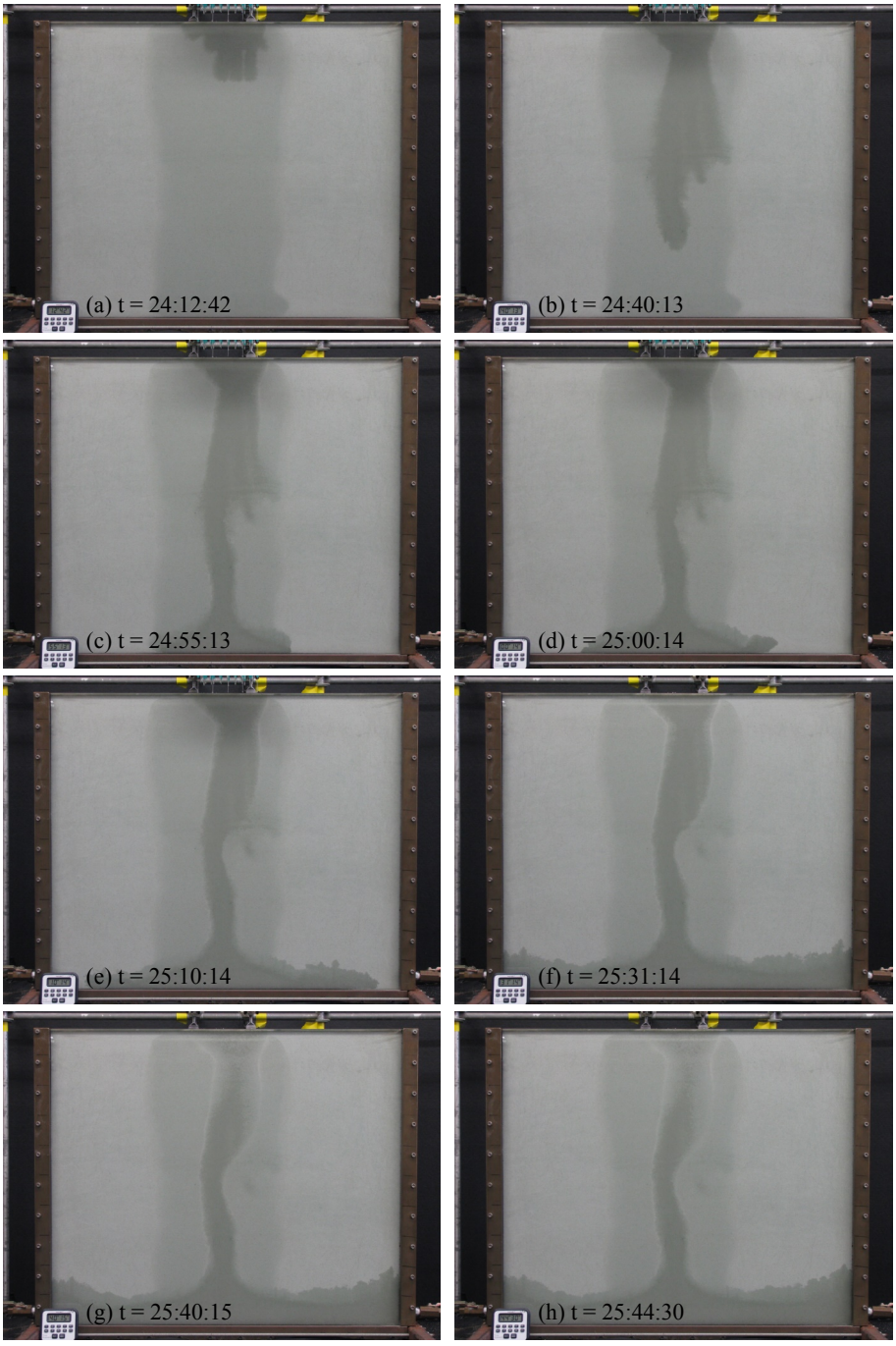


*Figure 3.6.* The ethanol-water boundary zone of lower saturation (halo effect) in experiment CF-J. The sequenced photographs begin with time zero being the beginning of ethanol application (a) t = 24:12:42, (b) t = 24:40:13, (c) t = 24:55:13, (d) t = 25:00:14, (e) t = 25:10:14, (f) t = 25:31:14 (application of water stopped at 25:30:00), (g) t = 25:40:15, and (h) t = 25:44:30.

#### *3.4.2.3 Cumulative Infiltration vs. Time*

Cumulative infiltration is the accumulated volume of infiltration into a porous media over a given period. During the constant flux application method, the rate of ethanol and water application are set and held at a constant rate; therefore, the cumulative infiltration versus time is linear with a constant slope expressing the set rate. Consequently, there is no difference between early-time cumulative infiltration and late-time cumulative infiltration plots. As can be seen in Table 3.7 and Table 3.8, water infiltrates visibly at a faster rate than ethanol as expressed by the distance of migration of the visible wetting front. This statement aligns with the physical properties of each fluid.

**Cumulative Ethanol Infiltration vs. Time**

The cumulative ethanol infiltration for the lower rate experiments for both the Opta sand and Ricci sand was lower than the cumulative infiltration for the higher rate experiments in the same sand types (Figure 3.7). The lower application rate resulted in lower cumulative infiltration rates (Figure 3.7; Table 3.7). The slope of the cumulative ethanol infiltration versus time indicates the rate at which the fluid was applied. There was minor variability in the overall cumulative infiltration rates; this can be seen in the slight variability between trend lines (Figure 3.7). The lower application rates increased the application time, whereas the higher application rates resulted in a shortened application time (Figure 3.7). The cumulative infiltration rate of ethanol infiltration into water-wet sands (indicated by black points) falls between the two infiltration rates but closer to the higher infiltration rate as that was the application method used for those experiments. The

lower flux experiments had targeted application volumes of approximately 45 ml, and the higher flux experiments had targeted application volumes of approximately 30 ml. The trend lines terminate at approximately those cumulative volumes (Figure 3.7).

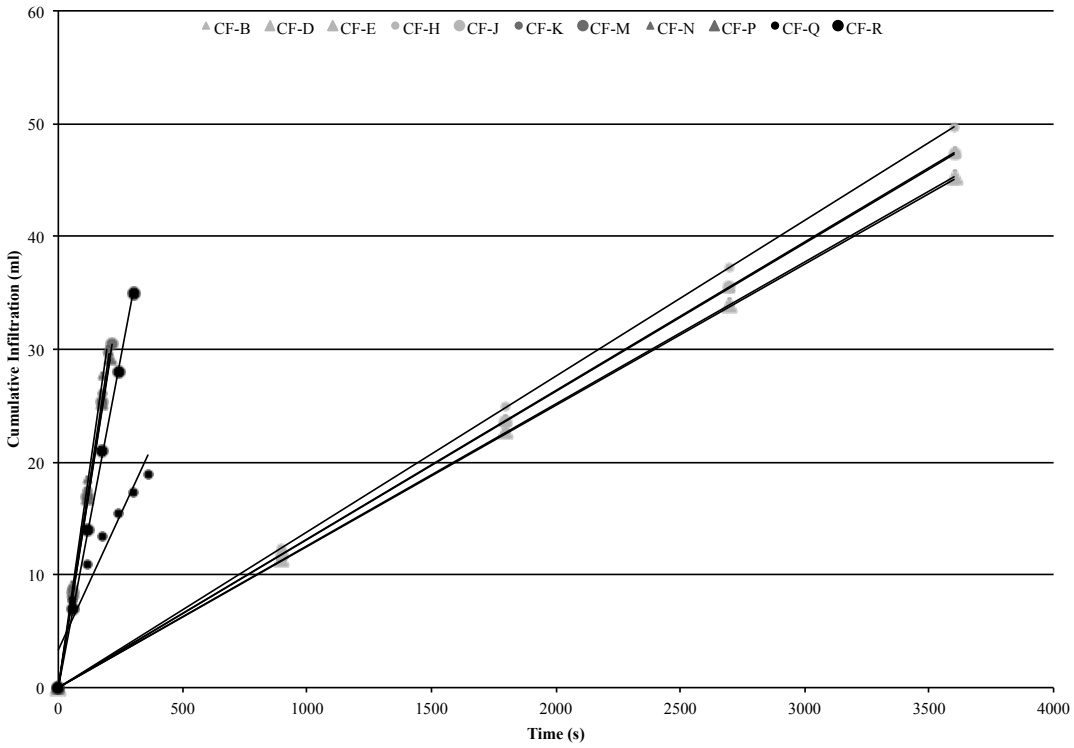


*Figure 3.7.* Cumulative ethanol infiltration vs. time for Opta Minerals Quartz Silica 49-7-15 and OOO Ricci Bros Sand Co., Inc. constant flux experiments. The symbologies are as follows: Higher Volume & Lower Flux Continuous Experiments on OOO Ricci Bros. Co., Inc. ▲, Higher Volume & Lower Flux Continuous Experiments on Opta Minerals Silica Quartz 49-7-15 •, Lower Volume & Higher Flux Pulse Experiments on OOO Ricci Bros. Co., Inc. ▲, Lower Volume & Higher Flux Pulse Experiments Opta Minerals Silica Quartz 49-7-15 •, and Ethanol following Water Infiltration (Lower Volume & Higher Flux Pulse Experiments on Opta Minerals Silica Quartz 49-7-15) •.

Table 3.7. Average ethanol cumulative infiltration rates for Opta Minerals Quartz Silica 49-7-15 and OOO Ricci Bros Sand Co., Inc. constant flux experiments.

| Sand Type | Experiment Type | Average Cumulative Infiltration Rate |
|---|---|---|
| | | ml/s |
| Opta sand | Continuous Application | 0.013 |
| | Pulse Application | 0.144 |
| Ricci sand | Continuous Application | 0.013 |
| | Pulse Application | 0.144 |

**Cumulative Water Infiltration vs. Time**

The cumulative water infiltration for the lower rate experiments for both the Opta sand and Ricci sand is lower than the cumulative infiltration for the higher rate experiments in the same sand types (Figure 3.8; Table 3.8). The rate of application is proportional to (the slope of) the cumulative infiltration versus time plot. The lower application rates increased the application time, whereas the higher application rates resulted in a shortened application time (Figure 3.8). There is larger variability in cumulative infiltration rates for the lower rate application experiments; this can be seen in the variability of the trend lines (Figure 3.8). There is little variability in the cumulative infiltration rates for the higher rate application experiments. The cumulative infiltration rate of water into unsaturated sands (indicated by black points) aligns with the higher application cumulative infiltration rate experiments as that was the application method chosen (Figure 3.8). The lower flux experiments had targeted application volumes of approximately 100 to 150 ml, and the

higher flux experiments had targeted application volumes of approximately 50 ml. The trend lines terminate at approximately those cumulative volumes (Figure 3.8).

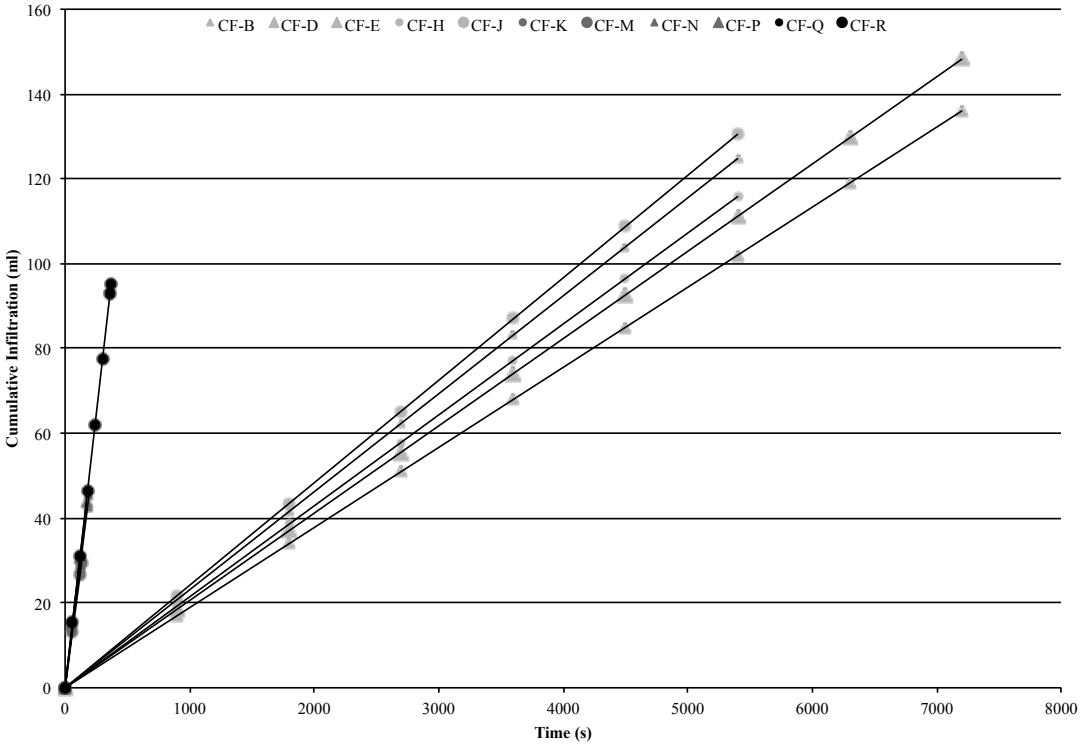


*Figure 3.8.* Cumulative water infiltration vs. time for Opta Minerals Quartz Silica 49-7-15 and OOO Ricci Bros Sand Co., Inc. constant flux experiments. The symbologies are as follows: Higher Volume & Lower Flux Continuous Experiments on OOO Ricci Bros. Co., Inc. ▲, Higher Volume & Lower Flux Continuous Experiments on Opta Minerals Silica Quartz 49-7-15 •, Lower Volume & Higher Flux Pulse Experiments on OOO Ricci Bros. Co., Inc. ▲, Lower Volume & Higher Flux Pulse Experiments Opta Minerals Silica Quartz 49-7-15 •, and Ethanol following Water Infiltration (Lower Volume & Higher Flux Pulse Experiments on Opta Minerals Silica Quartz 49-7-15) •.

Table 3.8. Average water cumulative infiltration rates for Opta Minerals Quartz Silica 49-7-15 and OOO Ricci Bros Sand Co., Inc. constant flux experiments.

| Sand Type | Experiment Type | Average Cumulative Infiltration Rate |
|---|---|---|
| | | ml/s |
| Opta sand | Continuous Application | 0.023 |
| | Pulse Application | 0.229 |
| Ricci sand | Continuous Application | 0.021 |
| | Pulse Application | 0.246 |

#### *3.4.2.4 Cumulative Infiltration vs. Root Time*

Cumulative infiltration for root time is common practice and provides a different perspective and additional support of the relationships described in Section 3.4.2.3.

**Cumulative Ethanol Infiltration vs. Root Time**

Similarly to cumulative infiltration versus time, against root time, the cumulative ethanol infiltration applied under lower constant flux is lower than the cumulative infiltration applied under higher constant flux for both the Opta sand and the Ricci sand (Figure 3.9). Furthermore, the cumulative infiltration rate of lower flux ethanol infiltration into water-wet sands (indicated by black points) falls in the same range as the lower flux experiments (Figure 3.9). Both the lower flux and higher flux have variability in the trend lines. However, the lower flux experiments see greater variability. All trend lines see a convex relationship that tends to increase upwards (Figure 3.9). The lower flux and higher

flux curves terminate at approximately 45 ml and 30 ml, respectively, as those were the targeted volumes for those series of experiments (Figure 3.9).

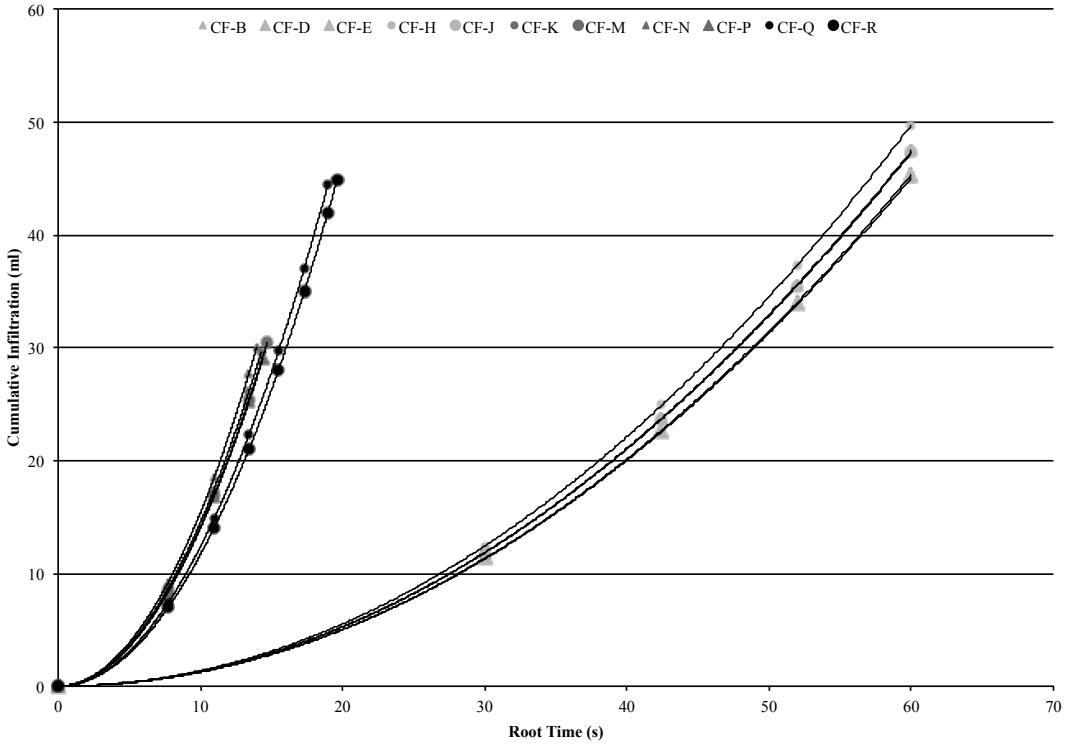


*Figure 3.9.* Cumulative ethanol infiltration vs. root time for Opta Minerals Quartz Silica 49-7-15 and OOO Ricci Bros Sand Co., Inc. constant flux experiments. The symbologies are as follows: Higher Volume & Lower Flux Continuous Experiments on OOO Ricci Bros. Co., Inc. ▲, Higher Volume & Lower Flux Continuous Experiments on Opta Minerals Silica Quartz 49-7-15 •, Lower Volume & Higher Flux Pulse Experiments on OOO Ricci Bros. Co., Inc. ▲, Lower Volume & Higher Flux Pulse Experiments Opta Minerals Silica Quartz 49-7-15 •, and Ethanol Following Water Infiltration (Lower Volume & Higher Flux Pulse Experiments on Opta Minerals Silica Quartz 49-7-15) •.

### Cumulative Water Infiltration vs. Root Time

Similarly to cumulative infiltration versus time, against root time, the cumulative water infiltration applied under lower flux is lower than the cumulative water infiltration under higher flux for both sands (Figure 3.10). There is a much larger variability in the lower flux cumulative water infiltration trend lines compared to the higher flux cumulative

infiltration trend lines (Figure 3.10). Furthermore, the cumulative infiltration rate of lower flux ethanol infiltration into water-saturated sands falls in the same range as the lower flux experiments (Figure 3.10). All trend lines see a convex relationship that tends to increase upwards. The lower flux and higher flux curves terminate at approximately 150 ml and 50 ml, respectively, as those were the targeted volumes for those series of experiments.

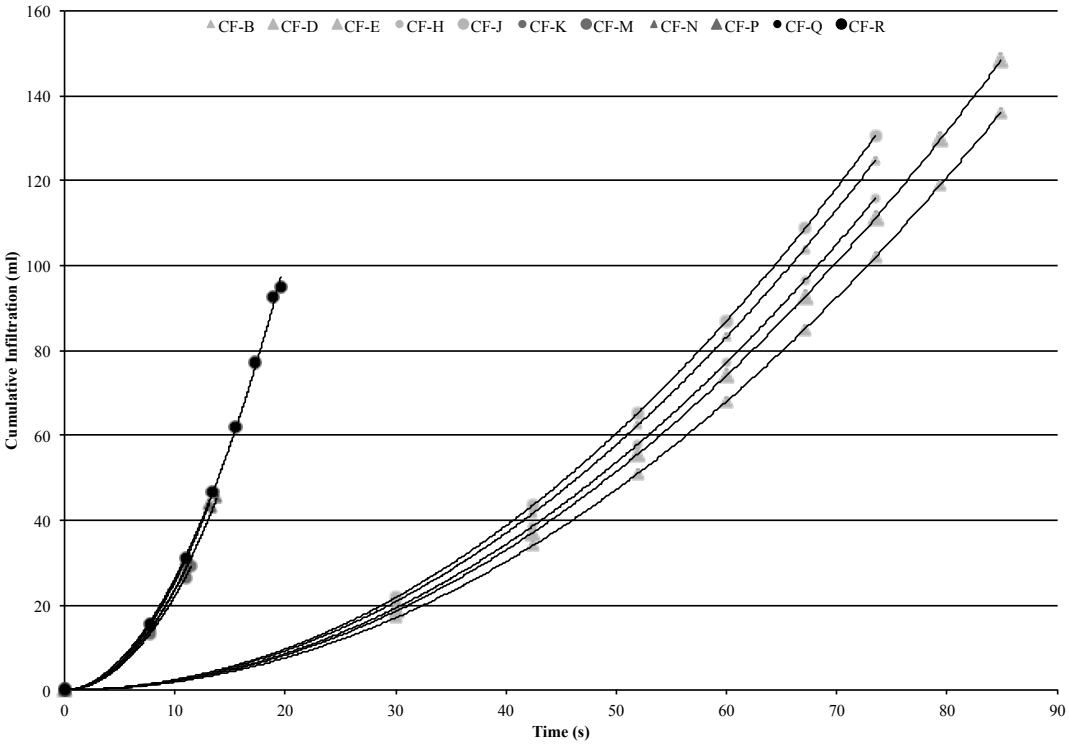


*Figure 3.10.* Cumulative water infiltration vs. root time for Opta Minerals Quartz Silica 49-7-15 and OOO Ricci Bros Sand Co., Inc. constant flux experiments. The symbologies are as follows: Higher Volume & Lower Flux Continuous Experiments on OOO Ricci Bros. Co., Inc. ▲, Higher Volume & Lower Flux Continuous Experiments on Opta Minerals Silica Quartz 49-7-15 •, Lower Volume & Higher Flux Pulse Experiments on OOO Ricci Bros. Co., Inc. ▲, Lower Volume & Higher Flux Pulse Experiments Opta Minerals Silica Quartz 49-7-15 •, and Ethanol Following Water Infiltration (Lower Volume & Higher Flux Pulse Experiments on Opta Minerals Silica Quartz 49-7-15) •.

#### *3.4.2.5 Finger Length vs. Time*

A finger is a type of preferential flow caused by instability due to pore-scale variations and fluid properties (Fetter, 1999). Finger length can provide many insights into focused flow. Finger length was measured manually from the base of the bulb to the finger tip for each type of experiment and plotted against time (Figure 3.11). The work by Zhang and Smith (2001, 2002) showed that experiments with the same trend-line slope have the same velocity. For both types of experiments, finger growth rate is constant (Figure 3.11).

**Pulse Application Experiments: Lower Volume and Higher Flux**

All duplicate experiments have comparable slope values, thereby similar finger growth velocities (Figure 3.11). The single exception to this is experiment CF-K (higher flux pulse experiment in the Opta sand) as an arm formed during the experiment and is therefore not representative. At the same higher flux rate, the Opta sand had finger growth rates of ~ 0.25 cm/min (not including experiment CF-K, the rate is 0.11 cm/min), whereas the Ricci sand had finger growth rates of ~ 0.10 cm/min (Figure 3.11). The finger growth rates were similar due to the constant application rate, despite differing sand characteristics.

**Continuous Application Experiments: Higher Volume and Lower Flux**

At lower flux, the Opta sand had finger growth rates of ~ 1.17 cm/min, whereas the Ricci sand had finger growth rates of ~ 0.61 cm/min (Figure 3.11). As anticipated, a higher finger growth rate was seen in Opta sand when compared to the Ricci sand.

Intuitively, higher flux application experiments would have higher rates of finger length growth and vice versa. As seen on Figure 3.11, lower flux rates display higher rates of finger growth. This could be due to lower flux application rates having smaller finger width, therefore having higher finger growth rates. The inverse would indicate that higher flux application rates would have larger finger widths, therefore lower finger length growth rates. However, there were no notable or observable differences between flux applications regarding finger width.

Overall, all lower flux continuous experiments had a higher rate of finger growth than higher flux experiments. This was primarily due to the experimental method as in the lower flux experiments water was continually added using a peristaltic pump. This continuous application created a continuously fed conduit through the unsaturated zone.

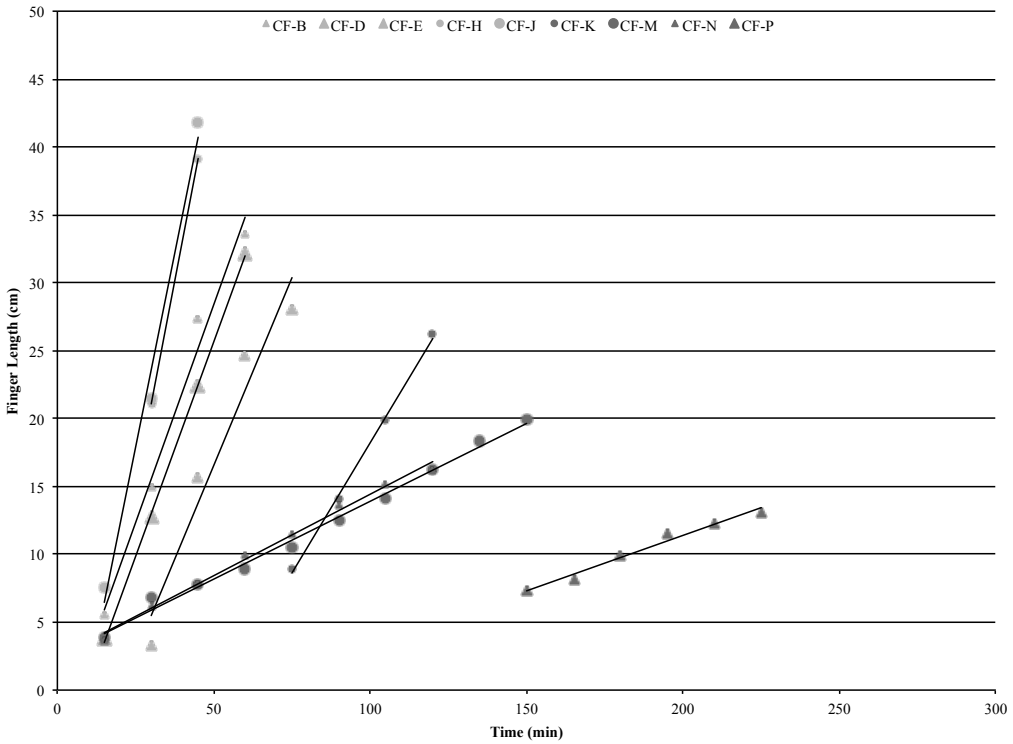


*Figure 3.11.* Finger length vs. time for Opta Minerals Quartz Silica 49-7-15 and OOO Ricci Bros Sand Co., Inc. constant flux experiments with time zero beginning at the start of water application. The symbologies are as follows: Higher Volume & Lower Flux Continuous Experiments on OOO Ricci Bros. Co., Inc. ▲, Higher Volume & Lower Flux Continuous Experiments on Opta Minerals Silica Quartz 49-7-15 •, Lower Volume & Higher Flux Pulse Experiments on OOO Ricci Bros. Co., Inc. ▲, and Lower Volume & Higher Flux Pulse Experiments Opta Minerals Silica Quartz 49-7-15 •.

#### *3.4.2.6 Moisture Content*

Moisture content and changes in moisture content are expressed well through images collected during the experiments. The areas of higher moisture content were defined with darker coloured sand, whereas air-dry sand or low moisture content was defined by lighter coloured sand. The highest moisture content was at the centre of the narrowly focused flow. During the drainage events, the decreases in liquid content were expressed as changing from darker, higher liquid moisture content sand to a lighter, lower liquid

moisture content sand. A zone of lower liquid (moisture) content visible at the ethanol-water boundary was the manifestation of the halo effect discussed in Section 5.1.

#### *3.4.2.7 Heterogeneities*

The relatively small heterogeneity in the system still provides valuable insight into understanding focused flow behaviours, while still adding complexities to the system that can inhibit systematic discussion of mechanism and processes within this research. The heterogeneities in the porous media were a consequence of the flow cell packing method (Section 3.3.2.2) and were not specifically a target of the research.

Varying degrees of heterogeneity are noted in all constant flux experiments. Experiments with the most prominent heterogeneous effects are CF-D (Figure 3.12), CF-E, and CF-J; however, minor heterogeneity is present in all experiments due to the experimental method and packing procedure. Even with heterogeneities present in the system, the focused flow event overcame the effects of minor heterogeneity.

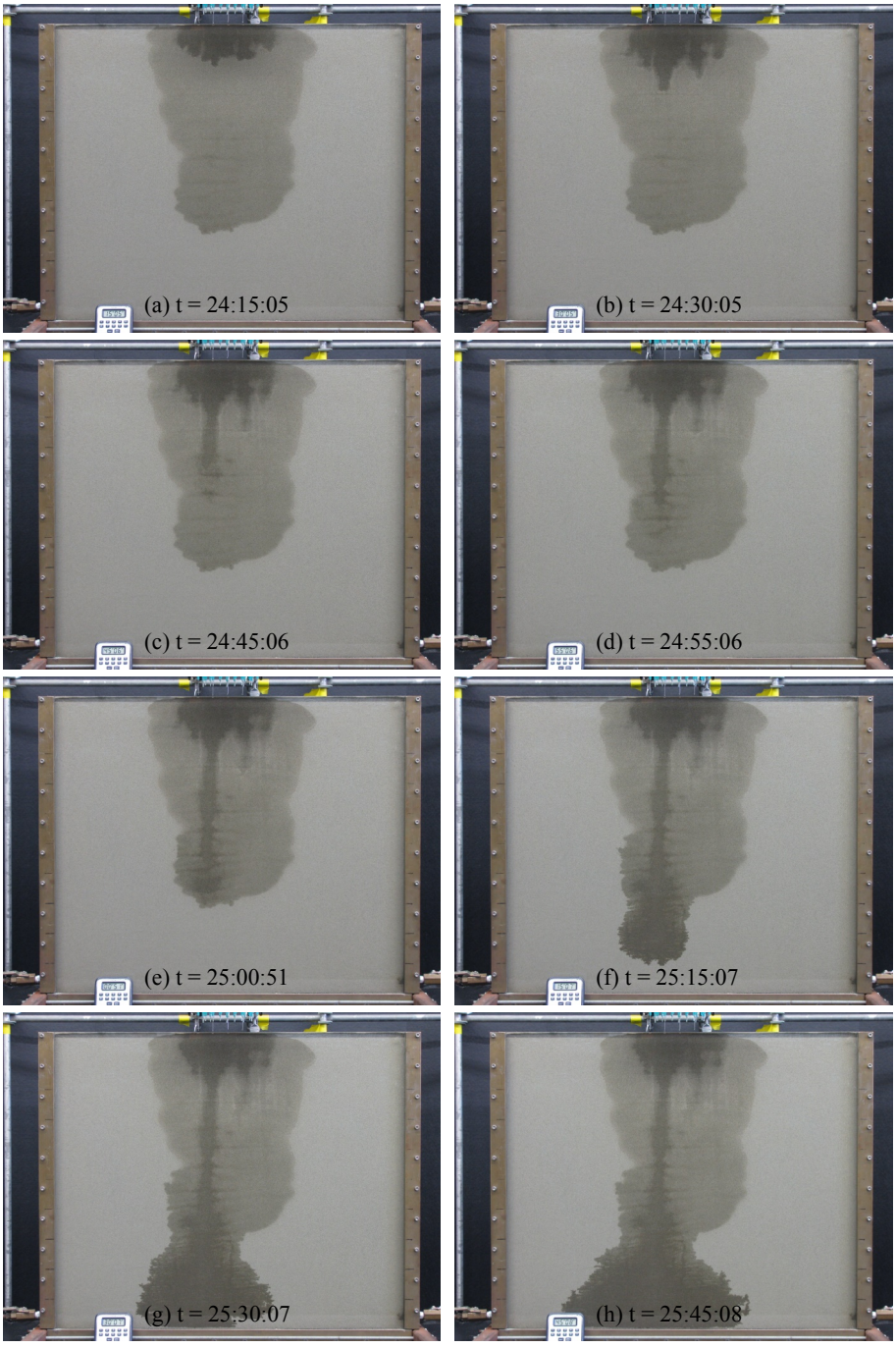


*Figure 3.12.* Water following ethanol infiltration constant flux experiment CF-D exhibiting minor heterogeneity. Sequenced photographs of experiment CF-D with time zero being the beginning of ethanol application (a) t = 24:15:05 (start of water application), (b) t = 24:30:05, (c) t = 24:45:06, (d) t = 24:55:06, (e) t = 25:00:51, (f) t = 25:15:07, (g) t = 25:30:07, and (h) t = 25:45:08.

#### *3.4.2.8 Bifurcation*

Bifurcation is the process whereby a focused flow event splits into two distinct focused flow fingers initiated by minor heterogeneities in the hydraulic properties at the tip of the advancing finger (Figure 3.13). In experiments where bifurcation occurs, the finger length growth rate is considerably smaller than that in a singular focused flow experiment and consistent with the supply of liquid being split between two pathways. Flow instability causing the generation of fingers during the displacement of a denser fluid displacing a less dense fluid in porous media requires initial perturbation of the infiltrating front. Small-scale heterogeneities in the pore structure can provide such perturbations (Chuoke et al., 1959).

Bifurcation was specifically noted in constant flux experiment CF-J (Figure 3.4) and CF-M (Figure 3.13). During experiment CF-M, two initial unstable fingers began to form; these fingers merged into one focused flow during migration through the ethanol-contaminated media. Bifurcation of this finger occurred midway through the contaminated sand (Figure 3.13f, 3.13g). Rather than advancing, this bifurcated pathway subsequently drained into the primary focused flow (Figure 3.13h).

Although experiments CF-D and CF-E (Figure 3.14) resemble bifurcation, true bifurcation did not occur. The constant flux application of infiltrating water (Phase 2) was not applied evenly, resulting in two initial unstable displacements. Multiple displacements advanced, and consequently drained and supplied the primary focused flow event.

Constant flux experiment CF-P exhibited evidence of multiple finger formation (Figure 3.15); however, similarly to the bifurcation seen on Figure 3.13, one finger became the dominant focused flow event. Constant flux experiments CF-H and CF-K displayed arm formation (water escaping into the unsaturated zone; Figure 3.16). However, this formation was a consequence of the experimental method and had minor impacts to the focused flow event.

Finger growth over time for experiments that displayed bifurcation or multiple initial unstable displaces is presented on Figure 3.17. Experiment CF-D and CF-E showed similar visual initial unstable displacements, which is supported by similar graphical finger length growth over time (Figure 3.17). Based on graphical interpretation, the minor bifurcation noted in experiment CF-J did not have notable impacts on the rate of finger growth (Figure 3.17).

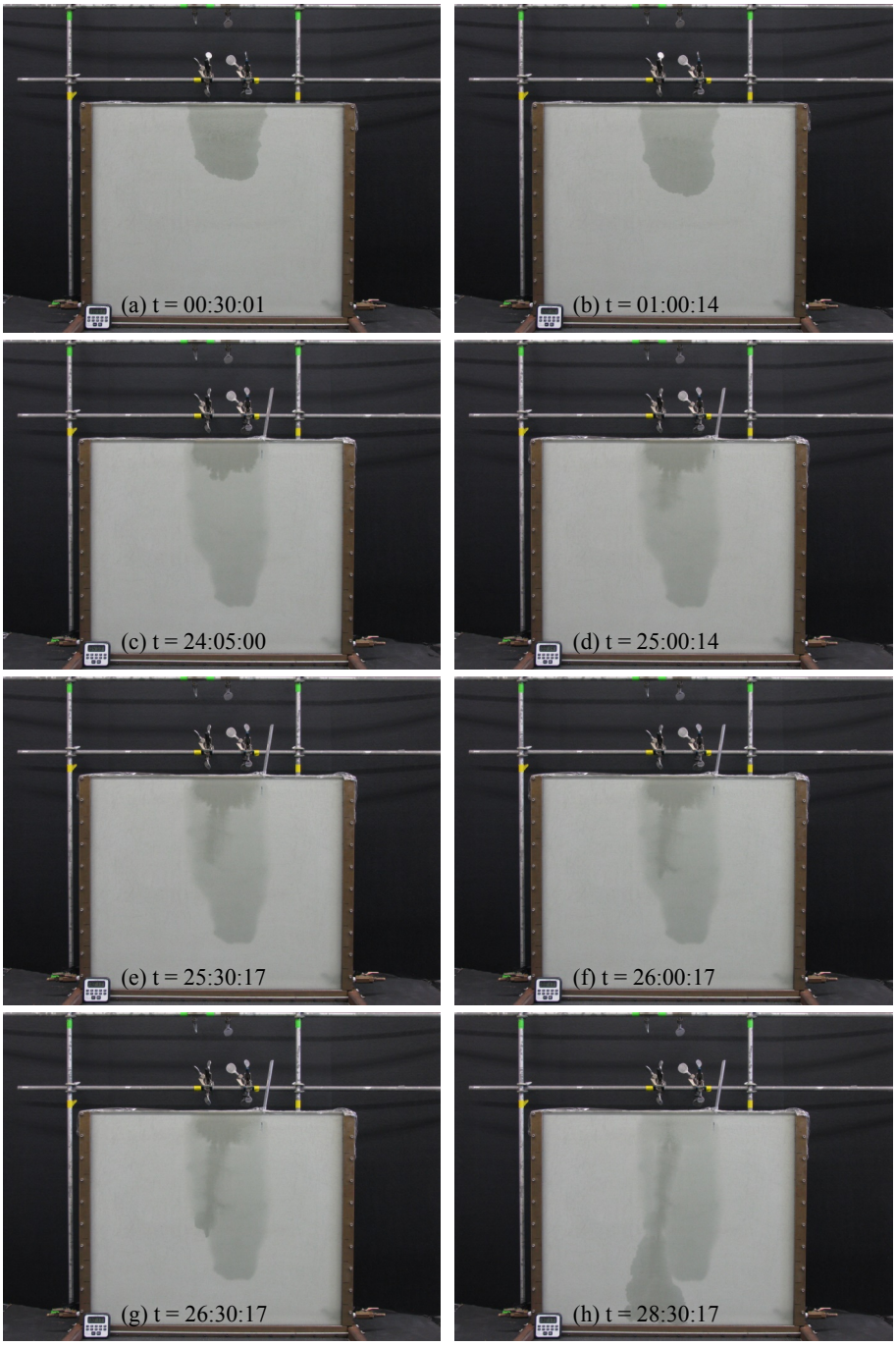


*Figure 3.13.* Water following ethanol infiltration constant flux experiment CF-M exhibiting bifurcation. Sequenced photographs of experiment CF-M with time zero being the beginning of ethanol application (a) t = 00:30:01, (b) t = 01:00:14, (c) t = 24:05:00 (start of water application), (d) t = 25:00:14, (e) t = 25:30:17, (f) t = 26:00:17, (g) t = 26:30:17, and (h) t = 28:30:17.

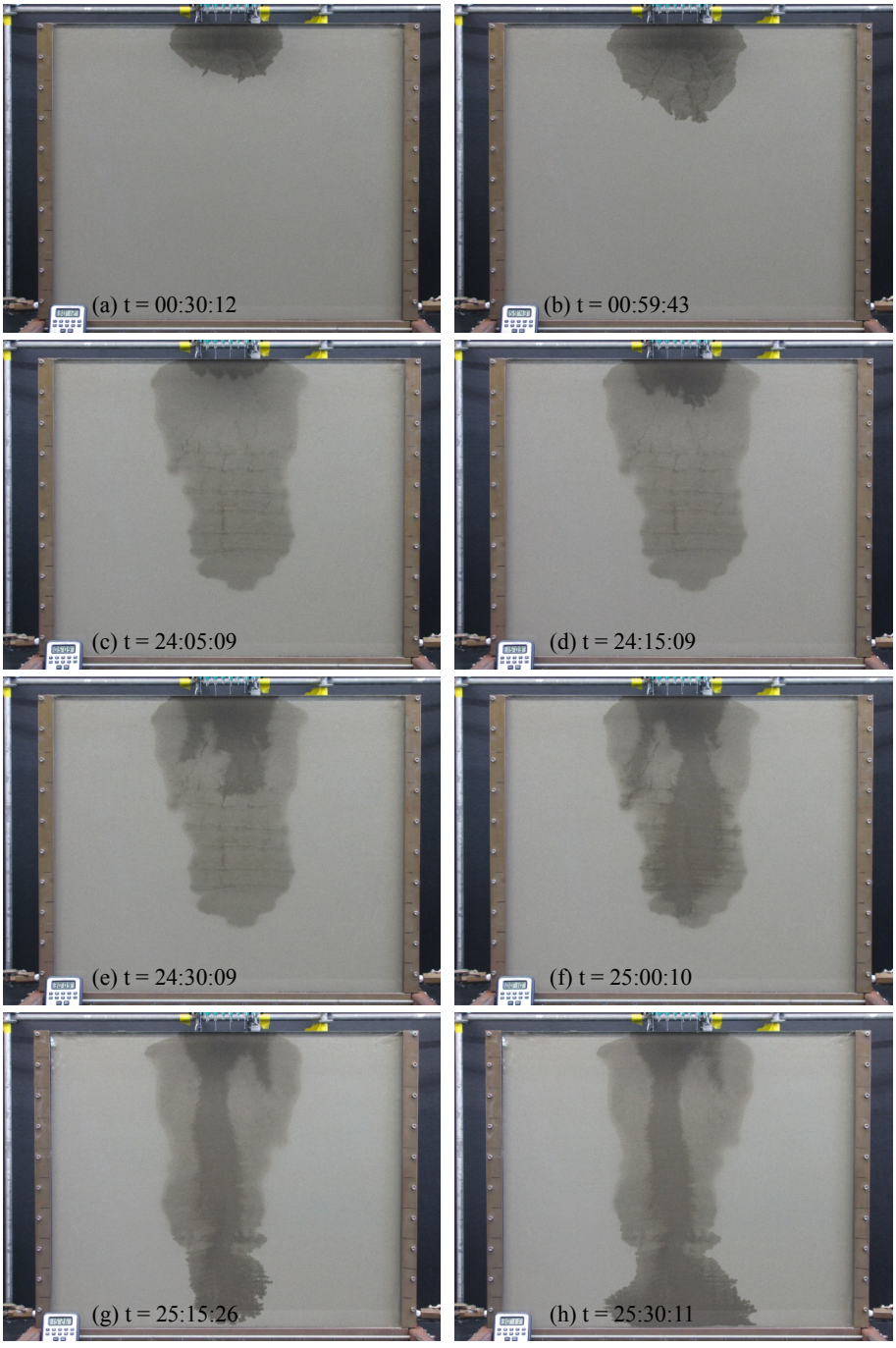


*Figure 3.14.* Water following ethanol infiltration constant flux experiment CF-E exhibiting two unstable displacements resulting in two focused flow events. Sequenced photographs of experiment CF-E with time zero being the beginning of ethanol application (a) t = 00:30:12, (b) t = 00:59:43, (c) t = 24:05:09 (start of water application), (d) t = 24:15:09, (e) t = 24:30:09, (f) t = 25:00:10, (g) t = 25:15:26, and (h) t = 25:30:11.

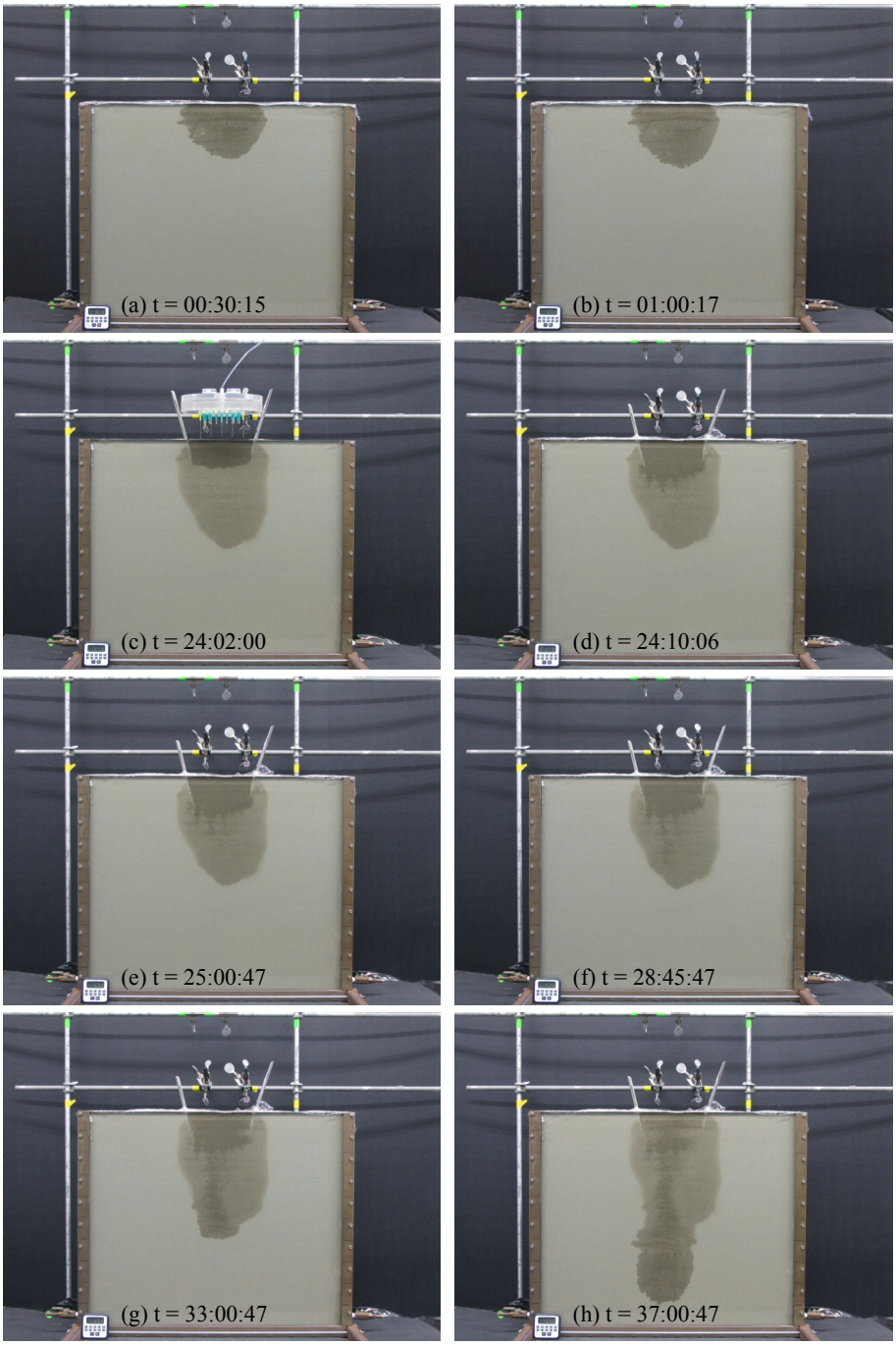


*Figure 3.15.* Water following ethanol infiltration constant flux experiment CF-P exhibiting minor finger formation. Sequenced photographs of experiment CF-P with time zero being the beginning of ethanol application (a) t = 00:30:15, (b) t = 01:00:17, (c) t = 24:02:00 (start of water application), (d) t = 24:10:06, (e) t = 25:00:47, (f) t = 28:45:47, (g) t = 33:00:47, and (h) t = 37:00:47.

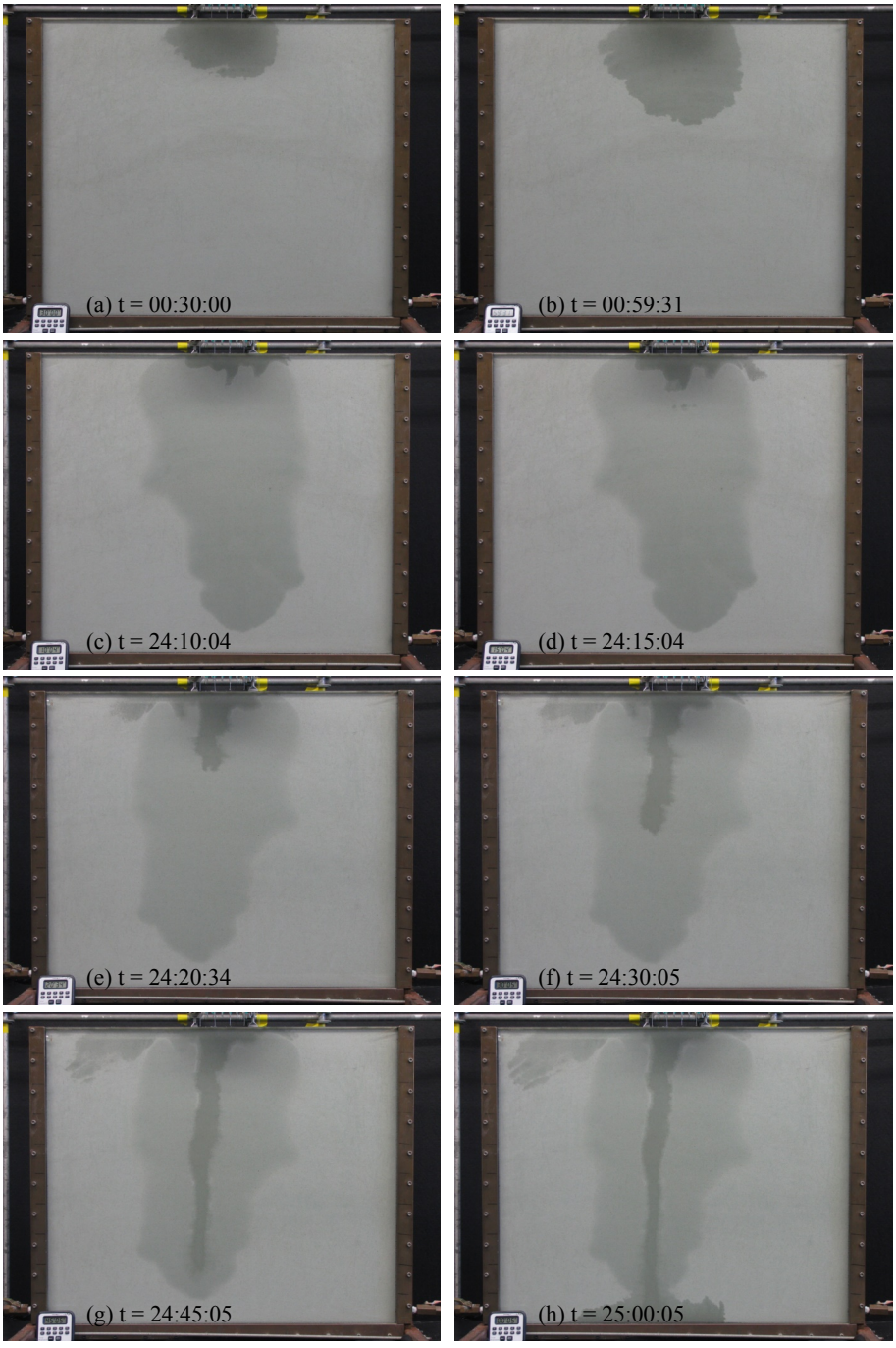


*Figure 3.16.* Water following ethanol infiltration constant flux experiment CF-H exhibiting arm formation. Sequenced photographs of experiment CF-H with time zero being the beginning of ethanol application (a) t = 00:30:00, (b) t = 00:59:31, (c) t = 24:10:04 (start of water application), (d) t = 24:15:04, (e) t = 24:20:34, (f) t = 24:30:05, (g) t = 24:45:05, and (h) t = 25:00:05.

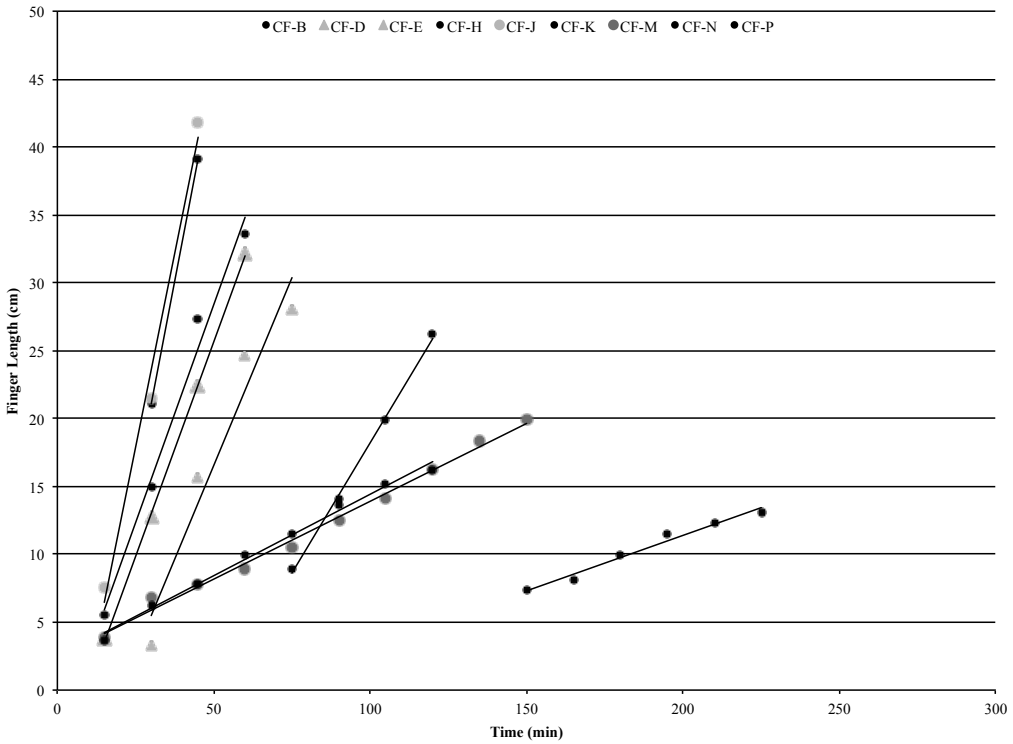


*Figure 3.17.* Comparison of finger length vs. time between singular focused flow experiments, multiple initial unstable displacements experiments (CF-D & CF-E), and bifurcated experiments (CF-J & CF-M). Time zero is the start of water application. The symbologies are as follows: Higher Volume & Lower Flux Continuous Experiments on OOO Ricci Bros. Co., Inc. ▲, Higher Volume & Lower Flux Continuous Experiments on Opta Minerals Silica Quartz 49-7-15 •, Lower Volume & Higher Flux Pulse Experiments Opta Minerals Silica Quartz 49-7-15 •, and singular focused flow experiments •.

#### *3.4.2.9 Effects of the Application Method*

The method of application can play a critical role in the experimental outcome. However, there was no evidence that either the peristaltic pump or the rainulator setup impacted the experimental outcome.

### 3.5 Conclusions

Water infiltrating into ethanol-contaminated porous media by application method of constant flux exhibits focused flow. There was no evidence of focused flow behaviours in ethanol following water infiltration porous media experiments by constant flux application. The presence of the antecedent ethanol creates a condition where the liquid pressure heads—due to capillarity—will be functionally dependent upon on both the volumetric moisture content and the aqueous ethanol concentration of the liquid (water) through its functional relation with interfacial (surface) tension at the air-liquid interfaces. This functional relation between ethanol content and liquid (water) pressure heads is the primary driver behind SCIFF. Additionally, the highly non-linear relation between kinematic viscosity and ethanol concentration, with its maximum around 40% by volume ethanol (the sludge effect), further contributes to sharpening the solute front between ethanol and water; this enhances the zone of lower saturation surrounding the focused flow event (the halo effect).

## 4 Constant Head

### 4.1 Introduction

Hydraulic head, or total head, is defined as the work per unit weight of fluid or energy state for groundwater relative to a datum (Bashir et al., 2007). Constant head means that a specific value of hydraulic head is maintained over time along the application surface. Positive values of constant pressure head mimic ponding behaviours on sands (Sciortino & Leij, 2012).

### *4.1.1 Tension Infiltrometry*

A tension infiltrometer (Figure 4.1) is a widely used laboratory and field measurement device that allows a given volume of water to pass through the porous stainless steel disc onto porous media under a calibrated and maintained tension (Reynolds & Zebchuk, 1996). Both the bubbling chamber and fluid reservoir are filled with fluid (Figure 4.1): the bubbling chamber with deionized water and the fluid reservoir with the infiltrating fluid. The suction or tension at the surface of the disc is controlled by the bubble tower, and the infiltrating fluid moves through the stainless steel disc at the base of the instrument (Figure 4.1). Tension infiltrometers maintain a negative pressure head or positive tension on the surface of the system (Beatty & Smith, 2013).

Tension infiltrometers can be used for measuring a variety of variables, some of which include hydraulic properties (i.e., hydraulic conductivity, cumulative infiltration), soil properties (i.e., pore size, sand texture), solute transport variables (i.e., solute transfer rate coefficients), and quantifying soil repellency (Beatty & Smith, 2013; Reynolds & Zebchuk, 1996).

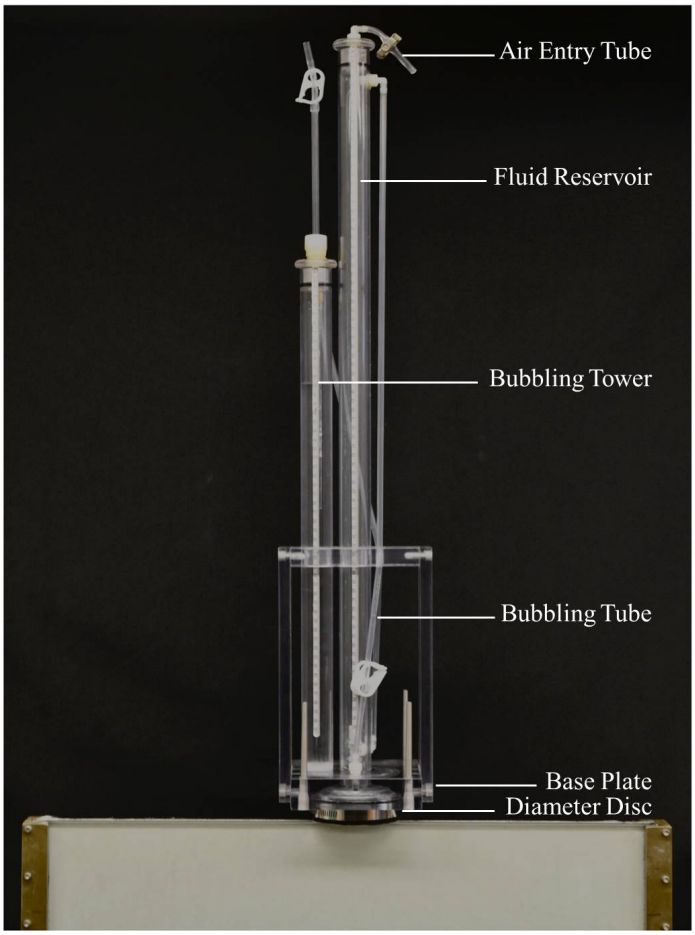


*Figure 4.1.* A labelled image of the constant head 8 cm tension infiltrometer positioned on the flow cell.

Section 3.1 contains a list of experimental design and analysis assumptions.

## 4.2 Study Objectives and Hypothesis

### *4.2.1 Study Objectives*

The primary objective of this research was to conduct a series of highly controlled 2-D unsaturated flow experiments using constant head application to the surface to

demonstrate, characterize, and quantify focused flow behaviour of water infiltrating into ethanol-contaminated porous media.

#### *4.2.2 Hypothesis*

The primary hypothesis of this research was that the application of water using constant head on ethanol-contaminated unsaturated porous media would produce a narrowly focused vertical flow infiltration pattern. It was further hypothesized that behaviour would be primarily due to the decreases in interfacial tensions between the air-liquid interfaces in the unsaturated sands as a function of ethanol concentration.

A secondary hypothesis was that the application of ethanol by constant head onto water-wetted unsaturated porous media would produce a stable semicircular infiltration pattern below the application area.

## 4.3 Experimental Design and Methods

### *4.3.1 Apparatus*

#### *4.3.1.1 Flow Cell*

The details regarding the flow cell are described in Section 3.3.1.1.

#### *4.3.1.2 Tension Infiltrometer*

An 8 cm Soil Measurement Systems Tension Infiltrometer was used for the constant head application experiments (Figure 4.1). The tension infiltrometer was used to apply ethanol

and water to 13.3% of the total width of the flow cell. The Plexiglas (acrylic) tension infiltrometer fluid reservoir was modified with a polypropylene fluid reservoir to accommodate 95% ethyl alcohol since acrylic is not compatible with high concentrations of ethanol. The tension infiltrometer was calibrated and used as per manufacturer instructions. The infiltrometer was thoroughly rinsed with deionized water after each phase of the experiment. The instrument was primed by initiating a bubble at the bottom of the bubbling tube (Figure 4.1) before each phase of the experiment.

Contact material is sediment applied in a thin layer to an experimental sediment surface. Contact material is used to level the surface and provide good contact between the instrument and sediment; contact material is primarily used in field experimental settings (Beatty & Smith, 2013; Reynolds & Zebchuk, 1996). The contact material should have a K greater than the K of the experimental sediment. Contact materials can have substantial impacts and discrepancy in experimental results (Beatty & Smith, 2013; Reynolds & Zebchuk, 1996). Consequently, a contact material was not used or required in this research.

The tension infiltrometer was not secured to a rigid support frame structure but was manually held to ensure and maintain good hydraulic contact over the duration of the experiment. The hydraulic contact between the infiltrometer and sand was checked regularly before, during, and after each application of fluid by the apparatus.

#### *4.3.1.3 Camera*

The details regarding the flow cell are described in Section 3.3.1.3.

#### *4.3.1.4 Materials*

The details regarding the materials used are described in Section 3.3.1.4.

### *4.3.2 Methods*

#### *4.3.2.1 Experimental Design*

The experiments were conducted on two sand textures: a finer sand texture (OOO Ricci Bros Sand Co., Inc.) and coarser sand texture (Opta Minerals Quartz Silica 49-7-15). The experiments were also conducted at two tensions: a lower tension of -2 cm and a higher tension of -3 cm/-8 cm. Tables 4.1, 4.2, and 4.3 present the breakdown of experiments. The -2 cm tension was selected as the lower tension as it is a tension commonly used in fieldwork and laboratory experiments. The -3 cm tension for ethanol and -8 cm tension for water was selected as the higher tension for comparison. The -8 cm of tension for water was scaled for the difference in surface tension between the two fluids (Table 1.2). The Laplace Equation of Capillarity (Equation 15) shows that the reduction of surface tension by approximately one-third will cause a one-third reduction in capillary pressure. Therefore, the tension value for water was scaled by approximately three times the tension value of ethanol.

#### *4.3.2.2 Homogenous Sand Pack*

The 2-D glass flow cell for these experiments was packed using the continuous pour method described in Section 3.3.2.2. After the sand was homogenously poured into the flow cell, the sand was levelled to ~ 1 mm above the top of the glass flow cell to allow for hydraulic contact between the tension infiltrometer and the sand. Good hydraulic contact between the infiltrometer and porous media is critical for effective use of the apparatus (Beatty & Smith, 2013; Reynolds & Zebchuk, 1996).

#### *4.3.2.3 Experimental Method*

After continuously pouring the sand and before beginning the experiment, the flow cell and camera were checked using beam and circular levels. Once ambient laboratory conditions were established, a specific known volume of 95% ethyl alcohol was applied to the surface of the flow cell using the tension infiltrometer setup (Section 4.3.1.2; Phase 1). Immediately after the ethanol was applied, the surface of the experiment was covered with plastic film to minimize any evaporative loss of moisture or ethanol during the waiting period. The 24-hr waiting period was timed relative to the beginning of the constant head apparatus applying ethanol (Phase 1). The waiting period allowed for infiltration and redistribution of fluids (specifically ethanol) within the flow cell. At the 24-hr mark, a known volume of deionized water was applied to the surface of the flow cell using the same constant head apparatus setup (Phase 2). The surface of the experiment was again immediately covered with plastic film to minimize evaporation during the waiting period of Phase 2. In some experiments during Phase 2, during water

infiltration, a stainless steel laboratory scoop was inserted as a shallow impermeable barrier to prevent the infiltrating water from escaping the antecedent ethanol-contaminated area near the top of the flow cell. There was a subsequent 24- to 72-hr waiting period that began after the beginning of the application of deionized water (Phase 2 and Phase 3). This 24- to 72-hr waiting period provided sufficient time for drainage and redistribution of the applied water to occur in the porous media. The application rates and volumes were verified before and after each application of ethanol and deionized water. The constant head tension remained the same during the entire duration of application period. Fluid ponding was not observed during any of the experiments. The ambient laboratory temperature was continually recorded in consideration of the fluid viscosity and density temperature dependence. The average laboratory temperature was 21.1°C ± 2°C.

#### *4.3.2.4 Image Acquisition*

Photographs using the camera setup (Section 3.3.1.3) were taken in 5-s increments during the first hour of each phase, followed by photographs at 15-min increments during the subsequent drainage and redistribution wetting periods. These photographs were used for visual flow observation and later analyzed and transformed into time-lapse videos for further analysis. Contact the author for access to the time-lapse videos.

## 4.4 Results and Discussion

### *4.4.1 Results*

To better understand the infiltration of water into ethanol-contaminated porous media, three categories of experiments were conducted: Ethanol Following Water Infiltration Porous Media Experiments (Section 4.4.1.1), Water Following Ethanol Infiltration for Lower Tension Constant Head Experiments (Section 4.4.1.2), and Water Following Ethanol Higher Tension Constant Head Experiments (Section 4.4.1.3).

#### *4.4.1.1 Ethanol Following Water Infiltration into Porous Media Experiments*

A series of two base-case ethanol following water infiltration experiments in porous media by way of constant head was conducted on the Opta sand as outlined in Table 4.1. The experimental details are provided in Table 4.1.

Table 4.1. Experimental details for the constant head ethanol following water infiltration porous media experiments. The Opta Minerals Quartz Silica 49-7-15 is a coarser and lighter coloured sand, and the OOO Ricci Bros Co., Inc. Sand is a finer and darker coloured sand.

| Experiment Name | Sand Type | Bulk Density | Tension | Volume of 95% Ethanol Applied | Length of 95% Ethanol Application | Volume of Water Applied | Length of Water Application |
|---|---|---|---|---|---|---|---|
| | | $g/cm^3$ | cm | ml | min | ml | min |
| CH-10 | Opta sand | 1.71 | -2 | 90.5 | 2:35 | 27 | 0:41 |
| CH-11 | Opta sand | 1.70 | -2 | 79 | 1:03 | 33 | 0:52 |

The de-aired, deionized water infiltrated into the unsaturated porous media in a relatively smooth, stable bulb-like shape (Figure 4.2a). Minor downwards migration occurred over the 30-min waiting period. The subsequent 95% ethanol application into the water-infiltrated media created a smooth semicircular and distinguishable interface between ethanol and water content (Figure 4.2c, 4.2d, 4.2e). A zone of lower fluid saturation at the ethanol-water boundary was present; this halo effect is discussed in Section 5.1. As hypothesized, there was no evidence of perturbations or focused flow instability behaviours during this set of experiments in which ethanol infiltrated into water-wet sands. Duplicate experiments were completed to ensure repeatability.


*Figure 4.2.* Ethanol following water infiltration constant head experiment CH-10. Sequenced photographs of experiment CH-10 with time zero being the beginning of water application (a) t = 00:15:03, (b) t = 00:29:44, (c) t = 00:31:54 (start of ethanol application), (d) t = 00:34:00, (e) t = 00:36:00, and (f) t = 00:45:21. Sequenced photographs of experiment CH-11 can be found in the Appendix.

#### *4.4.1.2 Constant Head Application Experiments: Lower Tension*

The lower tension (-2 cm) constant head experiments performed and associated details are outlined in Table 4.2. There were four lower tension constant head experiments performed: two on the Ricci sand and two on the Opta sand. A single focused flow event occurred in each of the lower tension constant flux experiments (Table 4.2).

Table 4.2 Experimental details for the lower tension of the constant head ethanol following water infiltration porous media experiments. The Opta Minerals Quartz Silica 49-7-15 is a coarser and lighter coloured sand, and the OOO Ricci Bros Sand Co., Inc. is a finer and darker coloured sand.

| Experiment Name | Sand Type | Bulk Density | Tension | Volume of 95% Ethanol Applied | Length of 95% Ethanol Application | Volume of Water Applied | Length of Water Application |
|---|---|---|---|---|---|---|---|
| | | $g/cm^3$ | cm | ml | min | ml | min |
| CH-4 | Ricci sand | 1.64 | -2 | 26.5 | 0:58 | 53 | 1:42 |
| CH-5 | Ricci sand | 1.64 | -2 | 26 | 1:02 | 43 | 1:32 |
| CH-7 | Opta sand | 1.72 | -2 | 31.5 | 0:50 | 29 | 0:29 |
| CH-8 | Opta sand | 1.71 | -2 | 32 | 0:57 | 32.5 | 0:21 |

### Phase 1: Antecedent Ethanol Contamination

The 95% ethanol infiltrated into the unsaturated porous media as a smooth, elongated bulb-like shape (Figure 4.3a) during the infiltration of ~ 26 to 32 ml of ethanol over the 8 cm wide contact area. Both sand types saw substantial downwards migration and redistribution of the finite volume of applied ethanol over the course of the 24-hr waiting period that followed (Phase 1; Figure 4.3b). The Ricci sand generated ethanol migration to shallower depths and infiltration at deeper depths to about one-half of the flow cell, whereas the Opta sand reached about three-quarters of the depth of the flow cell.

### Phase 2: Infiltrating Water-Bulb Formation

The focused flow behaviours that follow the application of water on the system are divided into three different growth stages: the water-bulb, the focused flow, and the breakthrough (Figure 4.3). Each stage has distinct visual characteristics.

The water-bulb stage occurred first and began as the de-aired, deionized water infiltrated from the tension infiltrometer into the ethanol-contaminated porous media (Phase 2). The water-bulb continued to grow as the deionized water was being continuously applied from the infiltrometer, which was maintaining a constant pressure head at the surface. The water-bulb phase persisted for a period after the infiltrometer was removed and drainage began near the surface of the sand (Figure 4.3d). The time between the removal of the infiltrometer and the initial visualization of the focused flow was approximately 1.75 to 2.5 hrs for the Opta sand and 1 to 2 hrs for the Ricci sand.

### Phase 2: Focused Flow Formation

The water-bulb stage was followed by the focused flow stage, whereby a preferential focused flow developed as an unstable perturbation of the front at the base of the deionized water-bulb (also the deepest zone of the water-bulb). Subsequently, the water draining from the water-bulb converged upon the perturbation and advanced below the water-bulb into a vertically oriented, narrowly focused preferential flow pathway (Figure 4.3e, 4.3f). The deionized water from within the water-bulb continued to feed the focused flow. The focused flow was not directly fed by the infiltrometer but developed

after the constant pressure head surface stopped. Specifically, the water-bulb grew during the application of water onto the system, which took 1:35 min for the Ricci sand and 0:25 mins for the Opta sand (Table 4.2), and continued to grow slowly for a time after the infiltrometer was removed. The focused flow did grow vertically at the tip but exhibited very little horizontal growth. A zone of lower saturation developed at the ethanol-water boundary, which is the halo effect discussed in Section 5.1. This zone of lower saturation was more prominent in the Opta sand, similar to that observed in the constant flux experiments described in Section 3.4. In each experiment, only one dominant perturbation formed, which occurred in the middle of the base of the water-bulb, which coincides with the deepest part of the water-bulb. These constant head experiments did not show evidence of multiple perturbations forming at the water-ethanol front.

**Phase 3: Breakthrough Formation**

The breakthrough stage followed the focused flow stage. The breakthrough stage occurred when the focused flow reached the base of the antecedent ethanol-contaminated porous media and broke through into the uncontaminated air-dry unsaturated porous media (Figure 4.3g, 4.3h). After breakthrough, the water migrating from the water-bulb essentially bypassed the ethanol-contaminated zone and entered the uncontaminated, unsaturated porous media. During the breakthrough stage, there was a visible and evident drainage front from the upper portion of the wetted region. The drainage event was seen in both the Ricci sand and the Opta sand. The lower tension, short application time, and

controlled volume nature of these lower tension experiments still created conditions that allowed the three stages to develop fully. Contact the author for access to the time-lapse videos.

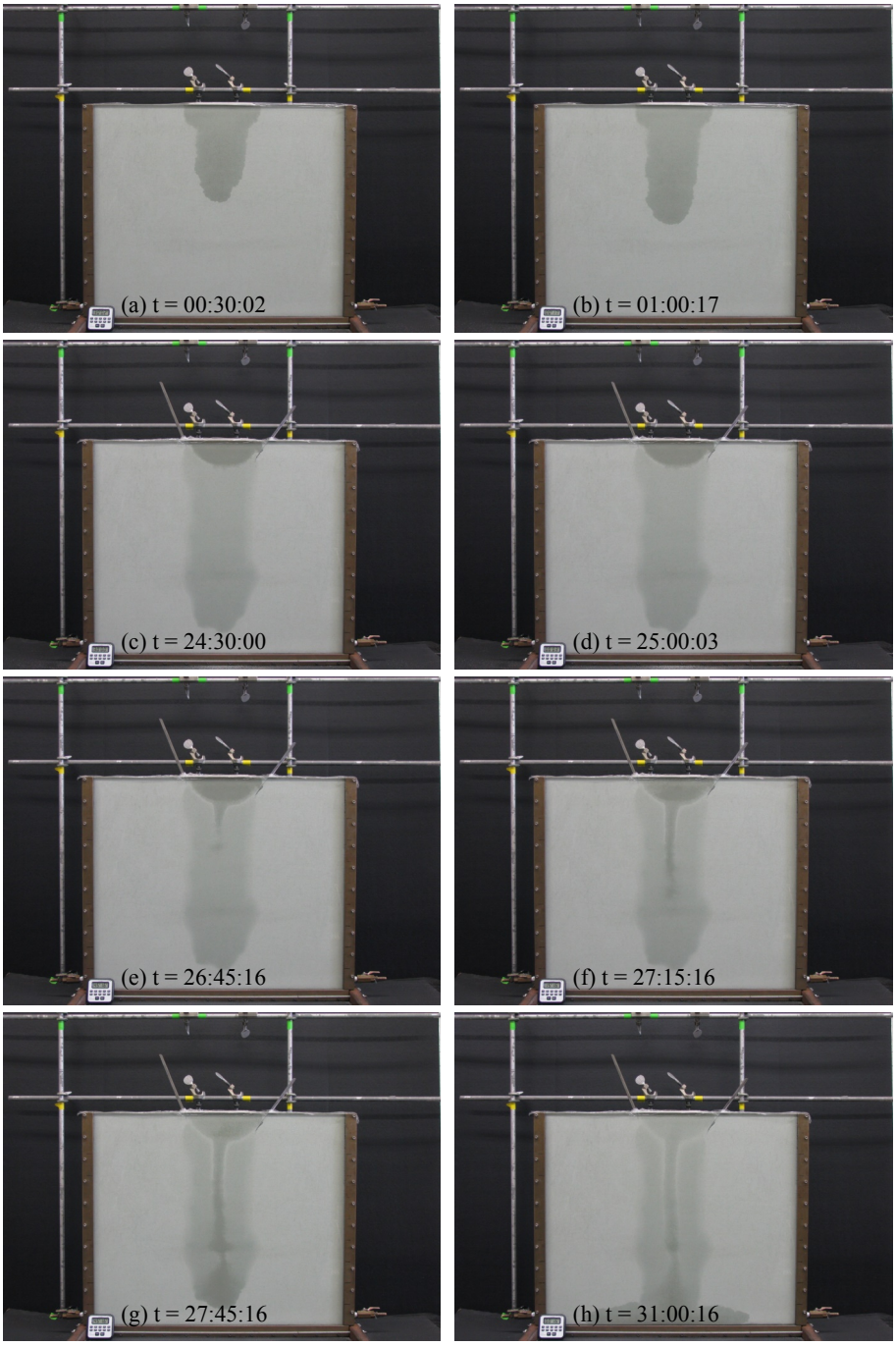


*Figure 4.3.* Lower tension water following ethanol infiltration constant head experiment CH-8. Sequenced photographs of experiment CH-8 with time zero being the beginning of ethanol application (a) t = 00:30:02, (b) t = 01:00:17, (c) t = 24:30:00 (start of water application), (d) t = 25:00:03, (e) t = 26:45:16, (f) t = 27:15:16, (g) t = 27:45:16, and (h) t = 31:00:16. Sequenced photographs of experiments CH-4, CH-5, and CH-7 can be found in the Appendix.

#### *4.4.1.3 Constant Head Application Experiments: Higher Tension*

The higher tension (-3 cm/-8 cm) constant head experiments performed and associated details are outlined in Table 4.3. There were four higher tension constant head experiments performed: two on the Ricci sand and two on the Opta sand. A single focused flow event occurred in each of the lower tension constant flux experiments (Table 4.3).

Table 4.3. Experimental details for the higher tension of the constant head ethanol following water infiltration porous media experiments. The Opta Minerals Quartz Silica 49-7-15 is a coarser and lighter coloured sand, and the OOO Ricci Bros Sand Co., Inc. is a finer and darker coloured sand.

| Experiment Name | Sand Type | Bulk Density | Tension | Volume of 95% Ethanol Applied | Length of 95% Ethanol Application | Volume of Water Applied | Length of Water Application |
|---|---|---|---|---|---|---|---|
| | | $g/cm^3$ | cm | ml | min | ml | min |
| CH-12 | Opta sand | 1.73 | -3/-8 | 31.5 | 1:36 | 31 | 7:30 |
| CH-13 | Opta sand | 1.73 | -3/-8 | 31 | 1:35 | 31 | 4:12 |
| CH-15 | Ricci sand | 1.63 | -3/-8 | 30.5 | 1:46 | 32 | 4:55 |
| CH-16 | Ricci sand | 1.63 | -3/-8 | 31.5 | 1:39 | 32 | 5:37 |

**Phase 1: Antecedent Ethanol Contamination**

The higher tension constant head experiments generated results similar to the lower tension constant head experiments (Section 4.4.1.2). The 95% ethanol infiltrated into the unsaturated porous media as a smooth, elongated bulb-like shape (Figure 4.4a) during the infiltration of ~ 30 to 32 ml of ethanol over the 8 cm wide contact area. Both sand types showed substantial downwards migration of the finite volume of ethanol applied; both

sands reached a depth of approximately one-half to two-thirds of the flow cell (Figure 4.4b). The ethanol drainage and migration is evident in the Opta sand. Ethanol migration and redistribution continued to occur during the 24-hr waiting period (Phase 1).

**Phase 2: Infiltrating Water-Bulb Formation**

Similar to the lower tension constant head experiments, the behaviours during and after the application of water (Phase 2) on the system are divided into three different growth stages: the water-bulb, the focused flow, and the breakthrough.

The water-bulb stage began to appear immediately after the application of the de-aired, deionized water onto the contaminated porous media (Figure 4.4c, 4.4d). The water-bulb continued to grow as the deionized water was being continuously applied by the infiltrometer, which was maintaining a constant pressure head at the surface. The water-bulb persisted for a period after the infiltrometer was removed and drainage began near the sand surface.

**Phase 2: Focused Flow Formation**

The focused flow stage began when a preferential focused flow developed as an unstable perturbation front at the base of the deionized water-bulb (the deepest zone of the water-bulb). Subsequently, the de-aired water from the water-bulb converged upon perturbation and advanced below the water-bulb in a vertically oriented, narrowly focused preferential flow pathway (Figure 4.4e, 4.4f).

During experiments CH-12, CH-15, and CH-16, there was no lag time between the removal of the infiltrometer after water application and the initial visualization of the focused flow event. However, experiment CH-13 had a lag time between the removal of the apparatus and the initial visualization of upwards of two hours. The focused flow grew vertically at the tip and exhibited very little horizontal growth. All four higher tension experiments exhibited bifurcation or multiple unstable focused flow formations. This is addressed in Section 4.4.2.5.

One noteworthy difference in the higher tension experiments is that the focused flow began to form as the constant head tension infiltrometer was still applying water. That is, there was no delay in the development of the perturbation and unstable focused flow; specifically, drainage was not needed at the surface. This means that hysteresis in the hydraulic functions was not playing a role in the initiation of the focused flow event in this case. A zone of lower saturation at the ethanol-water boundary was present; this will

be discussed further in Section 5.1. Similar to the lower tension constant flux experiments, this zone of lower saturation was more prominent in the Opta sand.

**Phase 3: Breakthrough Formation**

During the breakthrough stage (Figure 4.4g, 4.4h), the infiltrated water broke through into the uncontaminated, air-dry unsaturated sand with an observable drainage front. Similar to the lower tension experiments, the drainage front was seen in both the Ricci sand and the Opta sand but was more pronounced in the Opta sand. The water-bulb, focused flow, and breakthrough stages continued until drained into the previously uncontaminated, air-dry unsaturated porous media (Figure 4.4h). As the water drained into the previously unsaturated sand, an evident drainage front occurred in the upper wetted portion. After breakthrough, water migrating from the water-bulb essentially bypassed the ethanol-contaminated zone when migrating from the water-bulb to the air-dry unsaturated zone. Duplicate experiments were completed for each experiment and sand type to ensure repeatability.

The higher tension and relatively slower application time of the known volumes created a scenario of similar resemblance to the lower volume and higher flux pulse experiments discussed in Section 5.3, except for the initiation of the focused flow event. These experiments are compared and discussed further in Section 5.

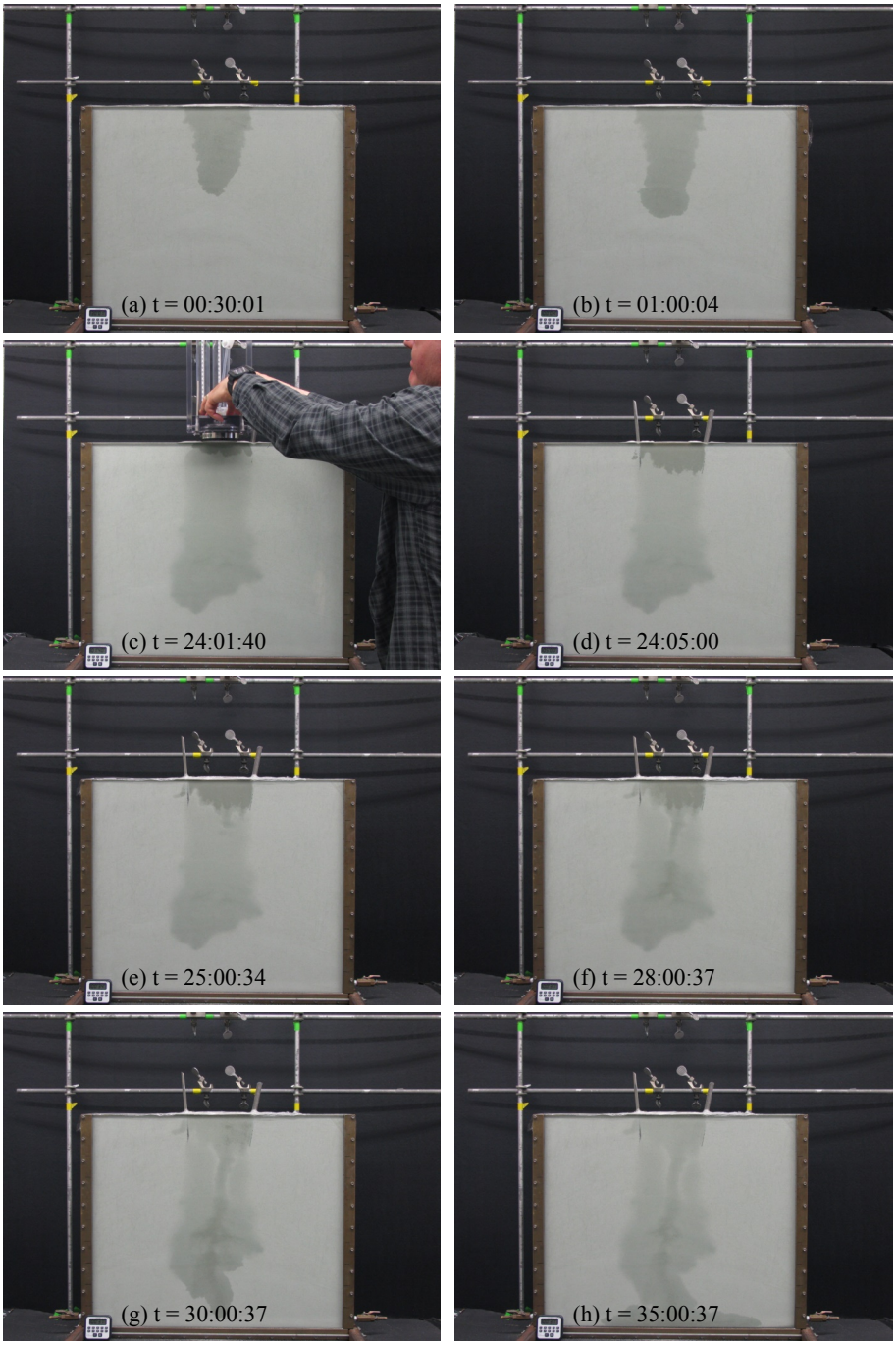


*Figure 4.4.* Higher tension water following ethanol infiltration constant head experiment CH-13. Sequenced photographs of experiment CH-13 with time zero being the beginning of ethanol application (a) t = 00:30:01, (b) t = 01:00:04, (c) t = 24:01:40 (start of water application), (d) t = 24:05:00, (e) t = 25:00:34, (f) t = 28:00:37, (g) t = 30:00:37, and (h) t = 35:00:37. Sequenced photographs of experiments CH-15 and CH-16 can be found in the Appendix.

### *4.4.2 Discussion*

#### *4.4.2.1 Comparison between Constant Head Experiments*

Constant head experiments where deionized, de-aired water infiltrated into antecedent ethanol-contaminated porous media exhibited vertical-flow events. Experiments where ethanol infiltrated into antecedent water did not exhibit focused flow events. These findings support the hypotheses of this thesis.

Both the lower tension and higher tension constant head experiments supported the hypothesis of this thesis. As seen in Table 4.2 and Table 4.3, the only experimental condition difference between the experimental method behind the constant head lower tension and higher tension experiments was the difference in tension. Other than the time and prevailing conditions at the time of initiation of focused water flow (SCIFF), the difference in tension between the lower tension and higher tension experiments only produced minor notable differences.

**Constant Head Application Experiments: Lower Tension**

The lower tension constant head experiments are outlined and presented in Table 4.2 and on Figure 4.3, respectively. The most notable difference was the shorter length of application time in the lower tension experiments (Table 4.2). As capillary pressure became less negative (lower tension), only pores for a certain range of capillary pressures were filled. Therefore, under lower tension infiltration, the smallest pores (highest

capillary pressures) were not filled, and the infiltrating front reached greater depths in the flow cell.

### Constant Head Application Experiments: Higher Tension

The higher tension constant head experiments are outlined and presented in Table 4.3 and on Figure 4.4, respectively. The most notable difference was the longer length of application time in the higher tension experiments (Table 4.3). As capillary pressure became more negative (or tension increased), the range of pores sizes (or capillary pressures) that could be filled decreased (the largest size assemblage of pores remained air filled). Therefore, under higher tension infiltration, the smallest pores (highest capillary pressures) were filled, and the infiltrating front migrated a shorter depth in the flow cell than the lower tension experiments under comparable volumes. The volume of ethanol applied under both low tension and high tension was relatively similar. However, the lower tension experiments redistributed within a greater area of porous media. This created a scenario whereby the moisture content was slightly greater in the higher tension experiments compared to the lower tension experiments. In both the lower and higher tension experiments, the there was a lag time between the water application in the water-bulb formation and the initial start of the focused flow. The lag time was more prominent in the higher tension experiment series, and the focused flow event began while the infiltrometer was still maintaining a constant head at the surface.

#### *4.4.2.2 Ethanol-Water Boundary Zone of Lower Saturation (Halo Effect)*

The zone of lower moisture content or saturation at the ethanol-water boundary surrounding the focused flow event (Figure 4.5) has been termed the halo effect. This narrow region of localized drainage is a characteristic of the SCIFF effect (Smith et al., 2011). The phenomenon is present in all water following ethanol infiltration experiments to some degree and is presented in experiment CH-8. This zone of lower saturation is present in both sand types. However, it is more pronounced in the Opta sand due to the properties of the sand. This effect will be discussed in detail in Section 5.1.

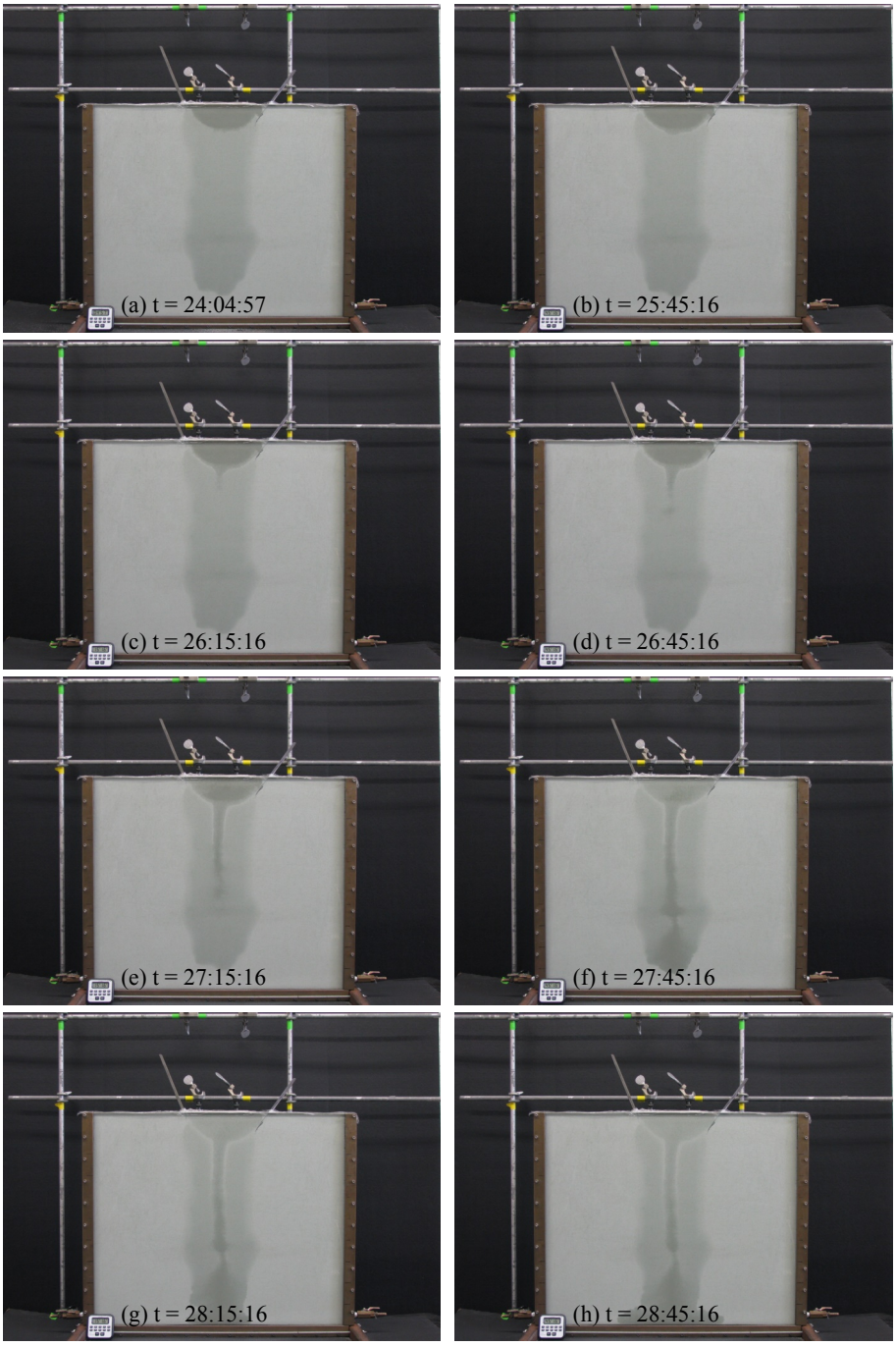


*Figure 4.5.* The ethanol-water boundary zone of lower saturation (halo effect) in experiment CH-8. The sequenced photographs begin with time zero being the beginning of ethanol application (a) t = 24:04:57 (application of water stopped at 24:00:21), (b) t = 25:45:16, (c) t = 26:15:16, (d) t = 26:45:16, (e) t = 27:15:16, (f) t = 27:45:16, (g) t = 28:15:16, and (h) t = 28:45:16.

#### *4.4.2.3 Cumulative Infiltration vs. Time*

Cumulative infiltration is defined as the accumulated volume of infiltrated fluid in porous media over a given period. In wettable porous media systems, the rate of infiltration decreases with time, whereas in hydrophobic systems, the rate of infiltration increases with time (Beatty & Smith, 2013). Due to the experimental constraints (i.e., volume of fluid applied), the system did not undergo a decrease in cumulative infiltration rate at late-time. Therefore, there was no discernable difference between early-time cumulative infiltration and late-time cumulative infiltration. As can be seen in Table 4.4 and Table 4.5, water infiltrates into the porous media at a faster rate than ethanol due to the physical properties of each fluid. The difference in infiltration rate was also observed visually during experimentation.

**Cumulative Ethanol Infiltration vs. Time**

The cumulative ethanol infiltration applied under higher tension (-3 cm) for both the Opta and Ricci sands were lower than the cumulative ethanol infiltration applied under lower tension (-2 cm) for both sands (Figure 4.6). As anticipated, the higher tension experiments resulted in a lower cumulative infiltration when compared to the lower tension experiments. The slope of the cumulative ethanol infiltration versus time indicates the rate at which the fluid was applied (Figure 4.6). As seen by the trend lines, there is variability between the infiltration rates between experiments (Figure 4.6). The same volume of ethanol application was targeted for both lower tension and higher tension experiments; however, due to the slower rate of the higher tension experiments, a longer application

time was required (Figure 4.6). The cumulative infiltration rate of ethanol infiltration into water-saturated sands (indicated by black points) falls in the same range as the lower tension experiments as that series of experiments was also set to a lower tension.

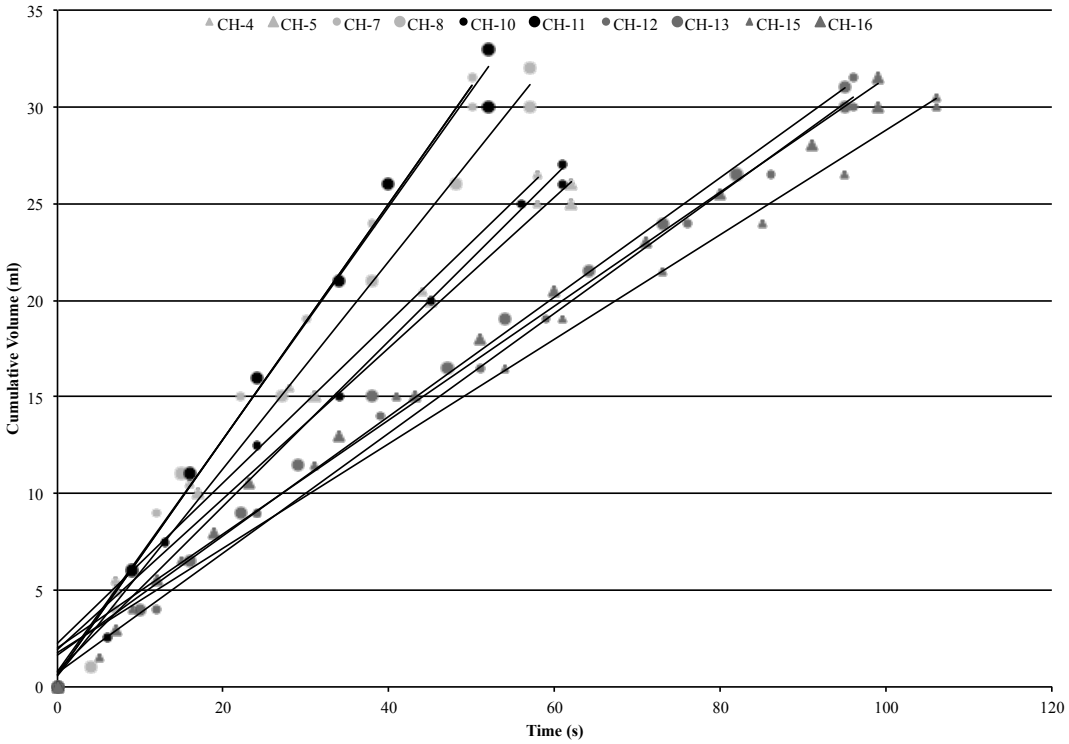


*Figure 4.6.* Cumulative ethanol infiltration vs. time for Opta Minerals Quartz Silica 49-7-15 and OOO Ricci Bros Sand Co., Inc. constant head experiments. The symbologies are as follows: Lower Tension on OOO Ricci Bros. Co., Inc. ▲, Lower Tension on Opta Minerals Quartz Silica 49-7-15 •, Higher Tension on OOO Ricci Bros. Co., Inc. ▲, Higher Tension on Opta Minerals Quartz Silica 49-7-15 •, and Ethanol Following Water Infiltration (Lower Tension on Opta Minerals Quartz Silica 49-7-15) •.

Table 4.4. Average ethanol cumulative infiltration rates for Opta Minerals Quartz Silica 49-7-15 and OOO Ricci Bros Sand Co., Inc. constant head experiments.

| Sand Type | Experiment Type | Average Cumulative Infiltration Rate |
|---|---|---|
| | | ml/s |
| Opta sand | Lower Tension | 0.573 |
| | Higher Tension | 0.310 |
| Ricci sand | Lower Tension | 0.403 |
| | Higher Tension | 0.283 |

### Cumulative Water Infiltration vs. Time

The cumulative water infiltration applied under higher tension (-8 cm) for both the Opta sand and the Ricci sand was lower than the cumulative water infiltration applied under lower tension (-2 cm) for the same sand types (Figure 4.7). Similarly to the cumulative ethanol infiltration, the higher tension experiments resulted in a lower cumulative infiltration when compared to the lower tension experiments. However, there is much larger variability between the tension settings in the cumulative water application, as seen by the trend lines (Figure 4.7), than in the cumulative ethanol infiltration (Figure 4.6). The water infiltration under higher tension was set to -8 cm, whereas for the same experiments, the ethanol infiltration was set to a tension of -3 cm. Therefore, the increased variability between the lower and higher tension experiments was primarily due to the difference between the tension settings in the higher tension experiments. To reiterate, the same volume of water was targeted when applying both lower and higher tension. Therefore, with a slower rate of infiltration in the higher tension experiments, the application time was longer. The cumulative infiltration rate of water into unsaturated

sands (indicated by black points) was applied by lower tension and aligns accordingly with those trend lines (Figure 4.7).

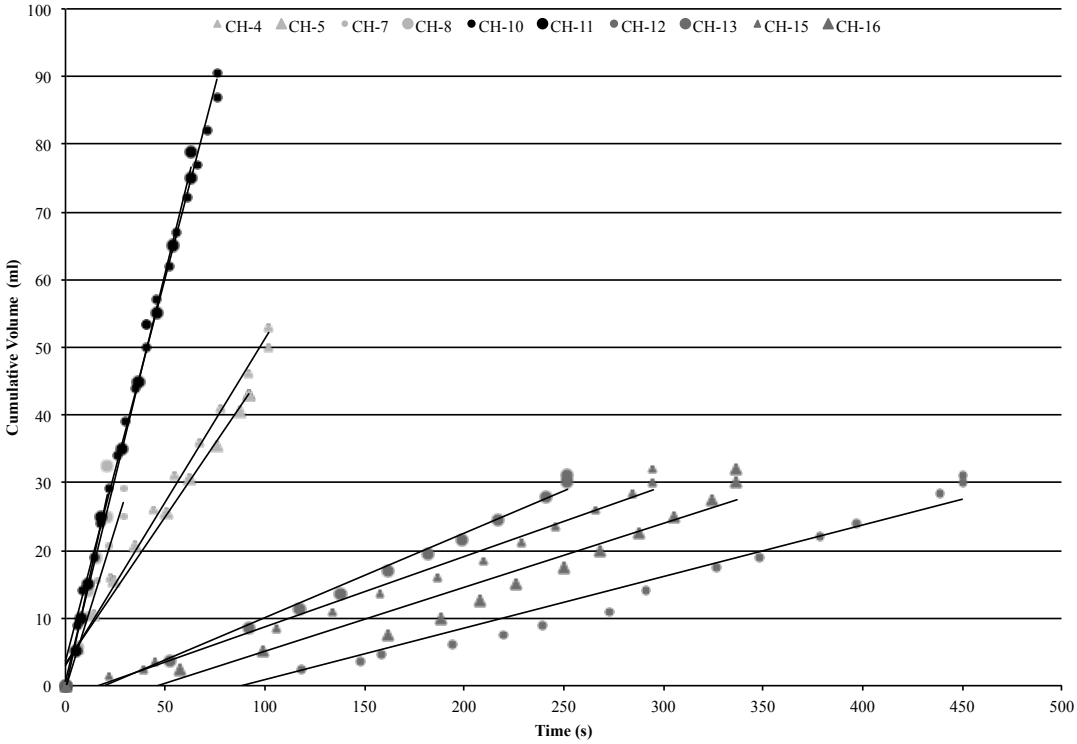


*Figure 4.7.* Cumulative water infiltration vs. time for Opta Minerals Quartz Silica 49-7-15 and OOO Ricci Bros Sand Co., Inc. constant head experiments. The symbologies are as follows: Lower Tension on OOO Ricci Bros. Co., Inc. ▲, Lower Tension on Opta Minerals Quartz Silica 49-7-15 •, Higher Tension on OOO Ricci Bros. Co., Inc. ▲, Higher Tension on Opta Minerals Quartz Silica 49-7-15 •, and Ethanol Following Water Infiltration (Lower Tension on Opta Minerals Quartz Silica 49-7-15) •.

Table 4.5. Average water cumulative infiltration rates for Opta Minerals Quartz Silica 49-7-15 and OOO Ricci Bros Sand Co., Inc. constant head experiments.

| Sand Type | Experiment Type | Average Cumulative Infiltration Rate |
|---|---|---|
| | | ml/s |
| Opta sand | Lower Tension | 1.160 |
| | Higher Tension | 0.101 |
| Ricci sand | Lower Tension | 0.458 |
| | Higher Tension | 0.099 |

#### *4.4.2.4 Cumulative Infiltration vs. Root Time*

Cumulative infiltration for root time is common practice and provides a different perspective and additional support for the relationships described in Section 4.4.2.3.

**Cumulative Ethanol Infiltration vs. Root Time**

Similarly to cumulative infiltration versus time, against root time, the cumulative ethanol infiltration applied under higher tension (-3 cm) was lower than the cumulative ethanol infiltration applied under lower tension (-2 cm) for both sands (Figure 4.8). Furthermore, the cumulative infiltration rate of lower tension ethanol infiltration into water-saturated sands fell in the same range as the lower tension experiments (Figure 4.8). There was a larger range of variability in both sands under lower tension. However, variability in data was present in both sands and tensions. All trend lines see a convex relationship that tends to increase upwards. The targeted volume of ethanol applied during these experiments was similar; therefore, most of the trend lines terminate at ~ 30 ml.

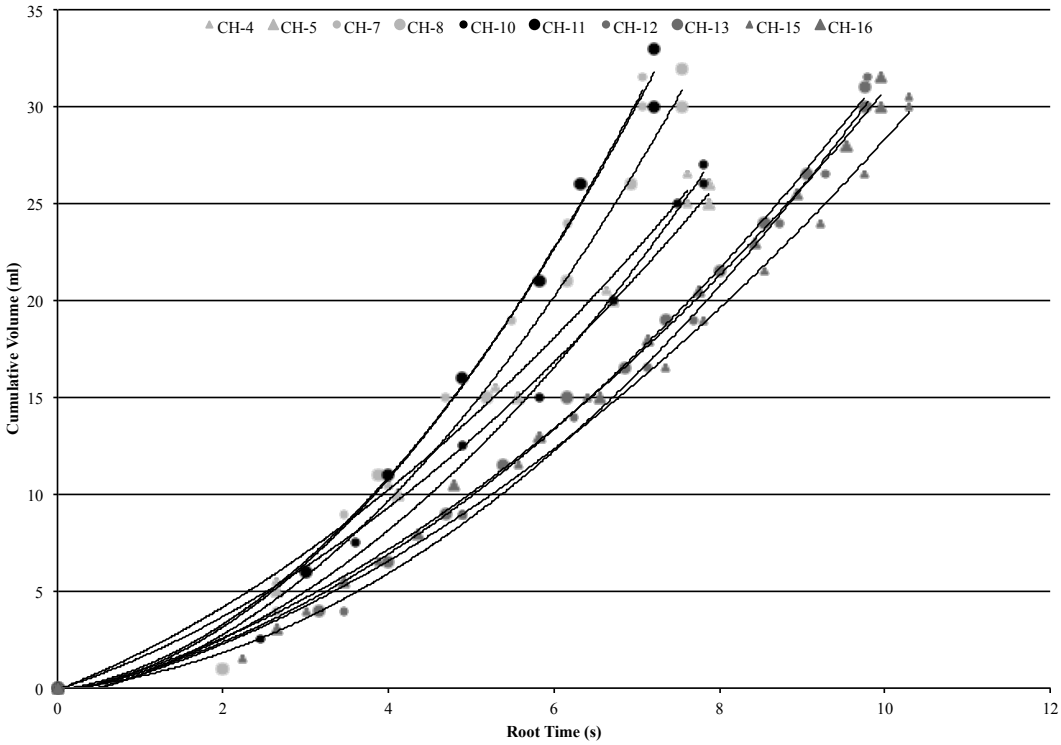


*Figure 4.8.* Cumulative ethanol infiltration vs. root time for Opta Minerals Quartz Silica 49-7-15 and OOO Ricci Bros Sand Co., Inc. constant head experiments. The symbologies are as follows: Lower Tension on OOO Ricci Bros. Co., Inc. ▲, Lower Tension on Opta Minerals Quartz Silica 49-7-15 •, Higher Tension on OOO Ricci Bros. Co., Inc. ▲, and Higher Tension on Opta Minerals Quartz Silica 49-7-15 •, and Ethanol Following Water Infiltration (Lower Tension on Opta Minerals Quartz Silica 49-7-15) •.

### Cumulative Water Infiltration vs. Root Time

Similarly to cumulative infiltration versus time, against root time, the cumulative water infiltration applied under higher tension (-8 cm) was lower than the cumulative water infiltration applied under lower tension (-2 cm) for both sands (Figure 4.9). There is large variability between the tension settings in the cumulative water infiltration trend lines (Figure 4.9). Furthermore, the cumulative infiltration rate of lower tension ethanol infiltration into water-saturated sands fell in the same range as the lower tension experiments (Figure 4.9). All trend lines see a convex relationship that tends to increase

upwards. The targeted volume of ethanol applied during these experiments was similar; therefore, most of the trend lines terminate at ~ 30 ml.

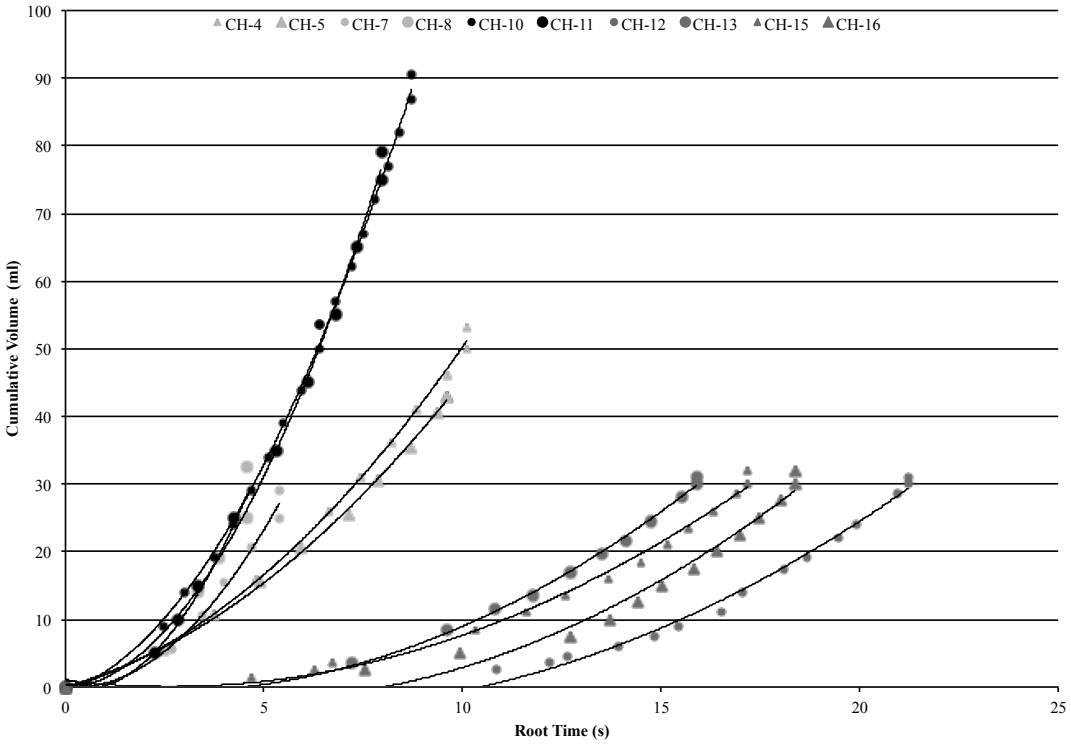


*Figure 4.9.* Cumulative water infiltration vs. root time for Opta Minerals Quartz Silica 49-7-15 and OOO Ricci Bros Sand Co., Inc. constant head experiments. The symbologies are as follows: Lower Tension on OOO Ricci Bros. Co., Inc. ▲, Lower Tension on Opta Minerals Quartz Silica 49-7-15 •, Higher Tension on OOO Ricci Bros. Co., Inc. ▲, Higher Tension on Opta Minerals Quartz Silica 49-7-15 •, and Ethanol Following Water Infiltration (Lower Tension on Opta Minerals Quartz Silica 49-7-15) •.

#### *4.4.2.5 Finger Length vs. Time*

The finger length growth rate can provide valuable insights into the focused flow initiation and development. Finger length was manually measured from the base of the bulb to the finger tip and plotted against time (Figure 4.10) for each type of experiment. The slope of the trend line indicates velocity; therefore, experiments with the same slope

indicate the same finger growth velocity (Zhang & Smith, 2001; Zhang & Smith, 2002). For both types of experiments, finger growth rate is constant (Figure 4.10).

**Lower Tension Experiments**

All duplicate experiments have comparable slope values, thereby similar finger growth velocities (Figure 4.10). At the same tension, the Opta sand had finger growth rates of ~ 0.34 cm/min, whereas the Ricci sand had finger growth rates of ~ 0.07 cm/min (Figure 4.10). This result was expected due to sand characteristic differences and visual observations during the experiment that observed the same trend.

**Higher Tension Experiments**

At higher tension, the Opta sand had finger growth rates of ~ 0.14 cm/min, whereas the Ricci sand had finger growth rates of ~ 0.27 cm/min (Figure 4.10). A higher finger growth was not anticipated in the Ricci sand. However, these discrepancies could be due to the bifurcation and minor heterogeneities present in the higher tension Opta sand experiments.

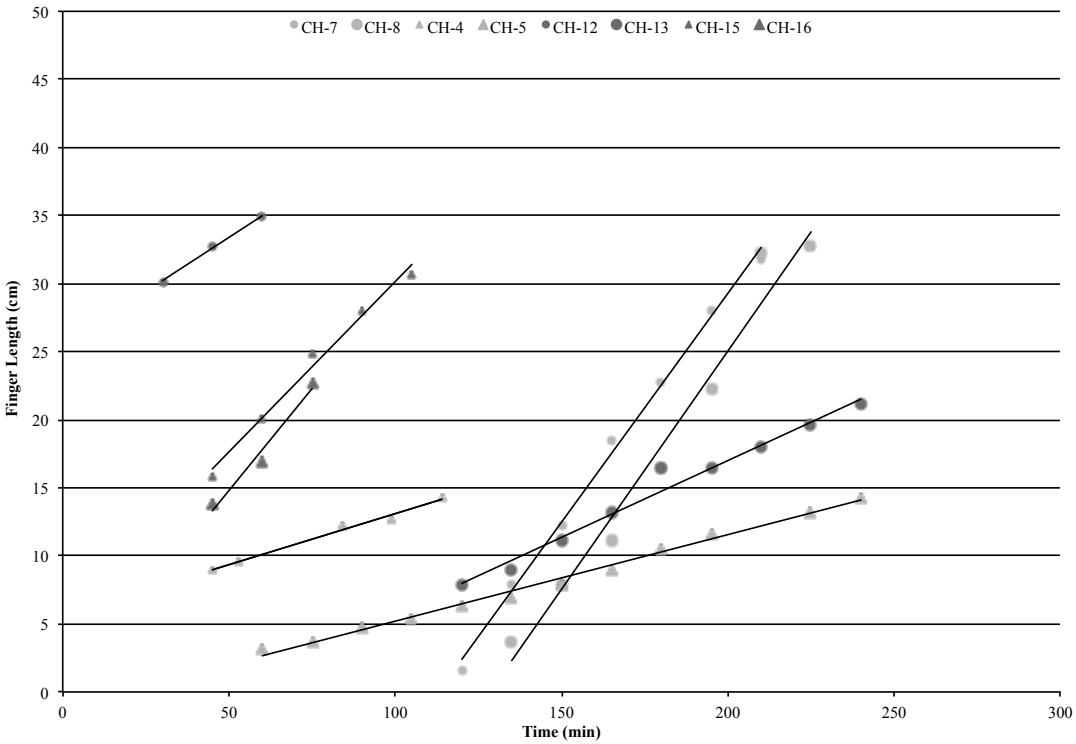


*Figure 4.10.* Finger length vs. time for Opta Minerals Quartz Silica 49-7-15 and OOO Ricci Bros Sand Co., Inc. constant head experiments with time zero beginning at the start of water application. The symbologies are as follows: Lower Tension on OOO Ricci Bros. Co., Inc. ▲, Lower Tension on Opta Minerals Quartz Silica 49-7-15 •, Higher Tension on OOO Ricci Bros. Co., Inc. ▲, and Higher Tension on Opta Minerals Quartz Silica 49-7-15 •.

#### *4.4.2.6 Moisture Content*

The glass flow cell and sand types expressed moisture content and changes in moisture content well. The relatively higher moisture content sand was defined by the darkest shades of sand, and the relatively lower moisture content sand was defined by the lighter coloured sand. Generally speaking, the centre of the narrowly focused flow had the highest visible moisture content. The air-dry unsaturated sand is evident as it remained the same colour before the experiment and was the lightest shade. The zones of sand that

underwent wetting events became visibly darker, and during drainage events, the sand became visibly lighter in colour. The zone of lower moisture content visible at the ethanol-water boundary became visibly lighter as the phenomenon became more prominent. The zone of lower moisture content, or the halo effect, is discussed in more detail in Section 5.1.

#### *4.4.2.7 Heterogeneities*

Although minor heterogeneity added complexity to the system and was not targeted during this experimental series, valuable insights can be drawn from heterogeneously packed porous media. The heterogeneities evident during these experiments were due to the nature of the flow cell packing method used (Section 3.3.2.2).

All constant head experiments were affected by varying degrees of minor heterogeneity. Heterogeneity was specifically noted in constant head experiment CH-13 (Figure 4.11). As shown on Figure 4.11g and Figure 4.11h, the focused flow behaviour overcame the effects of all heterogeneities present in the porous media.

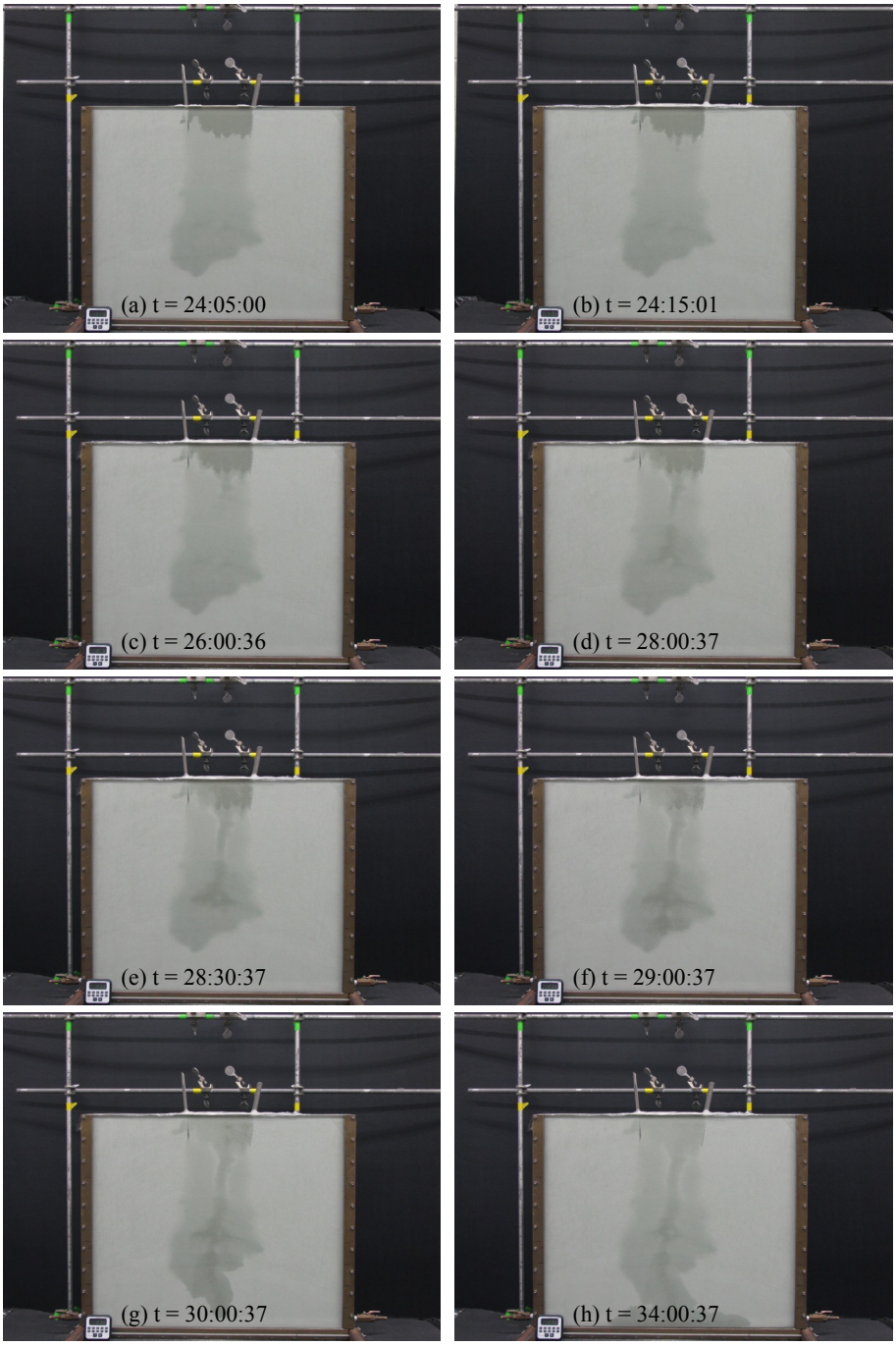


*Figure 4.11.* Water following ethanol infiltration constant head experiment CH-13 exhibiting minor heterogeneity. Sequenced photographs of experiment CH-13, with time zero being the beginning of ethanol application (a) t = 24:05:00 (b) t = 24:15:01, (c) t = 26:00:36, (d) t = 28:00:37, (e) t = 28:30:37, (f) t = 29:00:37, (g) t = 30:00:37, and (h) t = 34:00:37.

#### *4.4.2.8 Bifurcation*

Bifurcation is the process by which a focused flow event splits into two distinct focused flow events due to minor heterogeneities at the tip of the advancing finger (Zhang & Smith, 2001). Similar to larger scale heterogeneity, bifurcation adds complexity in understanding the system and is a consequence of heterogeneous packing.

Bifurcation was noted specifically in experiment CH-13 (Figure 4.12). Experiment CH-13 displayed a singular focused flow event that bifurcated at approximately 28:00:37 (Figure 4.12e). Rather than advancing, the additional pathways were subsequently drained once the primary focused flow broke through at depth.

Although experiment CH-12 (Figure 4.13) resembled bifurcation, true bifurcation did not occur. The application of water (Phase 2) was uneven and applied at two locations (Figure 4.13c), which resulted in two initial unstable displacements. The two unstable displacements resulted in two singular focused flow events. This phenomenon was also noted in experiments CH-15 and CH-16.

Finger growth over time for experiments that displayed multiple initial unstable displacements is presented on Figure 4.14. Experiment CH-12 showed the shortest overall time for finger growth as the infiltrating water was split between two unstable flow fingers (Figure 4.14). Experiment CH-15 and CH-16 showed similar visual initial unstable displacements, which was supported by similar graphical finger length growth.

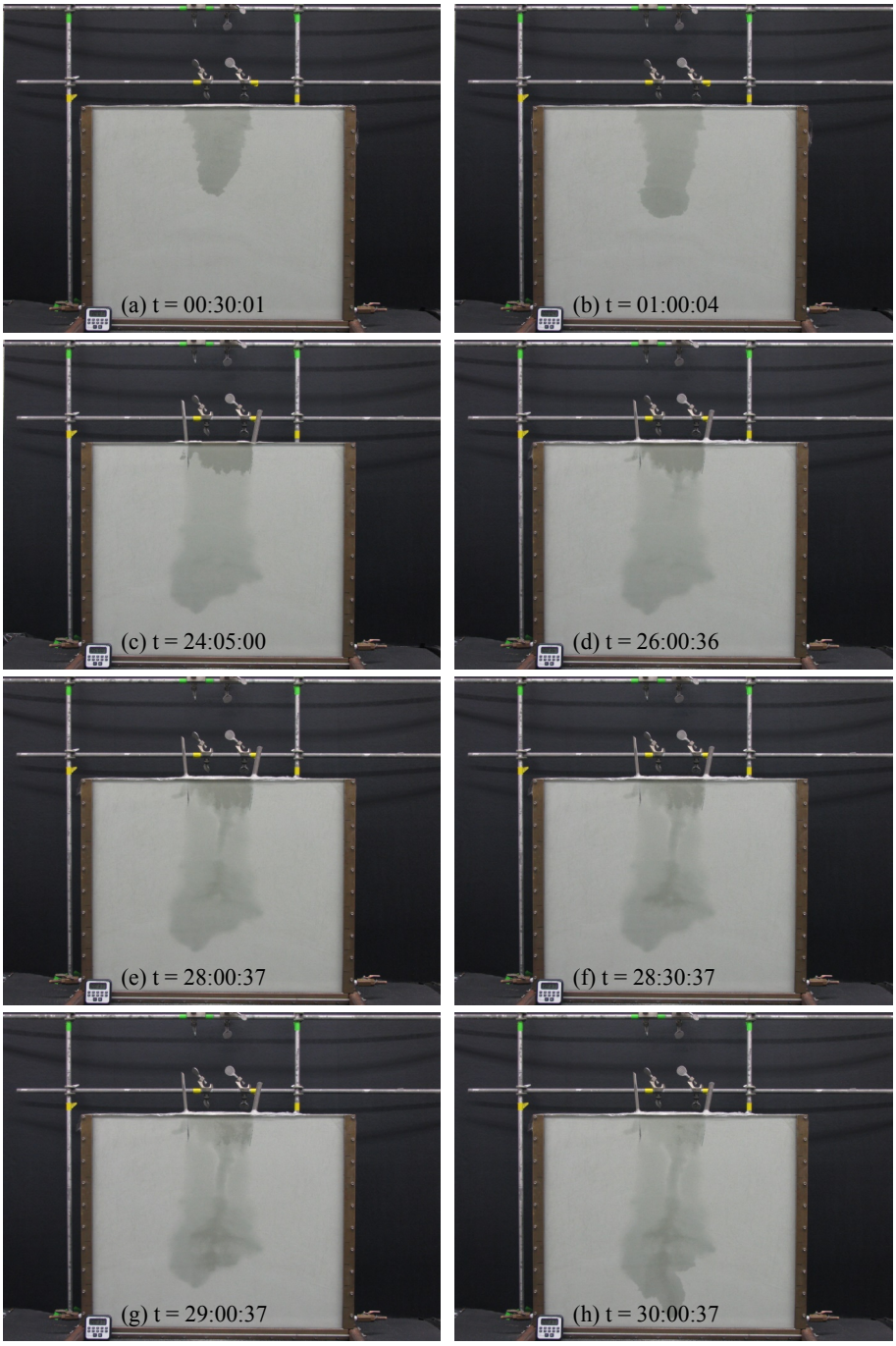


*Figure 4.12.* Water following ethanol infiltration constant head experiment CH-13 exhibiting bifurcation. Sequenced photographs of experiment CH-13 with time zero being the beginning of ethanol application (a) t = 00:30:01, (b) t = 01:00:04, (c) t = 24:05:00 (start of water application), (d) t = 26:00:36, (e) t = 28:00:37, (f) t = 28:30:37, (g) t = 29:00:37, and (h) t = 30:00:37.

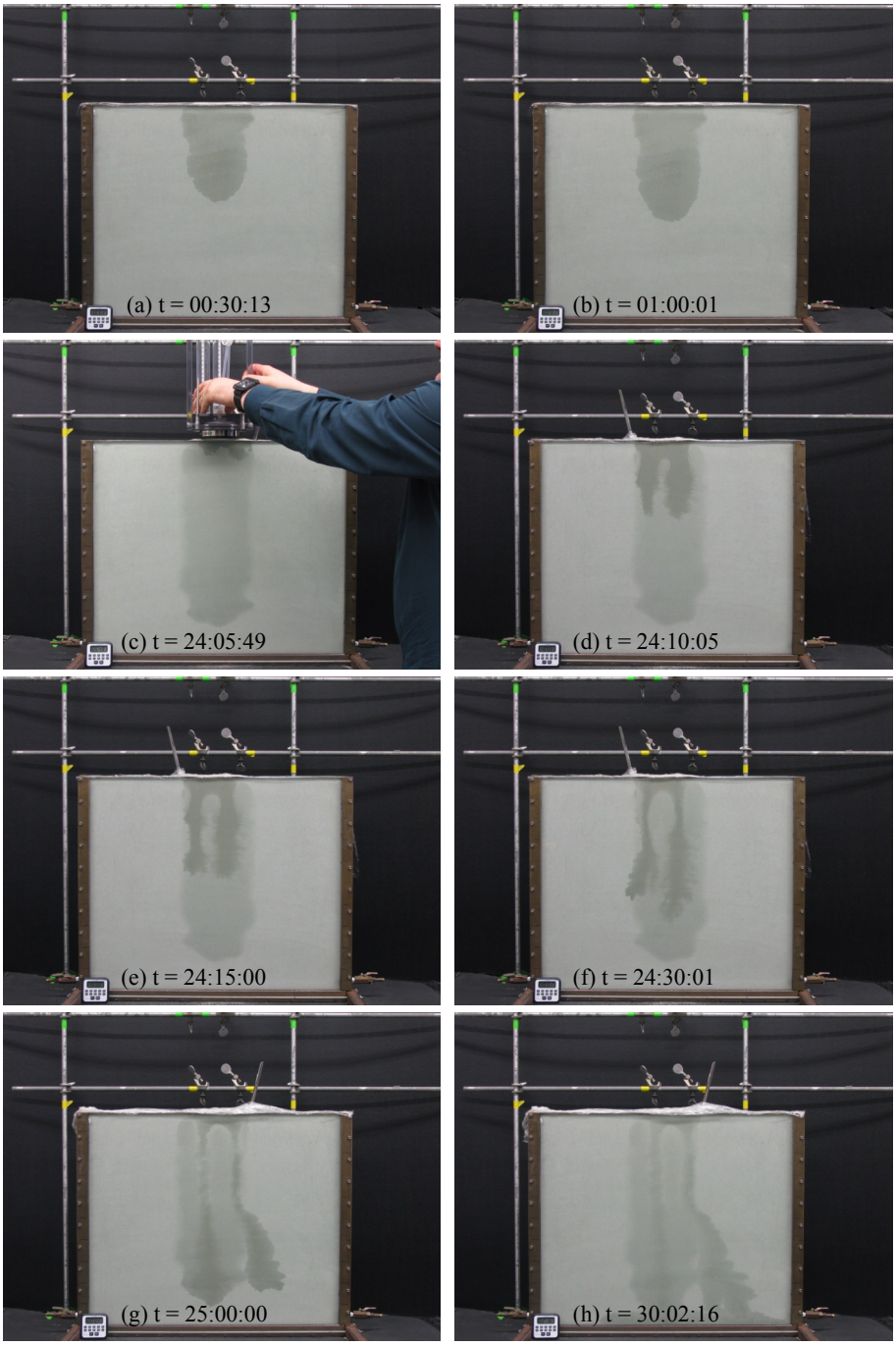


*Figure 4.13.* Water following ethanol infiltration constant head experiment CH-12 exhibiting two unstable displacements resulting in two focused flow events. Sequenced photographs of experiment CH-12 with time zero being the beginning of ethanol application (a) t = 00:30:13, (b) t = 01:00:01, (c) t = 24:05:49 (start of water application), (d) t = 24:10:05, (e) t = 24:15:00, (f) t = 24:30:01, (g) t = 25:00:00, and (h) t = 30:02:16.

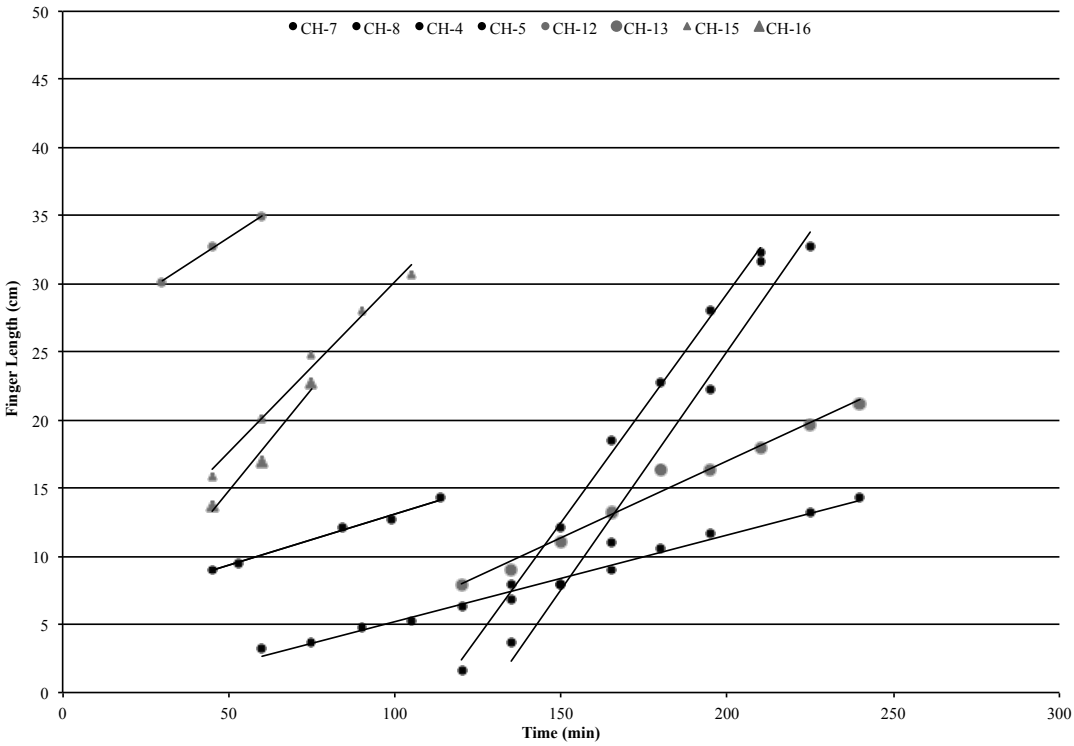


*Figure 4.14.* Comparison of finger length vs. time between singular focused flow experiments, multiple initial unstable displacements experiments (CH-12, CH-15, & CH-16), and bifurcated experiments (CH-13). Time zero is the start of water application. The symbologies are as follows: Higher Tension on OOO Ricci Bros. Co., Inc. ▲, and Higher Tension on Opta Minerals Quartz Silica 49-7-15 •, and singular focused flow experiments •.

#### *4.4.2.9 Effects of the Application Method*

The experimental outcome can be strongly influenced by the method of fluid application. However, there was no evidence that the tension infiltrometer impacted the experimental outcome.

## 4.5 Conclusions

Water infiltrating into ethanol-contaminated porous media by application method of constant head exhibited focused flow. There was no evidence of focused flow behaviours

in ethanol following water infiltration porous media experiments by constant head application. The presence of the antecedent ethanol creates a condition where the liquid pressure heads—due to capillarity—will be functionally dependent upon on both the volumetric moisture content and the aqueous ethanol concentration of the liquid (water) through its functional relation with interfacial (surface) tension at the air-liquid interfaces. This functional relation between ethanol content and liquid (water) pressure heads is the primary driver behind SCIFF. Additionally, the highly non-linear relation between kinematic viscosity and ethanol concentration with its maximum around 40% by volume ethanol further contributes to sharpening the solute front between ethanol and water; this enhances the zone of lower saturation surrounding the focused flow event (the halo effect).

# 5 Unique Findings

## 5.1 Ethanol-Water Boundary Zone of Lower Saturation (Halo Effect)

The ethanol-water boundary zone of lower saturation, or the halo effect, was evident in the experiments of this thesis. This phenomenon was previously reported by Smith et al. (2011) for water infiltration into butanol-contaminated porous media. Relative to the case for butanol-contaminated porous media, the ethanol experiments reported here exhibit a stronger halo effect on either side of the focused flow region that is notably wider relative to the width of the focused flow region.

This effect is a result of ethanol concentration gradients within this boundary zone linked to local relative hydraulic gradients. Within the zone of lower moisture content, the surrounding ethanol region has higher relative pressure heads (lower magnitude capillary pressure) than the lower relative pressure head in water dominant focused flow. This pressure head gradient induced a zone of lower moisture content. Furthermore, the infiltrating water has a higher surface tension than the surrounding lower surface tension ethanol, creating a zone of increased flux (Table 1.2). This increased flux creates increased drainage within the zone of lower saturation. Graphs displaying moisture content, relative concentration, and pressure head for distances along a cross-sectional area (Figure 5.1) created by Smith et al. (2011) did provide further insights.

The ethanol-contaminated sand showed enhanced halo effects compared to the previously reported butanol-contaminated sand (Smith et al., 2011). This is likely due to the differences in kinematic viscosity relations with aqueous concentrations of butanol and ethanol. The kinematic viscosity of a fluid is related to its density (Figure 1.2). The effects of density and surface tension are smaller than that of kinematic viscosity. The miscibility of ethanol and water creates a mixing zone at the boundary of the two fluids. As explained in Section 1.12, the kinematic viscosity of ethanol concentrations is highly non-linear with a maximum in ethanol concentration-dependent, viscosity-induced reduction in hydraulic conductivity, which occurs due to the sludge effect between 40% to 50% ethanol (Figure 1.2). Butanol does not have that same effect regarding kinematic viscosity. The fluid interplay at the ethanol-water interface has a concentration of 40% to

50%; therefore, the highest viscosity ethanol is present within the halo. A concentration of 40% to 50% ethanol will exist within the halo region, which is bound by 95% ethanol outside the focused flow event region and 100% water at the centre of the focused flow event. The detailed inspection of this effect through numerical modelling is beyond the scope of this thesis.

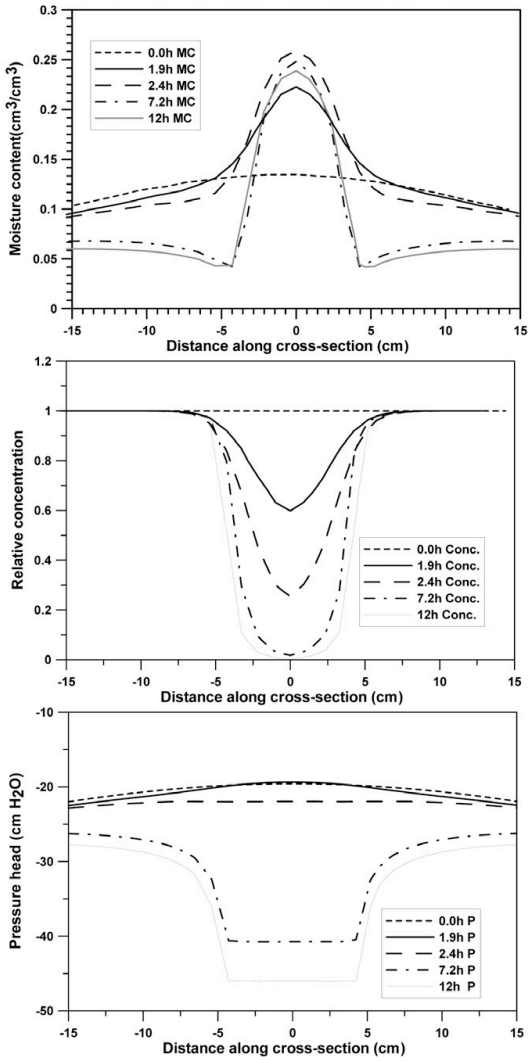


*Figure 5.1.* Simulated moisture content, relative concentration, and pressure head vs. distance along a horizontal cross-section. Water is applied by constant flux at the point source to a 7% butanol-contaminated porous media. Figure from Smith et al. (2011).

## 5.2 Fluid Flow around the Focused Flow

Understanding the interplay between ethanol-contaminated sand and infiltrating water at the tip of the infiltrating focused flow (Figure 5.2) is critical to understanding the system. The tip of the focused flow (SCIFF) front is stabilized by kinematic viscosity. The miscibility of water and ethanol allows for mixing to occur at the water-ethanol interface. At this interface, the kinematic viscosity maximum (Table 1.2) slows down the infiltrating water, creating higher water content at the tip of the focused flow. The tip sees the maximum water content (Figure 5.2). This phenomenon was termed the sludge effect by Beatty and Smith (2014; Section 1.12.6). Gravity is still a dominating force in this system. The constant and steady finger rate observed indicates that surface tension and viscosity effects remain constant in the system. A rind outlining the base of the focused flow (Figure 5.2) differs from the halo effect described in Section 5.1. The rind is a wider, stabilizing (compared to the halo effect) zone of lower conductivity caused by the kinematic viscosity maximum. The halo effect, evident on Figure 3.6 and Figure 4.5, is primarily caused by the maximum in kinematic viscosity due to the differences in density and surface tension between ethanol and water.

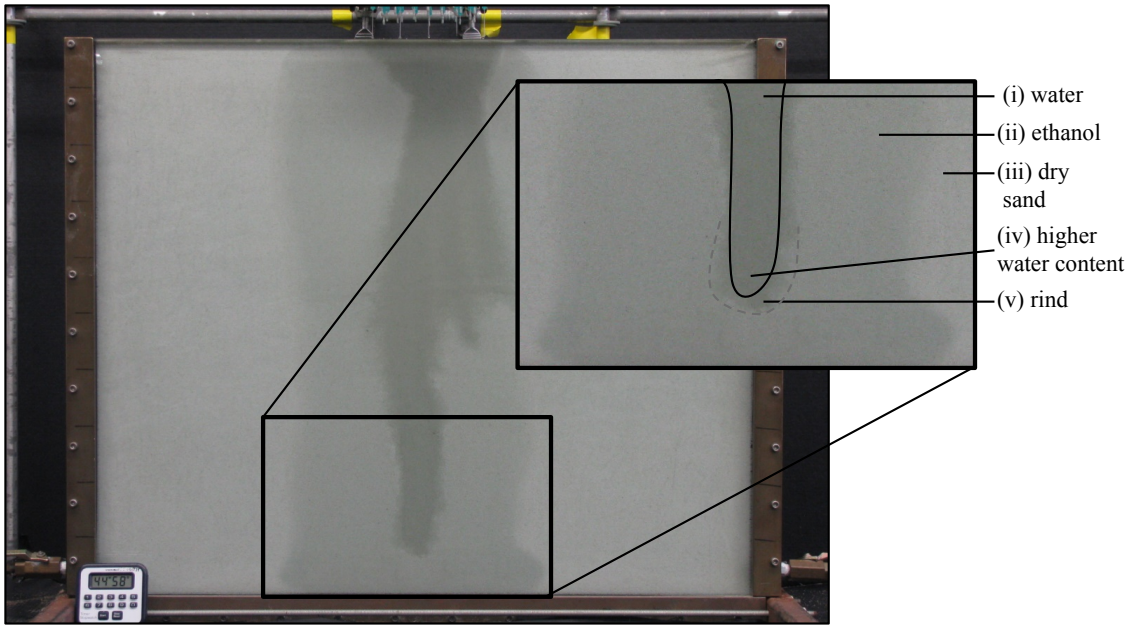


*Figure 5.2.* Zoomed schematic of experiment CF-J at 24:44:58 detailing (i) water, (ii) redistributed 95% ethanol, (iii) uncontaminated, dry sand, (iv) zone of higher water content, and (v) the rind zone.

## 5.3 Constant Head vs. Constant Flux

The constant flux (Section 3) and constant head (Section 4) experiments both strongly supported the hypotheses of this research with minor differences. The most significant difference was the initiation of multiple minor perturbations that occurred in water into ethanol constant flux experiments. The initiation of multiple perturbations did not occur in the water following ethanol constant head experiments. In the constant flux experiments, once one perturbation became dominant, the minor perturbations retreated.

Regarding application method, the nature of the constant head application is more controlled, whereas the constant flux application provides a less controlled and more variable application.

The lower volume and higher flux pulse constant flux experiments and higher tension constant head were experimentally designed at comparable fluid application and application rates. These experiments presented similar infiltration patterns and focused flow results, further supporting the findings of this work.

# 6 Summary and Conclusions

The unique infiltration behaviour of SCIFF was first reported by Smith et al. (2011) in butanol-contaminated sand. Infiltration of a fluid into a narrow, vertically focused flow into a previously contaminated porous media is a characterization of SCIFF. The research presented within this thesis provides greater understanding and insight into SCIFF behaviours for the case of water infiltrating into ethanol-contaminated unsaturated sand.

This research extended the investigation of focused flow behaviours through the inclusion of constant flux (Section 3) and constant head (Section 4) application of water into ethanol-contaminated sand. First and foremost, the primary hypothesis of this work was confirmed in that water infiltration into previously ethanol-contaminated unsaturated sand expressed vertical, highly focused flow (SCIFF) by methods of both constant flux and constant head. The primary driver behind the SCIFF behaviour in ethanol-contaminated sand was due to the differences of interfacial tensions between the two fluids. The secondary hypothesis was also confirmed; the application of ethanol into water-wetted unsaturated sand would produce a stable, semicircular infiltration pattern by methods of both constant head and constant flux.

A zone of lower saturation, or the halo effect, was strongly expressed in SCIFF for the ethanol-contaminated system. This zone of lower saturation was previously reported in literature for butanol (Smith et al., 2011). The more evident halo effect is likely due to the maximum of viscosity at aqueous concentrations of ethanol of 40% to 50% (Table 1.2; Figure 1.2), which sharpens and stabilizes the solute front and thereby enhances the zone of lower saturation.

Infiltration experiments were conducted by method of both constant flux (higher volume and lower flux continuous experiments and lower volume and higher flux pulse experiments) and constant head (lower tension and higher tension experiments) to mimic various real world scenarios. With similar flux rate applications and fluid volumes applied, constant flux and constant pressure head methods garnered similar results. This further confirmed that the delay in onset of SCIFF using constant head application is due to the finite volume applied as opposed to the boundary condition. The tension infiltrometer had a finite capacity limitation that needs to be considered since small volume applications with a smaller semicircular bulb exhibited delays in the time to initiate SCIFF instability. The finite volume application experiments that did not express SCIFF during infiltration initiated SCIFF during the redistribution period. This delay in SCIFF onset requires further investigation. However, it is hypothesized that maximum vertical depth of infiltration is a primary factor in SCIFF initiation. That is, for shorter depths of infiltration, hysteresis may play a primary role in SCIFF propagation. Specifically, the pressure head at the trailing drainage front needs to be considered.

As the primary focused flow is distinguished (under constant flux conditions), it then grows and propagates at the expense of the other remaining, potentially initiated focused flows. To clarify, the other focused flows retreat and drain into the singular, primary SCIFF pathway.

Furthering the understanding of the relationship between heterogeneity and SCIFF was not the primary aim of this work. The focused flow behaviours of water infiltrating into ethanol-contaminated sand overcame the effects of minor heterogeneity. Furthermore, it is reasonable to expect that SCIFF is a common primary flow process in ethanol-contaminated vadose zone scenarios as SCIFF was observed in water infiltration into ethanol-contaminated media that had infiltration fronts of ~ 5 cm deep. Natural heterogeneity is expected to contribute to initiating focused flow by providing enhanced initiation of primary pathways. This thesis research has displayed and enhanced the understanding of SCIFF behaviour during water infiltration into ethanol-contaminated sand.

# 7 Implications and Future Work

## 7.1 Implications

The results of this research have implications for the depths, rates, and patterns of infiltration of rainfall (constant flux) or water ponding (constant head) into ethanol-contaminated vadose zones and resultant contaminant mass transfers to groundwaters. The information presented in this thesis could prove valuable when assessing depth, rate,

and patterns of vadose zone contamination of any alcohol or water-miscible contaminants with similar physical properties to ethanol.

Regarding remedial efforts, water application into ethanol-contaminated vadose zones will create preferential and persistent conduits through the contaminated vadose zone, bringing the contaminant deeper into the subsurface with potentially less lateral movement (Glass et al., 1989a; Glass et al., 1989b). Remedial efforts should be targeted deeper into the subsurface rather than laterally.

## 7.2 Future Work

It is recommended that future work in this area be expanded to more laboratory experimentation, experiments in a field setting, and comprehensive modelling of the findings. The results from the laboratory experiments presented in this thesis show great promise for future experimental work. Understanding the variables of a homogenous system is critical to understanding the variables of a heterogeneous system. Homogeneously packed sands are not common outside of laboratory settings but are significant in scientific research. Therefore, experiments in heterogeneously packed flow cells could provide better insight into focused flow behaviours for more complex settings (Bashir et al., 2007). This focused flow mechanism could be dominant in other alcohol- or surfactant-contaminated systems. Therefore, expanding the laboratory work to a range of ethanol concentrations and various alcohols could provide better understanding of the effects and differences between focused flow infiltration rates. As gasoline spills and

releases are becoming increasingly common (especially at distribution terminals and on common transport pathways such as roads and railways), understanding the effects of the focused flow behaviour as part of ethanol blended gasoline (as the contaminant of interest) could also prove extremely valuable (Cápiro et al., 2007; Freitas & Barker, 2013a; Lee, 2008; Powers et al., 2001; Sciortino & Leij, 2012; Stafford et al., 2009).

Data collection within the vadose zone can prove to be difficult. The use of time domain reflectometry to quantify water content and tensiometers to quantify pressure head could provide valuable increased understanding of the system (Henry & Smith, 2003). However, high-density placement (fine spatial grid) and small time steps would be recommended as the focused flow phenomenon is complex and low spatial resolution may not provide added benefit. Moisture content visualization techniques, similar to those used by Glass et al. (1989b), could also provide valuable insights. To enhance the accuracy of conceptual and numerical models within this scope of work, accurate concentration-dependent surface tension values through laboratory experimentation are required (Smith & Gilham, 1999).

Ideally, pilot-scale field experiments for this scope of work should be carried out to assess the differences of focused flow infiltration patterns between field and laboratory settings. Laboratory experiments provide insight into individual processes, whereas field-scale experiments provide insights into the interaction between simultaneous processes. This expanded scope of work could provide real world context for these focused flow

infiltration behaviours. Drawing comparisons between laboratory and pilot-scale experiments, similarly to Cápiro et al. (2007) and Stafford et al. (2009), could provide valuable insights.

Numerically modelling current laboratory work and future field experiments could provide additional insights into understanding the details of the focused flow infiltration behaviours. Numerical modelling of this nature is uncommon due to the lack of experimental data to support the model and the challenge of modelling the system (Henry & Smith, 2003). Furthermore, to accurately model this work, hysteretic functions should be included. The HYDRUS 2-D model accounts for hysteretic moisture retention and could support the numerical modelling of this work. The results of this laboratory study provide valuable data for further investigation using the solute concentration-dependent coupled hysteretic unsaturated flow and transport 2-D model developed by Bashir et al. (2009). Comparison between laboratory experiments, field experiments, and modelling could provide important insights into the comprehensive understanding of this work.

# 8 References

Alvarenga, R.A.F., & Dewulf, J. (2013). Plastic vs. fuel: Which use of the Brazilian ethanol can bring more environmental gains? *Renewable Energy, 59,* 49-52. doi: 10.1016/j.renene.2013.03.029

Bashir, R., Smith, J.E., Henry, E.J., & Stolle, D. (2009). On the importance of hysteresis in numerical modeling of surfactant-induced unsaturated flow. *Soil & Sediment Contamination, 18(3),* 264-283. doi: 10.1080/15320380902772638

Bashir, R., Smith, J.E., & Stolle, D.E. (2008). Surfactant-induced unsaturated flow: instrumented horizontal flow experiment and hysteretic modeling. *Soil Science Society of America Journal, 72(6),* 1510-1519. doi: 10.2136/sssaj2007.0259

Bashir, R., Smith, J.E., & Stolle, D.E. (2011). The effect of ionic strength on surfactant-induced unsaturated flow. *Canadian Geotechnical Journal, 48(4),* 644-654. doi: 10.1139/t10-096

Bashir, R., Stolle, D.F., & Smith, J.E. (2007). Flux-based alternative formulation for variably saturated subsurface flow. *Journal of Hydrologic Engineering, 12(5),* 501-512. doi: 10.1061/(ASCE)1084-0699(2007)12:5(501)

Beatty, S.M., & Smith, J.E. (2013). Dynamic soil water repellency and infiltration in post-wildfire soils. *Geoderma, 192(1),* 160-172. doi: 10.1016/j.geoderma.2012.08.012

Beatty, S.M., & Smith, J.E. (2014). Infiltration of water and ethanol solutions in water repellent post wildfire soils. *Journal of Hydrology, 514,* 233-248. doi: 10.1016/j.jhydrol.2014.04.024

Brady, N.C., & Weil, R.R. (1999). *The nature and properties of soils (12th Ed.)*. Toronto, Canada: Prentice-Hall Canada Inc.

Cápiro, N.L., Stafford, B.P., Rixey, W.G., Bedient, P.B., & Alvarez, P.J.J. (2007). Fuel-grade ethanol transport and impacts to groundwater in a pilot-scale aquifer tank. *Water Research, 41(3),* 656-664. doi: 10.1016/j.watres.2006.09.024

Chuoke, R.L., van Meurs, P., & van der Poel, C. (1959). The instability of slow, immiscible, viscous liquid-liquid displacements in permeable media. *Petroleum Transactions, 219,* 188-194.

Fetter, C.W. (1999). *Contaminant hydrogeology (2nd Ed.)*. Long Grove, IL: Waveland Press Inc.

Freeze, R.A, & Cherry, J.A. (1979). *Groundwater*. Eaglewood Cliffs, NJ: Prentice Hall.

Freitas, J.G., & Barker, J.F. (2011). Monitoring lateral transport of ethanol and dissolved gasoline compounds in the capillary fringe. *Ground Water Monitoring & Remediation, 31(3),* 95-102. doi: 10.1111/j.1745-6592.2011.01338.x

Freitas, J.G., & Barker, J.F. (2013a). Denatured ethanol release into gasoline residuals, Part 1: Source behaviour. *Journal of Contaminant Hydrology, 148,* 67-78. doi: 10.1016/j.jconhyd.2012.12.010

Freitas, J.G., & Barker, J.F. (2013b). Denatured ethanol release into gasoline residuals, Part 2: Fate and transport. *Journal of Contaminant Hydrology, 148,* 79-91. doi: 10.1016/j.jconhyd.2012.12.009

Glass, R.J., & Steenhuis, T.S. (1984). *Factors influencing infiltration flow stability and movement of toxics in layered sandy soils*. St. Joseph, MI: ASAE Technical Paper, 1-31.

Glass, R.J., Parlange, J.Y., & Steenhuis, T.S. (1989a). Wetting front instability: 1. Theoretical discussion and dimensional analysis. *Water Resources Research, 25(6),* 1187-1194. doi: 10.1029/WR025i006p01187

Glass, R.J., Steenhuis, T.S., & Parlange, J.Y. (1989b). Mechanism for finger persistence in homogenous, unsaturated, porous media: theory and verification. *Soil Science, 148(1),* 60-70. doi: 10.1097/00010694-198907000-00007

Glass, R.J., Steenhuis, T.S., & Parlange, J.Y. (1989c). Wetting front instability: 2. Experimental determination of relationships between system parameters and two-dimensional unstable flow field behaviour in initially dry porous media. *Water Resources Research, 25(6),* 1195-1207. doi: 10.1029/WR025i006p01195

Henry, E.J., & Smith, J.E. (2002). The effect of surface-active solutes on water flow and contaminant transport in variably saturated porous media with capillary fringe effects. *Journal of Contaminant Hydrology, 56(3-4),* 247-270. doi:10.1016/S0169-7722(01)00206-6

Henry, E.J., & Smith, J.E. (2003). Surfactant-induced flow phenomena in the vadose zone: A review of data and numerical modeling. *Vadose Zone Journal, 2(2),* 154-167. doi: 10.2113/2.2.154

Henry, E.J., Smith, J.E., & Warrick, A.W. (2002). Two-dimensional modeling of flow and transport in the vadose zone with surfactant-induced flow. *Water Resources Research, 38(11),* 33/1–33/16. doi: 10.1029/2001WR000674

Hillel, D. (1998). *Environmental soil physics*. San Diego, California: Academic Press.

Kadlec, P., Henke, S., & Bubnik, Z. (2010). Properties of ethanol and ethanol-water solutions - Tables and Equations. *Sugar Industry/ Zuckerindustrie, 135(10),* 607-613.

Koorevaar, P., Menelik, G., & Dirksen, C. (1983). *Elements of soil physics, Volume 13*. Amsterdam, Netherlands: Elsevier Science.

Lee, K.Y. (2008). Viscosity of high-alcohol content fuel blends with water: Subsurface contaminant transport implications. *Journal of Hazardous Materials, 160(1),* 94-99. doi: 10.1016/j.jhazmat.2008.02.088

Lide, D.R. (1993). *Handbook of chemistry & physics (74th Ed.)*. CRC Press.

McLeod, H.C. (2015). *Investigating gas phase processes in natural and hydrocarbon-contaminated groundwater (Unpublished doctoral dissertation)*. McMaster University, Hamilton, ON.

Miller, E.E., & Miller, R.D. (1956). Physical theory for capillary flow phenomena. *Journal of Applied Physics, 27(4),* 324-332. doi: 10.1063/1.1722370

Mualem, Y. (1976). A new model for predicting the hydraulic conductivity of unsaturated porous media. *Water Resources Research, 12(3),* 513-522. doi: 10.1029/WR012i003p00513

Opta Minerals Inc. (2018). *Technical data sheet*. Waterdown, ON: Opta Minerals Inc.

Parlange, J.Y., & Hill, D.E. (1976). Theoretical analysis of wetting front instability in soils. *Soil Science, 122 (4),* 236-239. doi: 10.1097/00010694-197610000-00008

Powers, S.E., Rice, D., Dooher, B., & Alvarez, P.J.J. (2001). Will ethanol-blended gasoline affect groundwater quality? *Environmental Science & Technology, 35(1),* 24A-30A. doi: 10.1021/es012247h

Reynolds, W.D., & Zebchuk, W.D. (1996). Use of contact material in tension infiltrometer measurements. *Soil Technology, 9(3),* 141-159. doi: 10.1016/S0933-3630(96)00009-8

Ricci Bros Sand Co., Inc. (2018). *Industrial sand cross reference typical analysis and properties.* Port Norris, NJ: Ricci Bros Sand Co, Inc.

Sciortino, A., & Leij, F.J. (2012). Numerical investigation of the impact of ethanol on flow in the vadose zone. *Groundwater, 50(6),* 883-894. doi: 10.1111/j.1745-6584.2011.00908.x

Silliman, S.E., Berkowitz, B., Simunek, J., & Van Genuchten, M.Th. (2002). Fluid flow and solute migration within the capillary fringe. *Ground Water, 40(1),* 76-84. doi: 10.1111/j.1745-6584.2002.tb02493.x

Smith, J.E., Henry, E.J., & Bashir, R. (2011). Solute-dependent capillarity-induced focused flow during infiltration into alcohol-contaminated soil. *Vadose Zone Journal, 10(1),* 403-411. doi: 10.2136/vzj2009.0081

Smith, J.E., & Gilham, R. W. (1999). Effects of solute concentration-dependent surface tension on unsaturated flow: Laboratory sand column experiments. *Water Resources Research, 35 (4),* 973-982. doi: 10.1029/1998WR900106

Smith, J.E., & Zhang, Z.F. (2001). Determining effective interfacial tension and predicting finger spacing for DNAPL penetration into water-saturated porous media. *Journal of Contaminant Hydrology, 48(1-2),* 167-183. doi: 10.1016/S0169-7722(00)00166-2

Spencer, S.J., Andrews, G.T., & Deacon, C.G. (2013). Contact angle of ethanol-water solutions on crystalline and mesoporous silicon. *Semiconductor Science and Technology, 28(5),* 1-5. doi: 10.1088/0268-1242/28/5/055011

Stafford, B.P., Cápiro, N.L., Alvarez, P.J.J., & Rixey, W.G. (2009). Pore water characteristics following a release of neat ethanol onto pre-existing NAPL. *Ground Water Monitoring & Remediation, 29 (3),* 93-104. doi: 10.1111/j.1745-6592.2009.01243.x

Stafford, B.P., & Rixey, W.G. (2011). Distribution of fuel-grade ethanol near a dynamic water table. *Ground Water Monitoring & Remediation, 31(3),* 55-60. doi: 10.1111/j.1745-6592.2011.01348.x

van Genuchten, M. Th. (1980). A closed-form equation for predicting the hydraulic conductivity for unsaturated soils. *Soil Science Society of America Journal, 44(5),* 892-898. doi: 10.2136/sssaj1980.03615995004400050002x

Zhang, Z.F., & Smith, J.E. (2001). The velocity of DNAPL fingering in water-saturated porous media: laboratory experiments and a mobile-immobile-zone model. *Journal of Contaminant Hydrology, 49(3-4),* 335-353. doi: 10.1016/S0169-7722(01)00097-3

Zhang, Z. F., & Smith, J.E. (2002). Visualization of DNAPL fingering processes and mechanisms in water-saturated porous media. *Transport in Porous Media, 48(1),* 41-59. doi: 10.1023/A:1015675404195

# 9 Appendix

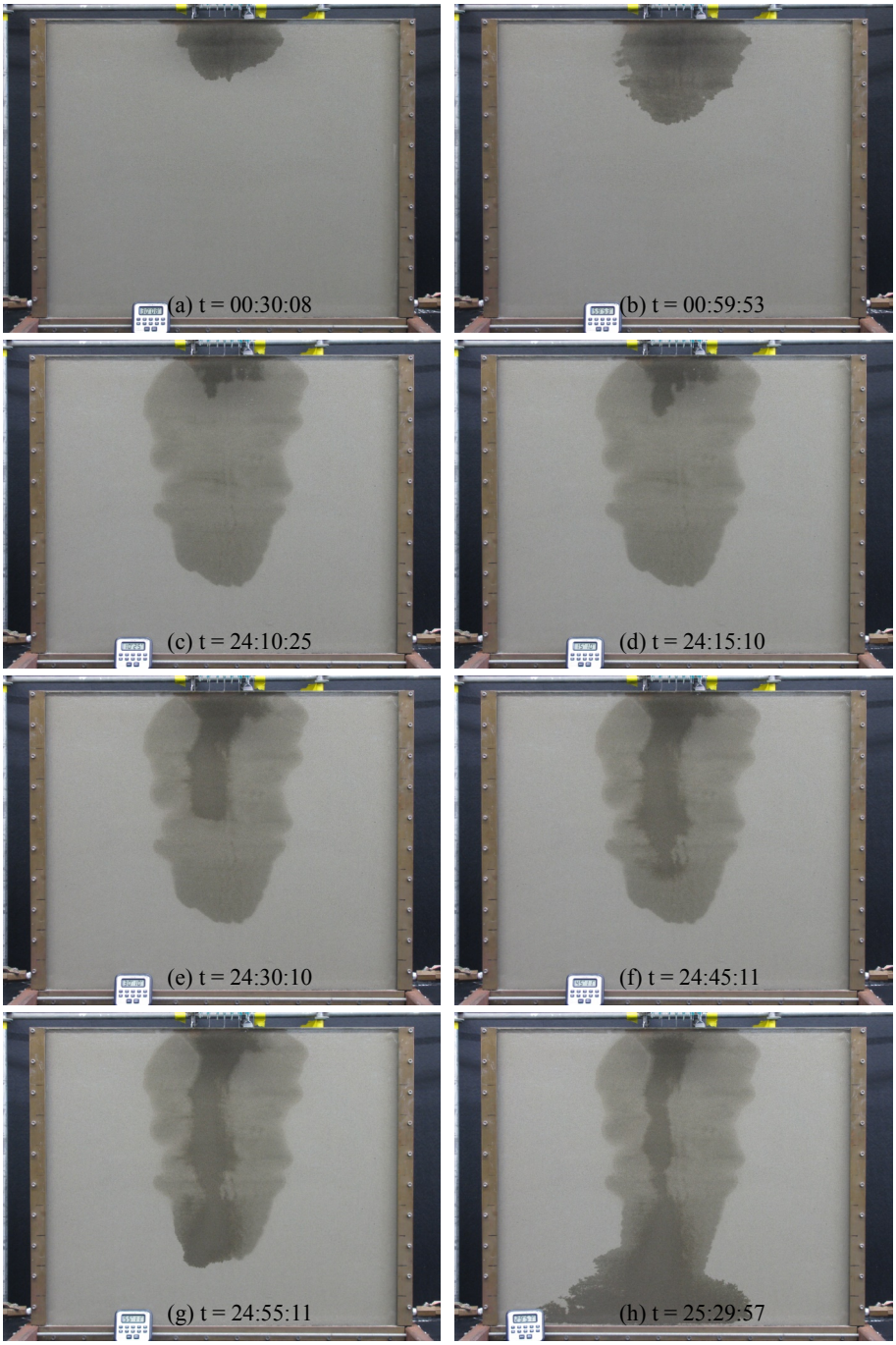


*Figure A.1.* Higher volume and lower flux continuous water following ethanol infiltration constant flux experiment CF-B. Sequenced photographs of experiment CF-B with time zero being the beginning of ethanol application (a) t = 00:30:08, (b) t = 00:59:53, (c) t = 24:10:25 (start of water application), (d) t = 24:15:10, (e) t = 24:30:10, (f) t = 24:45:11, (g) t = 24:55:11, and (h) t = 25:29:57.

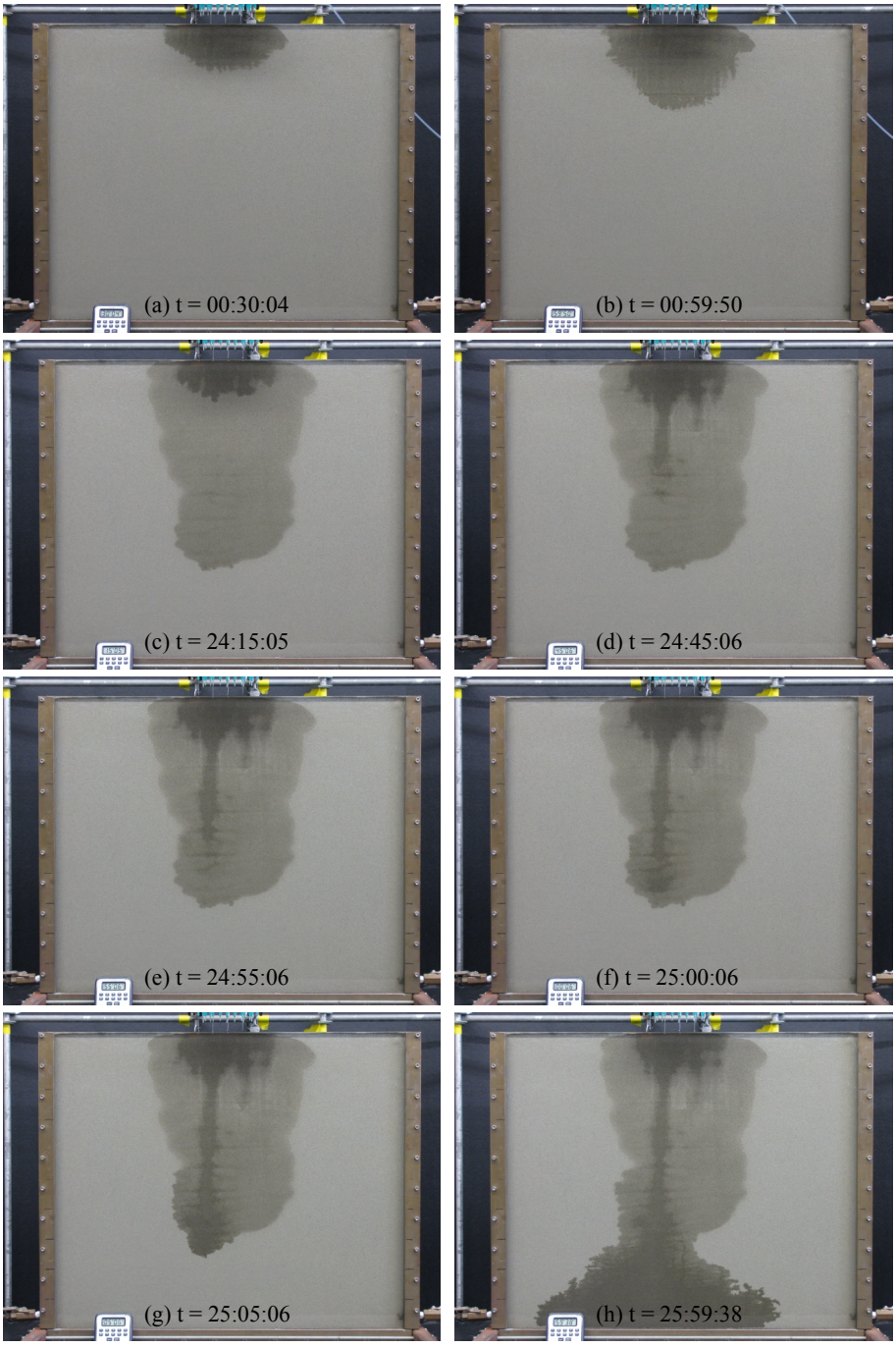


*Figure A.2.* Higher volume and lower flux continuous water following ethanol infiltration constant flux experiment CF-D. Sequenced photographs of experiment CF-D with time zero being the beginning of ethanol application (a) t = 00:30:04, (b) t = 00:59:50, (c) t = 24:15:05 (start of water application), (d) t = 24:45:06, (e) t = 24:55:06, (f) t = 25:00:06, (g) t = 25:05:06, and (h) t = 26:59:38.

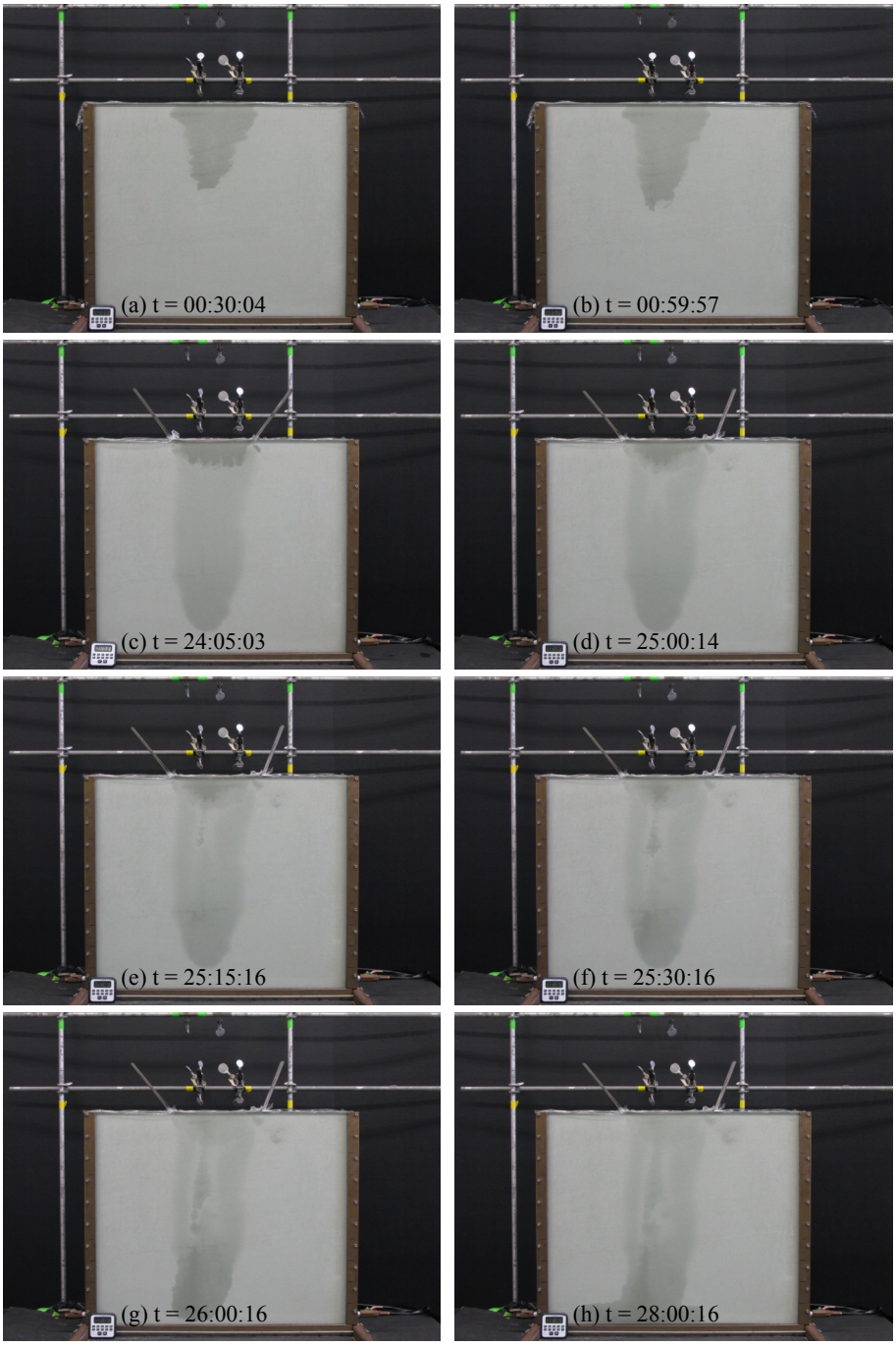


*Figure A.3.* Lower volume and higher flux pulse water following ethanol infiltration constant flux experiment CF-K. Sequenced photographs of experiment CF-K with time zero being the beginning of ethanol application (a) t = 00:30:04, (b) t = 00:59:57, (c) t = 24:05:03 (start of water application), (d) t = 25:00:14, (e) t = 25:15:16, (f) t = 25:30:16, (g) t = 26:00:16, and (h) t = 28:00:16.

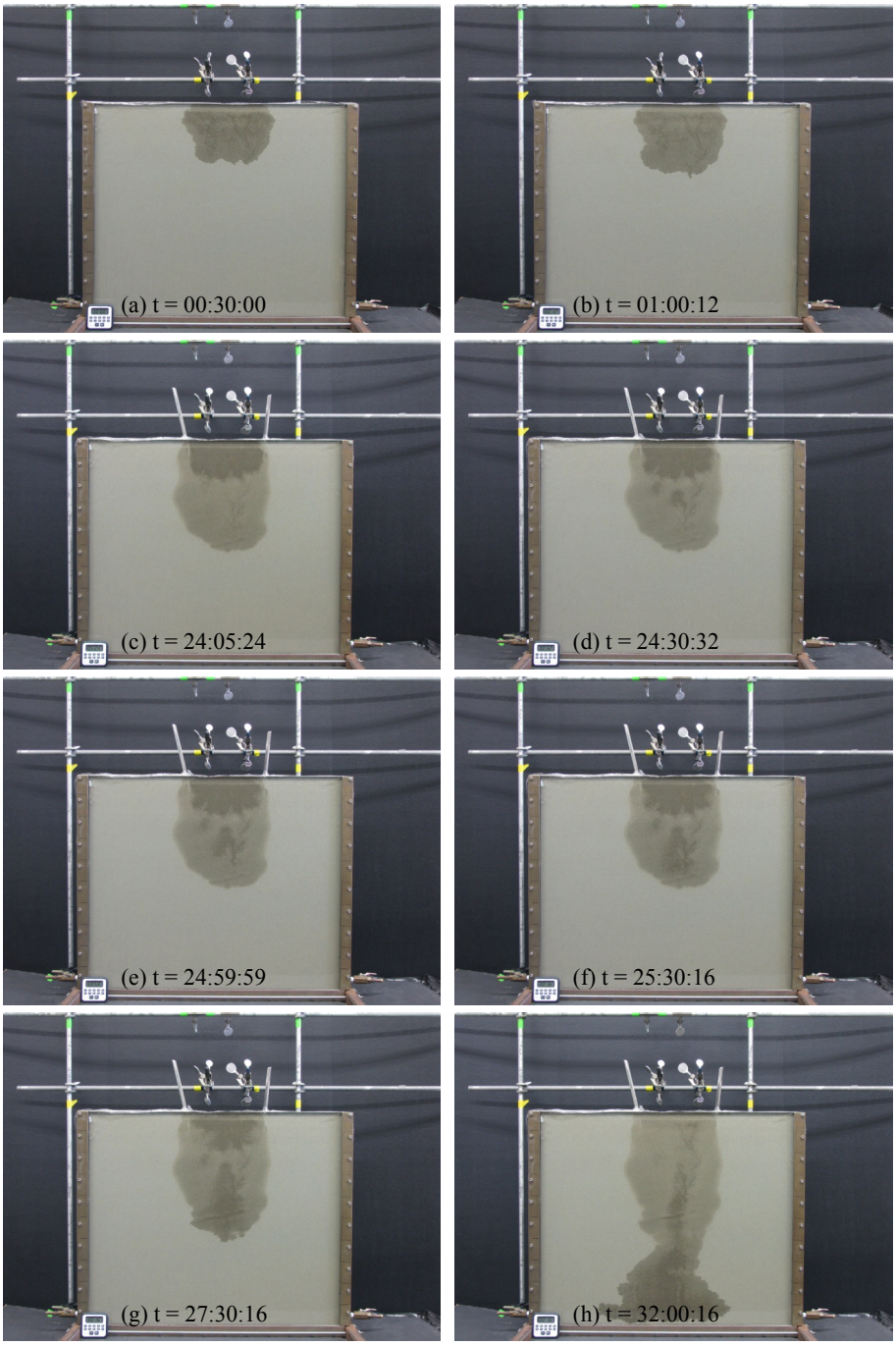


*Figure A.4.* Lower volume and higher flux pulse water following ethanol infiltration constant flux experiment CF-N. Sequenced photographs of experiment CF-N with time zero being the beginning of ethanol application (a) t = 00:30:00, (b) t = 01:00:12, (c) t = 24:05:24 (start of water application), (d) t = 24:30:32, (e) t = 24:59:59, (f) t = 25:30:16, (g) t = 27:30:16, and (h) t = 32:00:16.

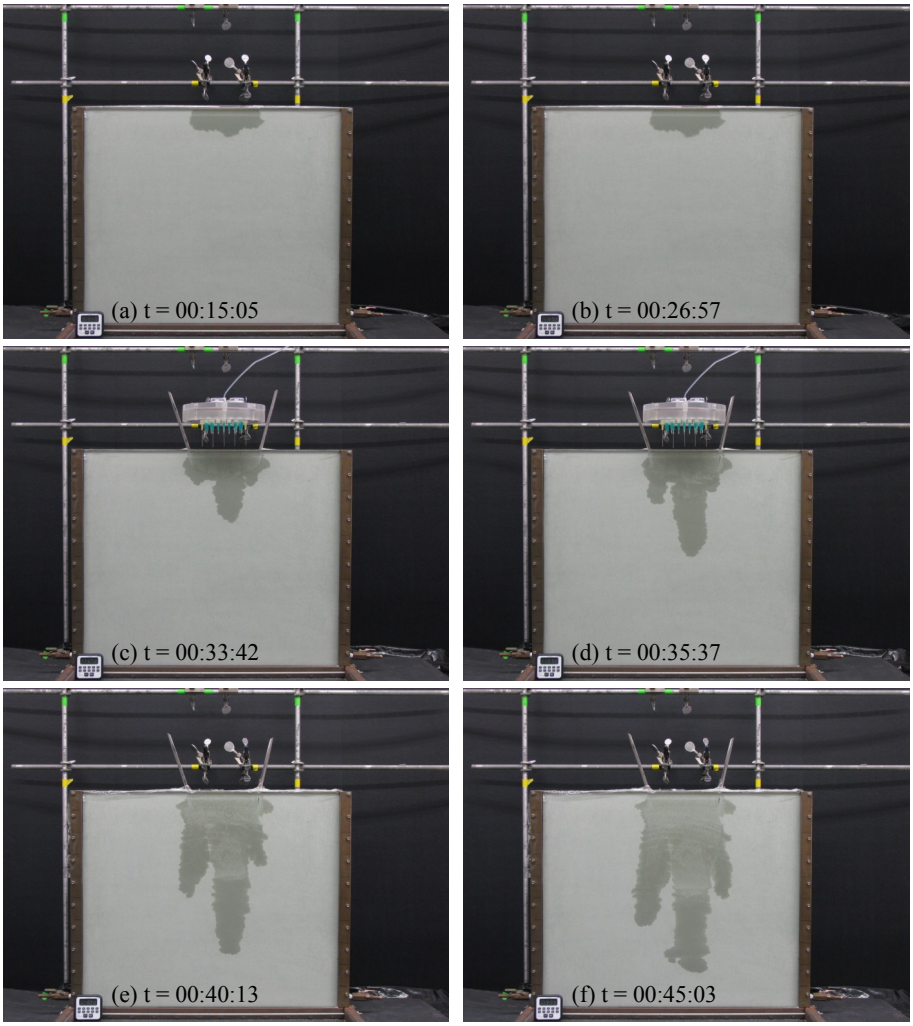


*Figure A.5.* Ethanol following water infiltration constant flux experiment CF-Q. Sequenced photographs of experiment CF-Q with time zero being the beginning of water application at (a) t = 00:15:05, (b) t = 00:26:57, (c) t = 00:33:42 (start of ethanol infiltration), (d) t = 00:35:37, (e) t = 00:40:13, and (f) t = 00:45:03.

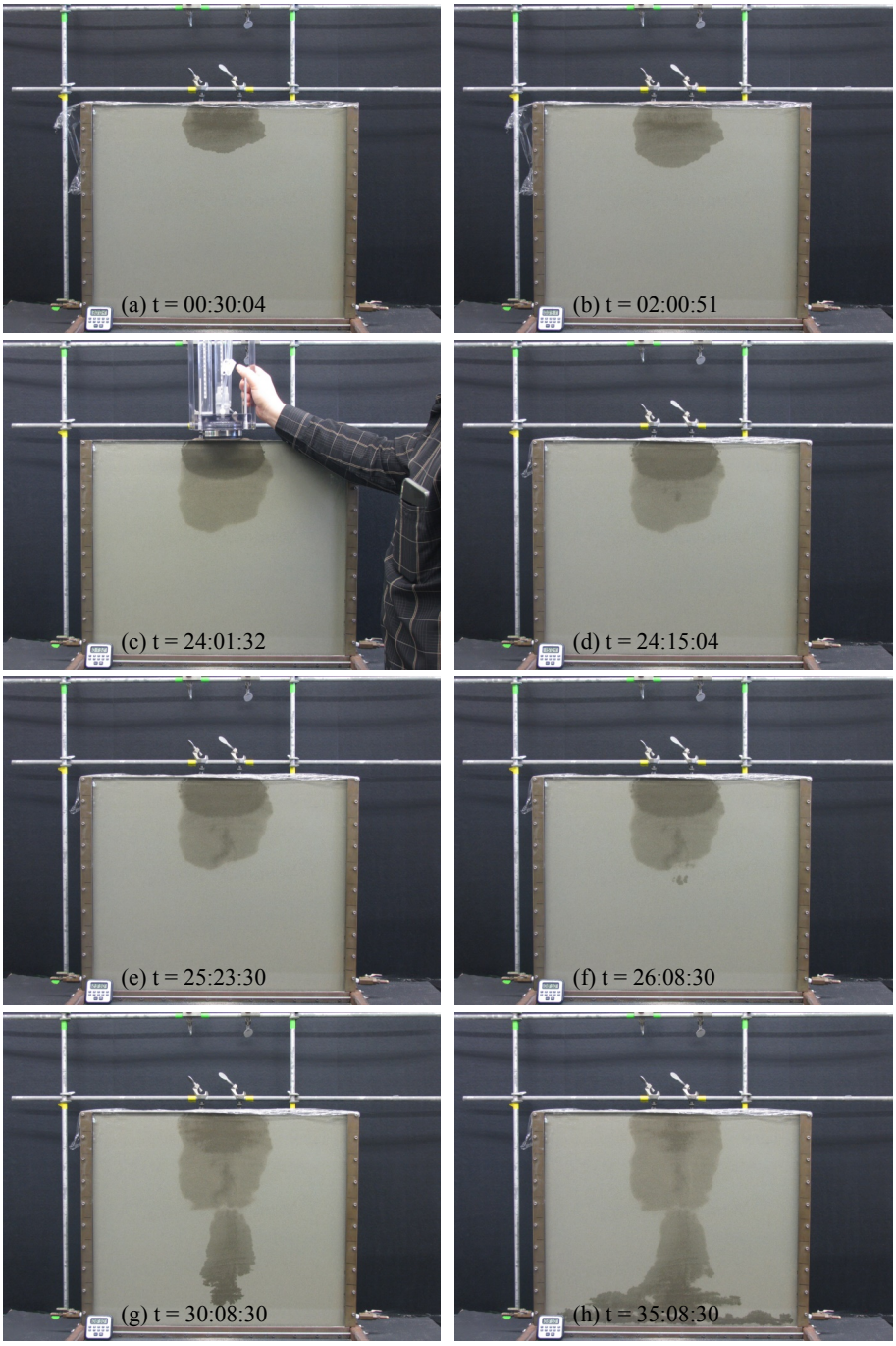


*Figure A.6.* Lower tension water following ethanol infiltration constant head experiment CH-4. Sequenced photographs of experiment CH-4 with time zero being the beginning of ethanol application (a) t = 00:30:04, (b) t = 02:00:51, (c) t = 24:01:32 (start of water application), (d) t = 24:15:04, (e) t = 25:23:30, (f) t = 26:08:30, (g) t = 30:08:30, and (h) t = 35:08:30.

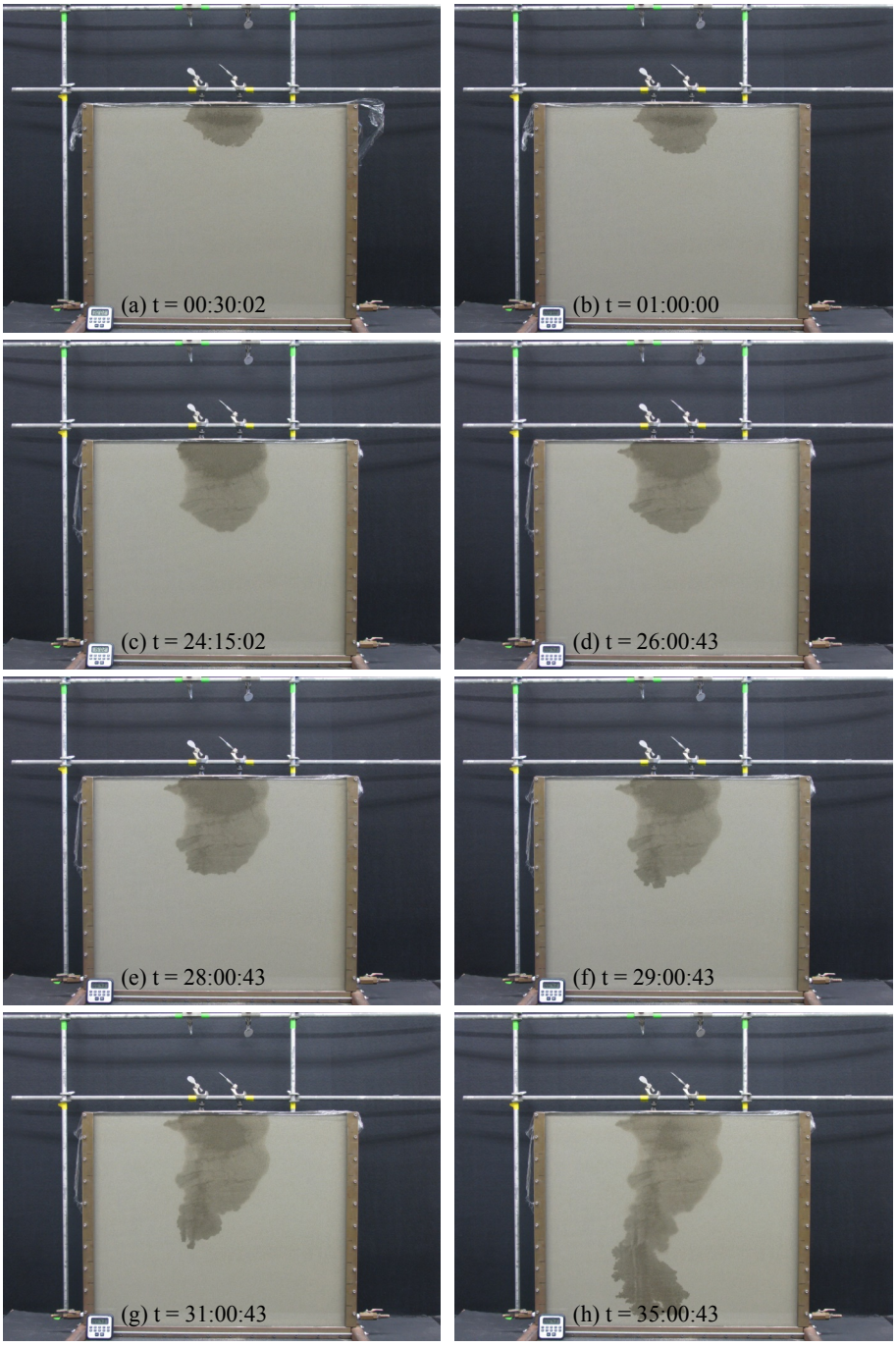


*Figure A.7.* Lower tension water following ethanol infiltration constant head experiment CH-5. Sequenced photographs of experiment CH-5 with time zero being the beginning of ethanol application (a) t = 00:30:02, (b) t = 01:00:00, (c) t = 24:15:02 (start of water application), (d) t = 26:00:43, (e) t = 28:00:43, (f) t = 29:00:43, (g) t = 31:00:43, and (h) t = 35:00:43.

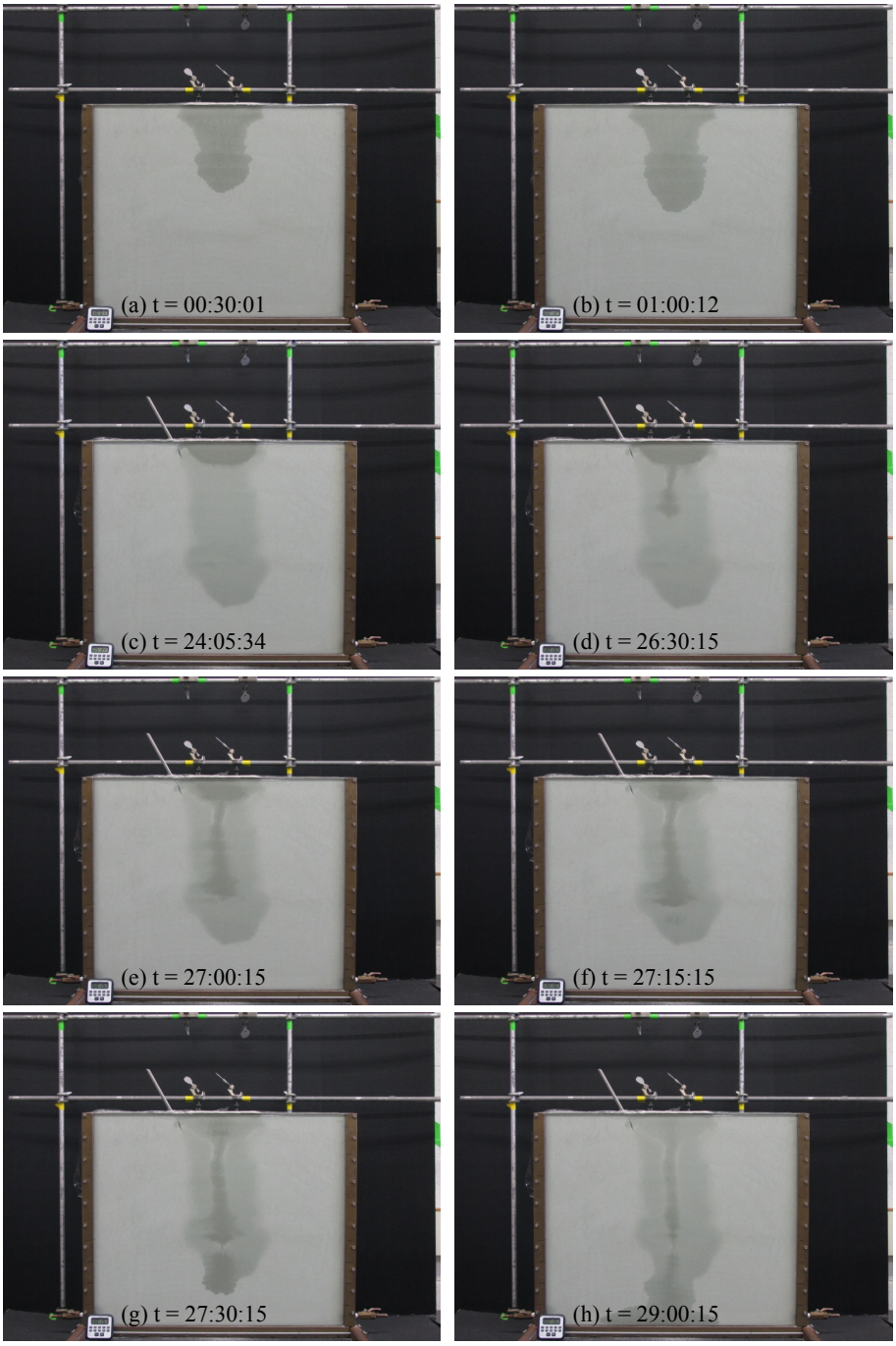


*Figure A.8.* Lower tension water following ethanol infiltration constant head experiment CH-7. Sequenced photographs of experiment CH-7 with time zero being the beginning of ethanol application (a) t = 00:30:01, (b) t = 01:00:12, (c) t = 24:05:34 (start of water application), (d) t = 26:30:15, (e) t = 27:00:15, (f) t = 27:15:15, (g) t = 27:30:15, and (h) t = 29:00:15.

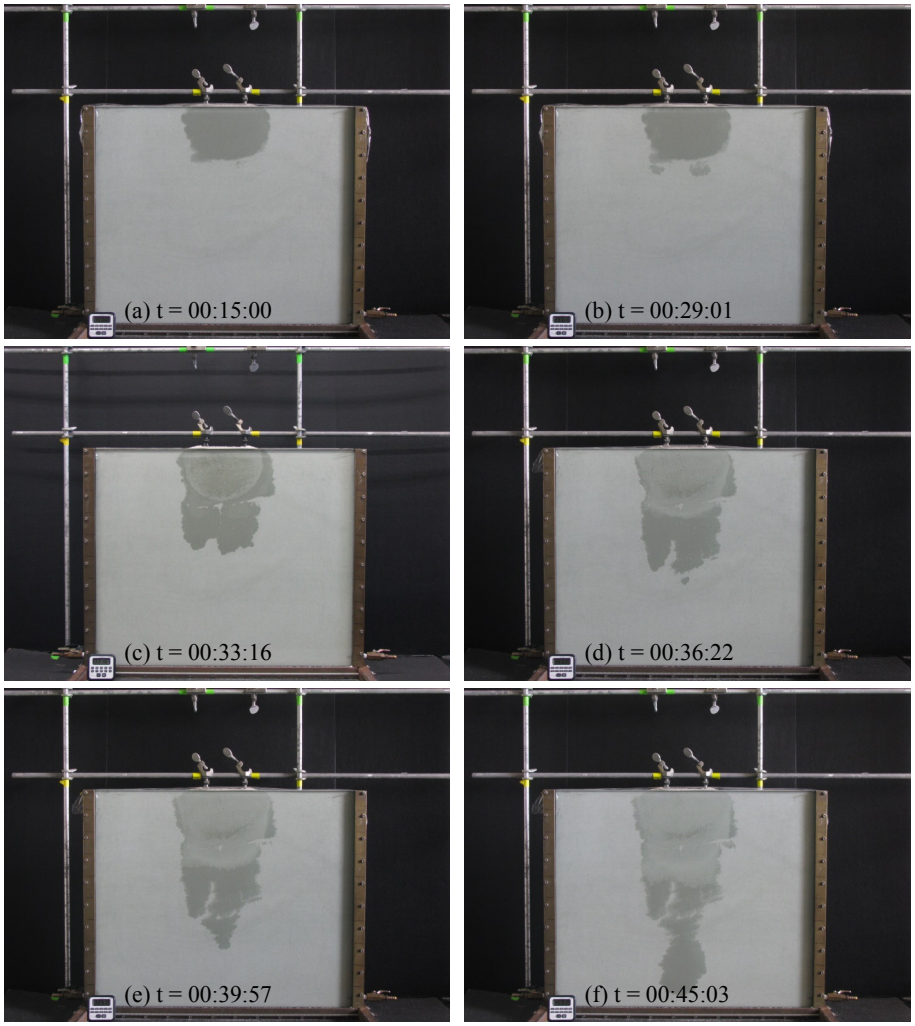


*Figure A.9.* Ethanol following water infiltration constant head experiment CH-11. Sequenced photographs of experiment CH-11 with time zero being the beginning of water application (a) t = 00:15:00, (b) t = 00:29:01, (c) t = 00:33:16 (start of ethanol application), (d) t = 00:36:22, (e) t = 00:39:57, and (f) t = 00:45:03.

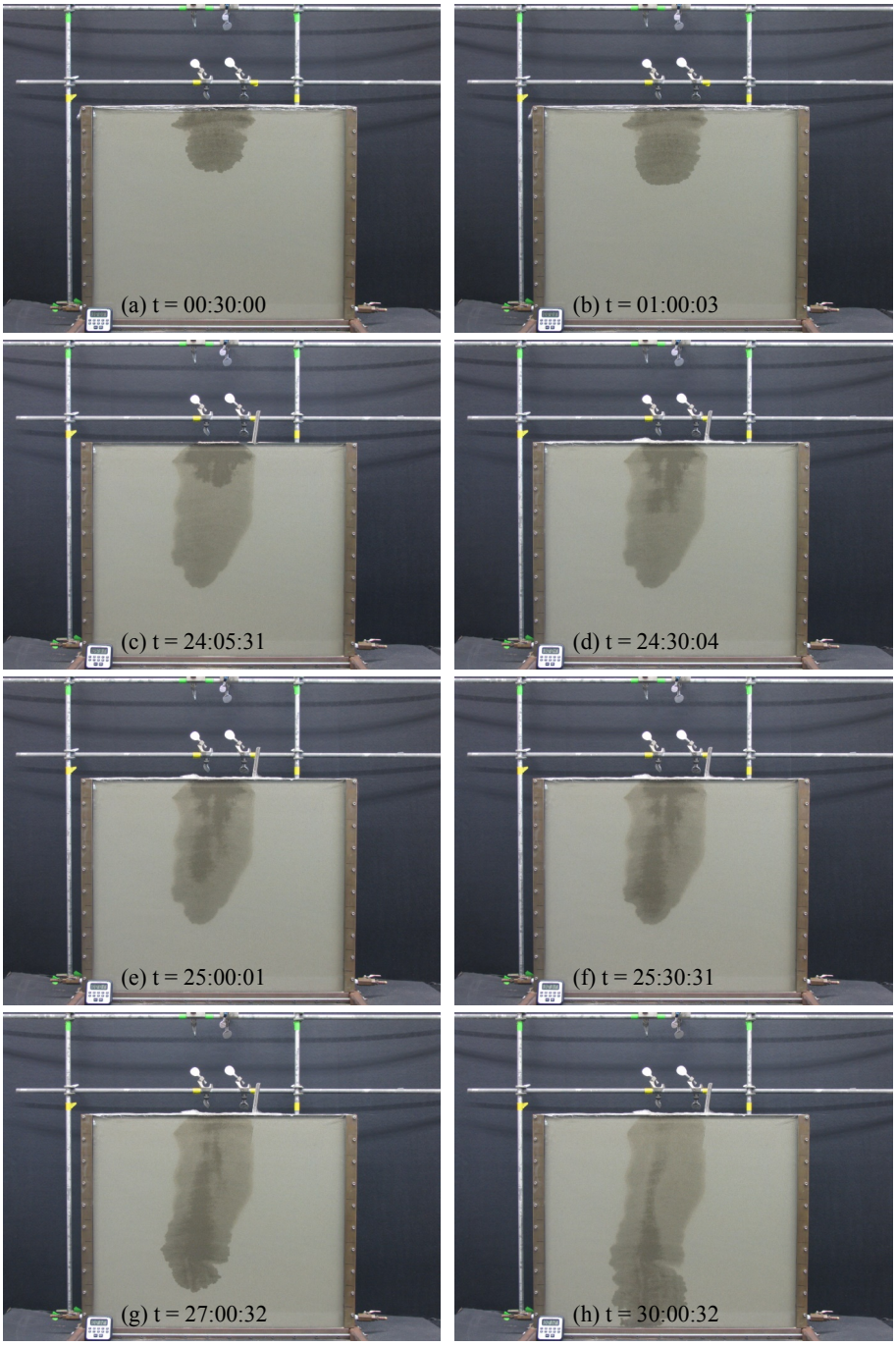


*Figure A.10.* Higher tension water following ethanol infiltration constant head experiment CH-15. Sequenced photographs of experiment CH-15 with time zero being the beginning of ethanol application (a) t = 00:30:00, (b) t = 01:00:03, (c) t = 24:05:31 (start of water application), (d) t = 24:30:04, (e) t = 25:00:01, (f) t = 25:30:31, (g) t = 27:00:32, and (h) t = 30:00:32.

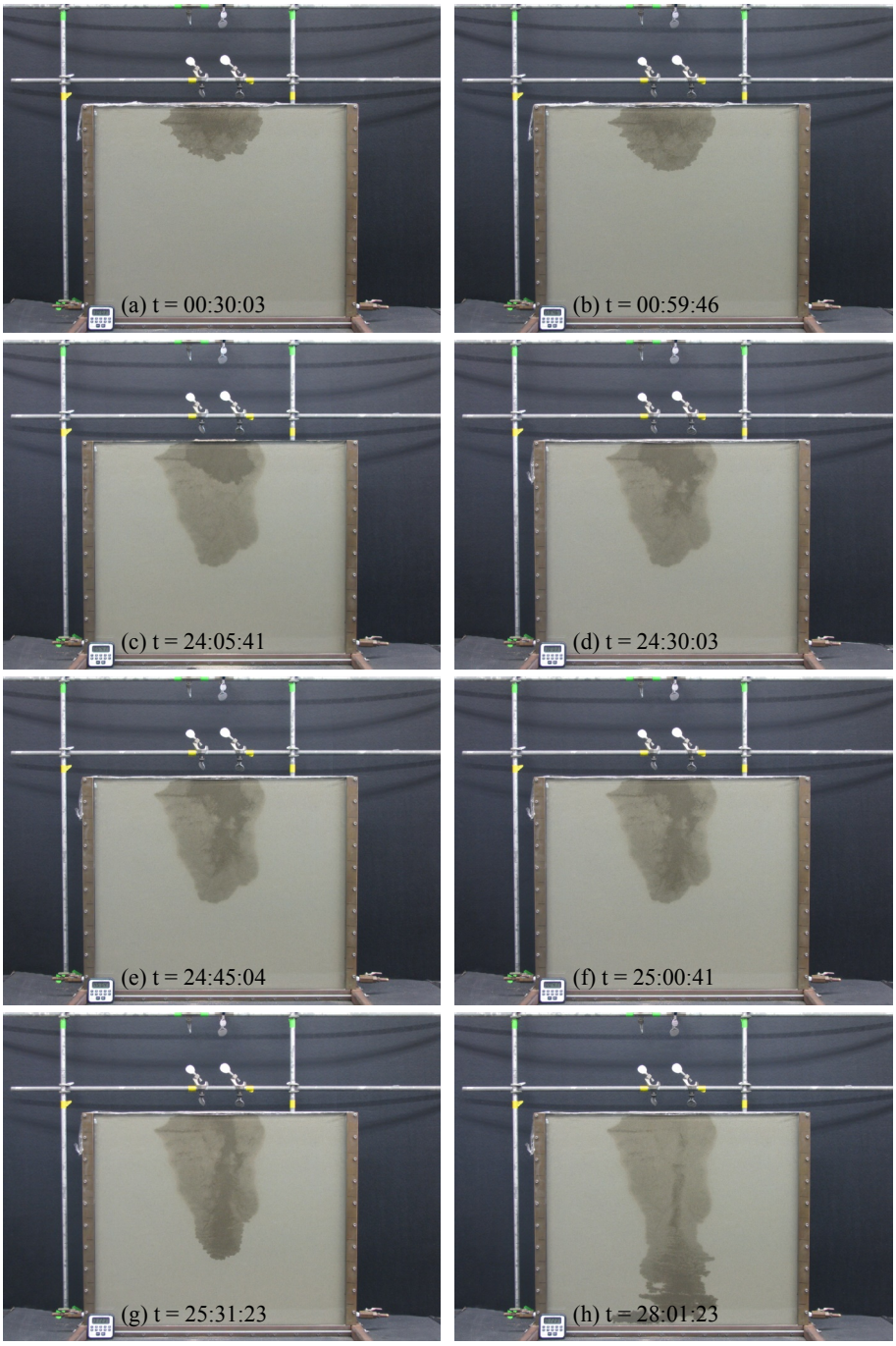


*Figure A.11.* Higher tension water following ethanol infiltration constant head experiment CH-16. Sequenced photographs of experiment CH-16 with time zero being the beginning of ethanol application (a) t = 00:30:03, (b) t = 00:59:46, (c) t = 24:05:41 (start of water application), (d) t = 24:30:03, (e) t = 24:45:04, (f) t = 25:00:41, (g) t = 25:31:23, and (h) t = 28:01:23.